EXCITATION PROCESSES OF RARE GAS ATOMS BY ELECTRON IMPACT

by

SALIM H. AL-SHAMMA
M.Phil. (University of Southampton)

Thesis submitted to the University of Stirling
for the degree of Doctor of Philosophy

Institute of Atomic Physics
University of Stirling

September, 1978.

A B S T R A C T

A study has been made of excitation functions of rare gas atoms (He, Ne, Ar, Kr, and Xe) near threshold by observing the UV photons emitted from the first excited states following electron impact, and a comparison is made with previous experiments.

The angular intensity distributions of photons emitted from the first excited states of Kr and Xe were also obtained and polarization values were deduced from these measurements.

The electron energy loss spectra of He, Ar, Kr, and Xe were measured in the incident electron energy range of 25 to 45 eV and at scattering angles of 27^{o} and 40^{o}.

From these measurements, the inelastic cross sections of the prominent peaks of Ar, Kr, and Xe were obtained, and in addition, the differential excitation functions of Ar, Kr and Xe were studied.

A delayed coincidence technique was applied to investigate the angular correlation between electrons scattered inelastically from Kr and photons emitted in the decay of $^{3}P_{1}$ and $^{1}P_{1}$ states to the ground state.

A C K N O W L E D G E M E N T S

I wish to express my gratitute to Professor H. Kleinpoppen and to Dr. J.F. Williams, my supervisors, for their valued guidance and encouragement during the course of this work.

I am greatly indebted to Drs. I. McGregor and D. Hils for frequent discussions and their assistance in overcoming the difficulties associated with this experiment. The help of Dr. M.C. Standage in the early stages of the experiment is also acknowledged.

I also wish to thank Drs. A.J. Duncan and R. Hippler for their useful comments.

I would like to extend my gratitude to our technicians, Mr. A.J. Duncan and Mr. A. Sherman for their technical assistance, and to Mrs. A. Dunlop for typing the thesis.

I acknowledge financial support from the University of Mosul (Iraq).

C O N T E N T S

CHAPTER 1

INTRODUCTION

The study of the electron impact excitation of atoms is of great interest for the understanding of impact excitation of atoms in general.

Within the last two decades, great progress has been made in overcoming previous difficulties related to the electron sources themselves and their applications in particular experiments. Electron impact excitation studies with improved electrostatic spectrometers have been reviewed by Lassettre (1969). There is, however, only a limited amount of experimental information available on energy loss spectra of rare gas atoms and their inelastic cross sections. Theoretically, Sawada et al (1971) have predicted the energy dependence of differential inelastic cross sections of 3p - 4s, s' for Ar at 30^{o} scattering angle by using a distorted wave theory.

At Stirling, a crossed beam apparatus was constructed by previous workers (Raible (1974), and Koschmieder (1974)) to study low energy electron scattering from atomic hydrogen and the excitation functions of the first excited states of rare gas atoms by observing the UV photons emitted during the decay.

This thesis represents a continuation and expansion of the work of Raible and Koschmieder and contains the following results:

1. Improvements to the previous measurements of the excitation functions for the first excited states of Ne, Ar, Kr, and Xe and presents a measurement of the excitation function of He (see chapter 3).

2. The first measurements of the angular intensity distributions, and hence the polarization of the UV photons emitted from the

$4p^5$ 5s $^3P_1$ and $^1P_1$, and $5p^5$ 6s $^3P_1$ and $^1P_1$ states of Kr and Xe respectively (see chapter 4).

3. Measurements of the electron energy loss (spectra) of He, Ar, Kr, and Xe at different incident energies and scattering angles. The inelastic cross sections of the prominent peaks of Ar, Kr, and Xe are deduced from the relative intensity of the inelastic and elastic peaks. In addition, the dependence of the differential excitation functions of Ar, Kr, and Xe on electron impact energy are obtained (see chapter 5).

4. The first observation of an electron-photon angular correlation measured by the delayed coincidence between electrons scattered inelastically and the subsequent photons emitted in the decay of the $^3P_1$ and $^1P_1$ states of Kr (see chapter 6).

CHAPTER 2

THE APPARATUS

2.1 Outline of the apparatus

The apparatus initially consisted of two differentially pumped chambers, the oven chamber and excitation chamber. In this experiment, only the excitation chamber was used, after modifications to the gas nozzle mounting allowed the removal of the oven chamber. The excitation chamber contained a 127^{o} electrostatic electron monochromator and analyser, the electron and photon detectors and, of course, the gas nozzle. This chamber was separated from the diffusion pump by means of an electro-pneumatically operated gate valve which prevented the pumping oil from reaching the excitation chamber in case of power failure. The pump was a four stage oil diffusion pump with a speed of 3000 ℓ/sec (for air). The pumping fluid oil used was Santovac 5. The pump was cooled by two water cooled chevron baffles. A two stage rotary pump with a speed of 100 m^3/h was used as a forepump. Two types of vacuum seals (Viton O ring and indium wires) were used. The excitation chamber was made of non-magnetic stainless steel and was baked by a heater wire wrapped around the chamber. Baking temperatures did not exceed $120^{o}C$ to avoid damage to the vacuum seals. Typical background pressures obtained were $3*10^{-7}$ torr.

2.2 Helmholtz Coils

With any electrostatic energy selector, it is necessary to cancel the earth's magnetic field. Neutralisation of the earth's field is achieved by three mutually perpendicular pairs of Helmholtz coils

surrounding the scattering chamber. Each coil consists of 50 turns of copper wire which are wound on an aluminium frame. Typical residual fields measured with the Helmholtz coils in operation were a few milligauss (10 mG).

2.3 Protection circuit

An interlock system was designed to protect the machine in case of water failure, steep pressure rise and power failure. The machine would switch off if any of these emergencies arose. At the same time the gate valve would shut, thereby isolating the excitation chamber from the diffusion pump. All external power supplies to the system would also switch off.

2.4 Leak detection

A quadrupole mass spectrometer (Balzer model QMG 101) was used as a leak detector. The main feature of this unit is its high sensitivity and good resolution. This unit was connected to the apparatus continuously for detecting sudden leaks and tracing the gas under study. Helium gas was used as a test gas. A typical residual gas spectrum traced by a chart recorder is shown in Fig. (2.1).

2.5 Atomic beam source

A well-defined atomic beam is produced by the effusion of the gas through a nozzle. This nozzle consists of a multicapillary array which is mounted in a non-magnetic stainless steel tube of 2mm diameter and 27mm length. The distance between the end of the tube and the centre of the interaction region can be adjusted from inside the system. The

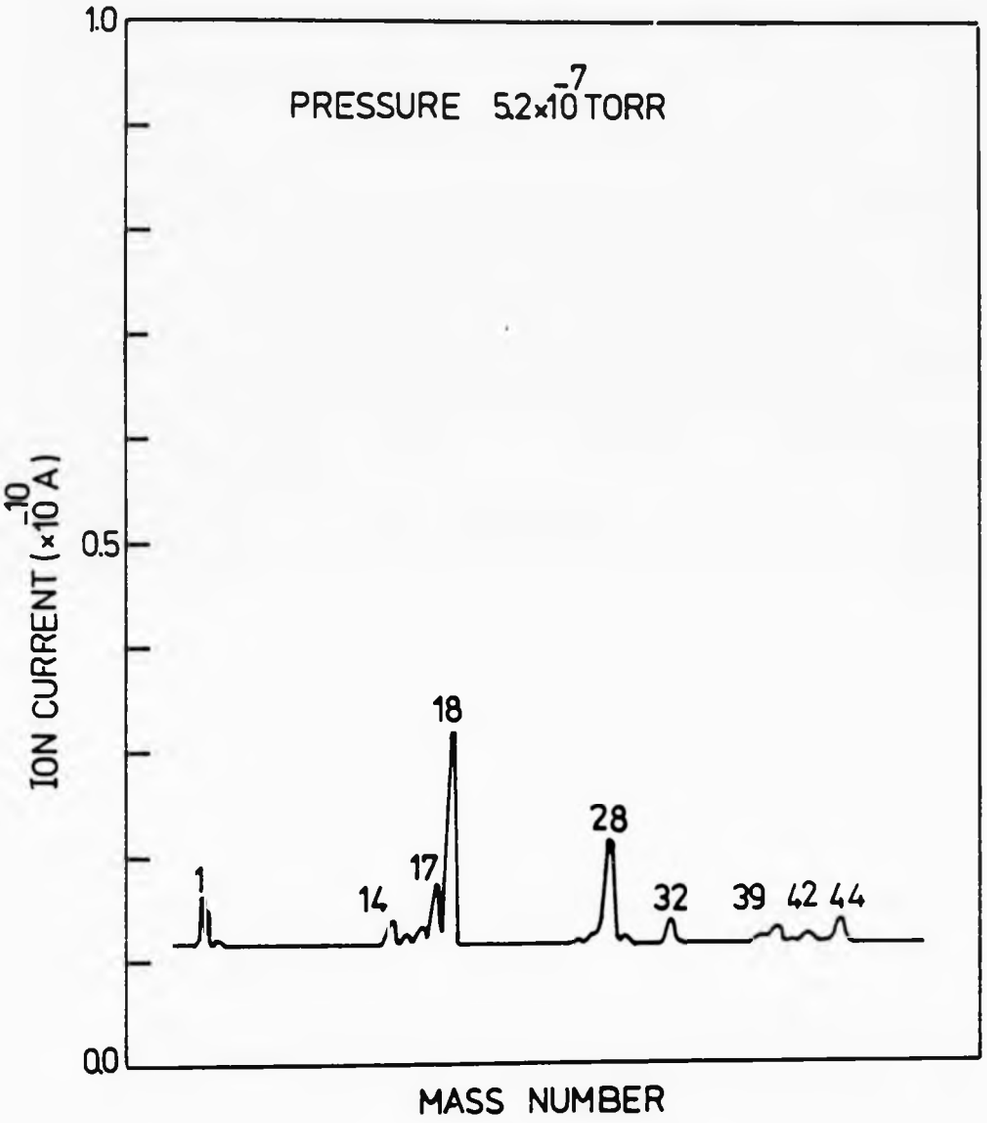

Fig. (2.1): A typical residual gas spectrum

rare gases used are of research grade.

2.6 Electrostatic energy selectors (monochromator and analyser)

2.6.1 Introduction

In many electron collision experiments, it is important to improve the energy spread (ΔE) of the electron beam emitted from a thermionic emitter which has a half width of about 0.25 eV at the best. The energy spread (ΔE) can be defined as energy between the half maximum points of the electron beam current distribution (FWHM). When electrons escape from such an emitter, the current distribution can be described by a Maxwell distribution

$$I(E) = I_o(\frac{E}{kT})\ e^{-E/kT} \qquad (2.1)$$

where I_o is the total current, E is the electron energy measured in eV, T is the emitter temperature measured in K, and k is Boltzman constant.

At low electron beam currents, the energy distribution is Maxwellian at a temperature corresponding to the emitter temperature, but as the current is increased toward the space charge limit the energy width increases and the energy distribution is no longer Maxwellian (Simpson and Kuyatt (1966)).

Many instruments have been described to provide an electron beam of low energy spread and have been used in the field of electron spectroscopy (see, for example, high resolution experiments by Williams (1976) and Brunt et al (1977c)). Among electrostatic analysers, there are two types commonly used in electron impact work. These are the 180^o hemispherical and the 127^o cylindrical analysers. A 180^o hemispherical

analyser was described by Purcell (1938). It provides three dimensional focusing and has axial symmetry. Kuyatt and Simpson (1967) have given a further description of such a device and studied the effect of the space charge on its operation. A 127^{o} cylindrical analyser was first suggested by Hughes and Rojansky (1929). They described the path of electrons in a field of ($X = -A/r$) resulting from the potential difference between a pair of concentric cylinders. They showed that focusing of electrons occurs in this device at $\pi/\sqrt{2} = 127.17^{o}$. The general transmission function of the analysers is given by

$$\frac{\Delta r}{r_o} = A\frac{\Delta E}{E_o} - B\alpha^2 - C\beta^2 \quad . \tag{2.2}$$

where r_o is the radius of the central path of electrons through the analyser ($r_o = \frac{r_1+r_2}{2}$), Δr is the slit width, E_o is the mean energy, ΔE is the energy spread measured in terms of full width at half maximum intensity, α is the angular divergent of the beam in the plane of drawing (Fig. 2.2), and β is the corresponding angle perpendicular to this plane. A, B, and C are constants and have different values for various analysers.

For a 127^{o} cylindrical analyser,

$$A = 1 \quad B = 4/3 \quad \text{and} \quad C = 1.$$

The energy resoultion for a 127^{o} analyser is therefore given by

$$\frac{\Delta E}{E_o} = \frac{\Delta r}{r_o} + \frac{4}{3}\alpha^2 + \beta^2 \tag{2.3}$$

Fig. (2.2) shows the trajectory of electrons between a pair of concentric cylinders of radii r_1 and r_2 ($r_1 < r_2$) with the mean energy $E_o = eV_o$. The entrance and exit slits are separated by 127.17^{o}. The

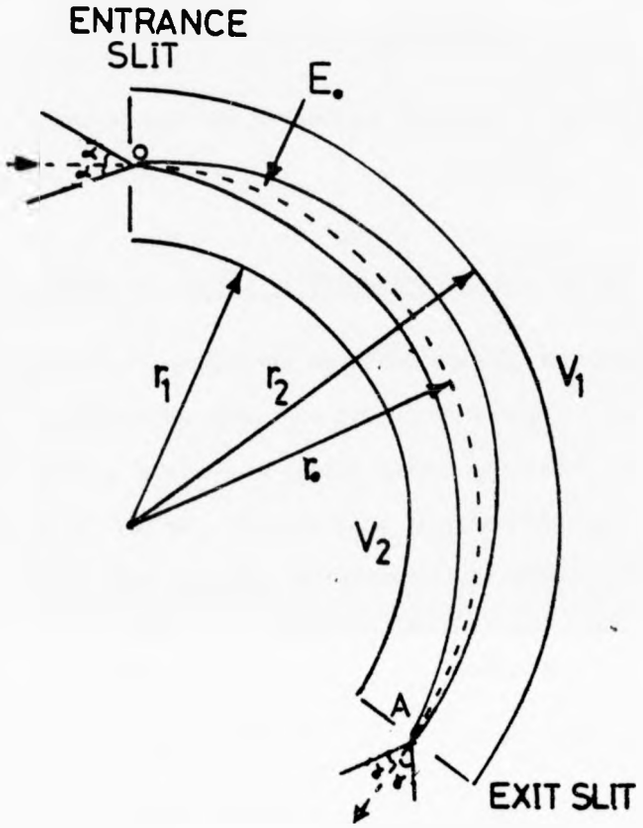

Fig. (2.2): Electron trajectory in 127^{o} electrostatic analyser.

field produced by the cylinders is given by

$$E(r) = \frac{1}{r} \frac{V_1 - V_2}{\ln (r_2/r_1)} \qquad (2.4)$$

where V_1 and V_2 are the potentials applied to the outer and inner cylinders respectively.

2.6.2 Mechanical design of the monochromator system

The 127^{o} electrostatic selector used in this experiment, built by Raible (1974) and based on the principal design of Marmet and Kerwin (1960), is designed to achieve an energy spread and hence energy resolution of the order of 100 meV. The details of this selector are shown in Fig. (2.3). The geometrical parameters of this system are

$r_{\text{outer grid}} = 18.0$ mm $r_{\text{inner grid}} = 12.0$ mm

$r_{\text{outer plate}} = 22.0$ mm $r_{\text{inner plate}} = 8.0$ mm

Mean radius = 15 mm

Height of the slit = 5.0 mm

Width of the slit can be varied

All the elements of this selector are gold plated from oxygen-free copper except the entrance and exit slits which are made of molybdenum. The deflector grids are made of a tungsten mesh of 87% transparancy and are mounted on special support frames. This monochromator can be heated up to 200^{o}C by outer shield which is built as a heater jacket. All the elements of this selector are covered with soot in order to reduce the chance of electrons being reflected off the walls.

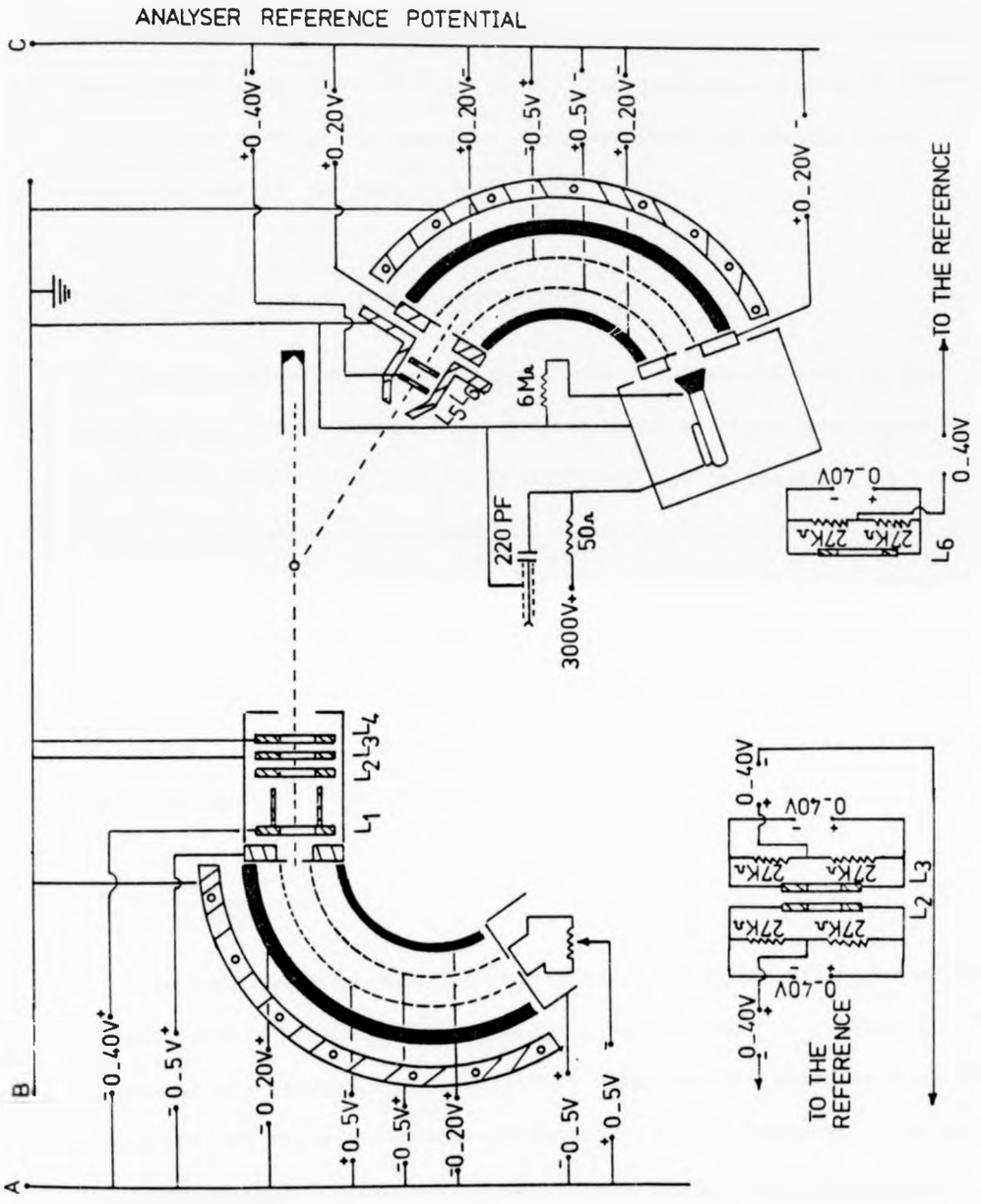

Fig. (2.3): A schematic diagram of a 127^{o} electrostatic monochromator and analyser assembly

2.6.3 Electron gun for monochromator

A simple electron gun is used in this experiment, consisting of a tungsten wire of 0.1 mm diameter mounted along the entrance slit of the monochromator, as shown in Fig. (2.3). The tungsten filament is housed inside a box made of non-magnetic stainless steel to prevent stray electrons leaving the gun.

2.6.4 Output lens system for monochromator

The electrons leaving the monochromator are accelerated to the required energy and focused by a three element aperture lens system of the Read type (1970) of 5 mm diameter and 2.5 mm spacings. A schematic diagram of these lenses is shown in Fig. (2.3). L_2 and L_3 are split lenses mounted perpendicular to each other allowing these lenses to be used as deflectors to produce a well focused and aligned electron beam. A special box is made of molybdenum sheeting to house these lenses which are also made of molybdenum. The spacers between the lenses are made of boron nitride.

2.6.5 Faraday cup

The electron beam emerging from the monochromator after traversing the interaction region is collected by a Faraday cup. A schematic diagram of the Faraday cup used in this experiment is shown in Fig. (2.4) It consists of three concentric cylinders of inner diameters 4, 8, and 12 mm respectively. In order to obtain a high collector efficiency, the inner cylinder is made twelve times deeper than its diameter. In addition, the three cylinders are sooted to reduce the number of reflected

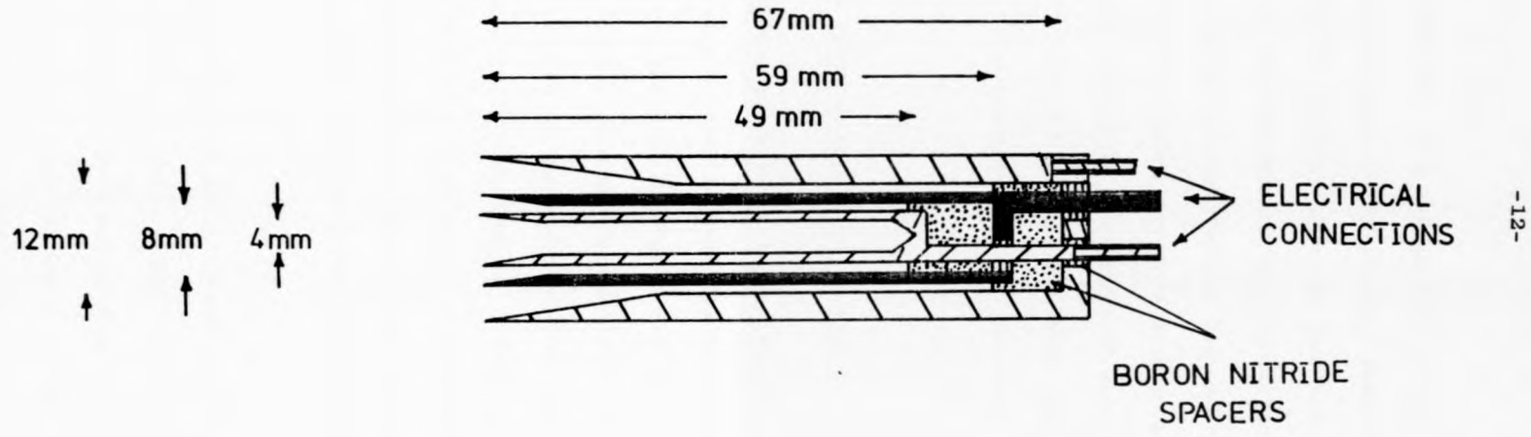

Fig. (2.4): A schematic diagram of the Faraday cup

and secondary electrons. The aim of this design was to measure the divergence of the incident electron beam. When measuring excitation functions and angular distributions, an aperture of 4 mm diameter was placed in front of the Faraday cup to stop reflected electrons from the inner surfaces reaching the interaction region. The inner cup is used to measure the electron current with an electrometer (Keithley 602). The Faraday cup is mounted at a distance of about 15 mm away from the centre of the interaction region. The three cups are made of non-magnetic stainless steel. The spacers are made from boron nitride and oxide ceramic rods.

2.6.6 Scattered electron collector (analyser)

Scattered electrons from the interaction region are analysed by a 127^{o} electrostatic system identical to the monochromator. These electrons enter the analyser through a slit of width 1.5 mm and are then decelerated and focused onto the entrance slit of the analyser by a two lens system (L_5 and L_6) as shown in Fig. (2.3). L_6 is a split lens which can be also used as a deflector. Electrons transmitted through the analyser are detected by an electron channeltron. These lenses are made of non-magnetic stainless steel. The spacers are made of oxide ceramic. The procedure used to check the operation of this analyser is as follows.

The scattering angle of the analyser is set parallel to the direction of the incident beam. A high electron beam current is thereby obtained with a relatively poor energy resolution. These electrons are focused onto the entrance slit (by means of the above lenses L_5 and L_6), and then pass through the analyser. Finally, these electrons are detected by an electron channeltron in connection with an electrometer (in these measurements no voltage is applied to the electron channeltron

since it is only used as a Faraday cup to monitor the electron beam current). The electron beam profiles are traced using an X-Y recorder. Typical results are shown in Fig. (2.5). The analyser is used in this way for detecting the elastic peak and energy loss spectra for a number of gases as explained in Chapter 5.

2.7 Ultraviolet detectors

Two kinds of photon detector are used in this experiment -

1. Photon detector (Bendix BX 762)

This photo tube is equipped with an MgF_2 window with a short wavelength cut-off at 1140 Å. The cathode has a funnel shape coated with a caesium iodide(CsI) and followed by a channeltron for electron multiplication. The quantum efficiences of the CsI of the photo cathode at the wavelengths 2000, 1700, 1500, and 1300 Å are 0.008%, 2%, 5%, and 8% respectively and are suitable for the detection of Lyman-α photons (1216 Å). The dark count rate of this tube is 0.2 count/sec. and the gain is of $\sim 10^8$. The voltage to operate the detector is about 3200 volts. In the counting mode, the output is characterised by a narrow pulse height distribution. The tube is housed inside a non-magnetic stainless steel tube. In order to limit the solid angle of the radiation entering the tube, a two aperture system is used Kuyatt (1968). The two apertures are of 4 mm diameter and spaced 10 mm apart as shown in Fig. (2.6a). The voltage divider for the tube and the decoupling capacitor are mounted directly to the tube. The electrical connections are kept as short as possible to avoid interference effects. The detector is positioned on a turntable which can be rotated from outside the chamber through an angular range from 67° to 112.5°. The distance between the detector

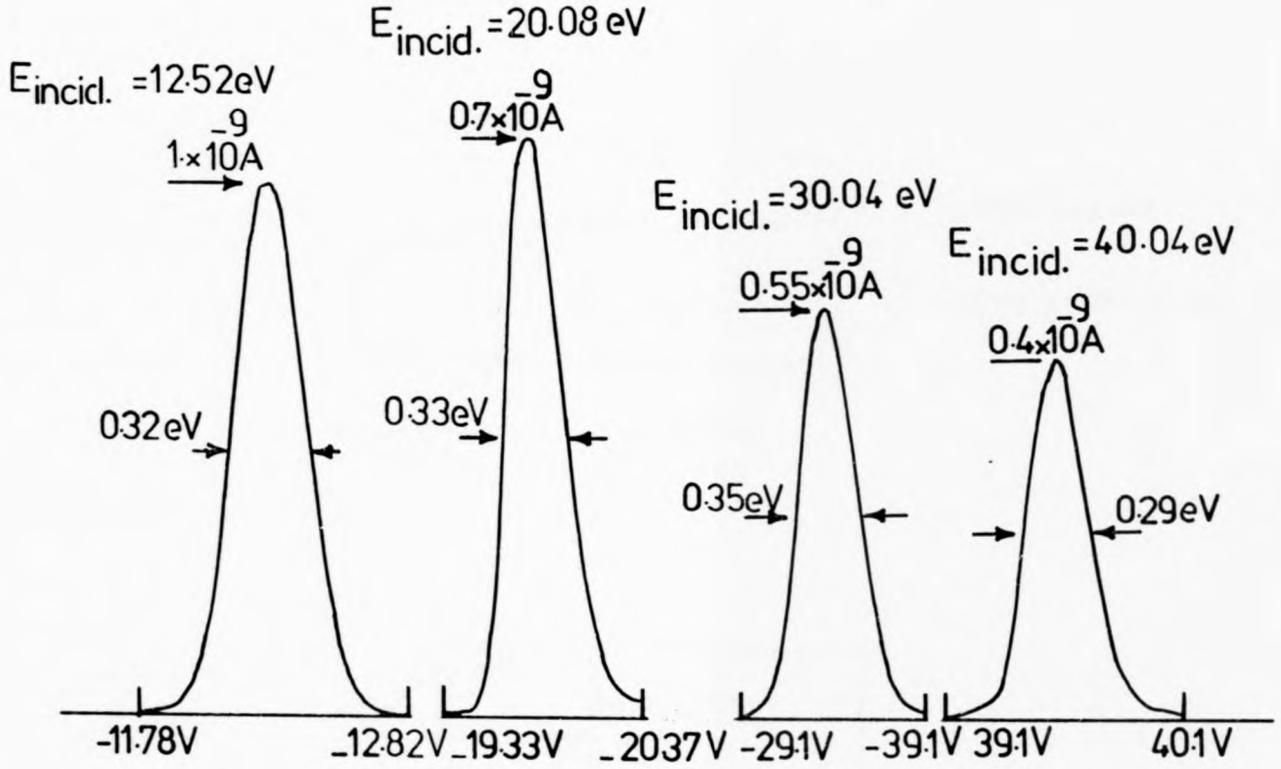

Fig. (2.5): Electron beam profiles

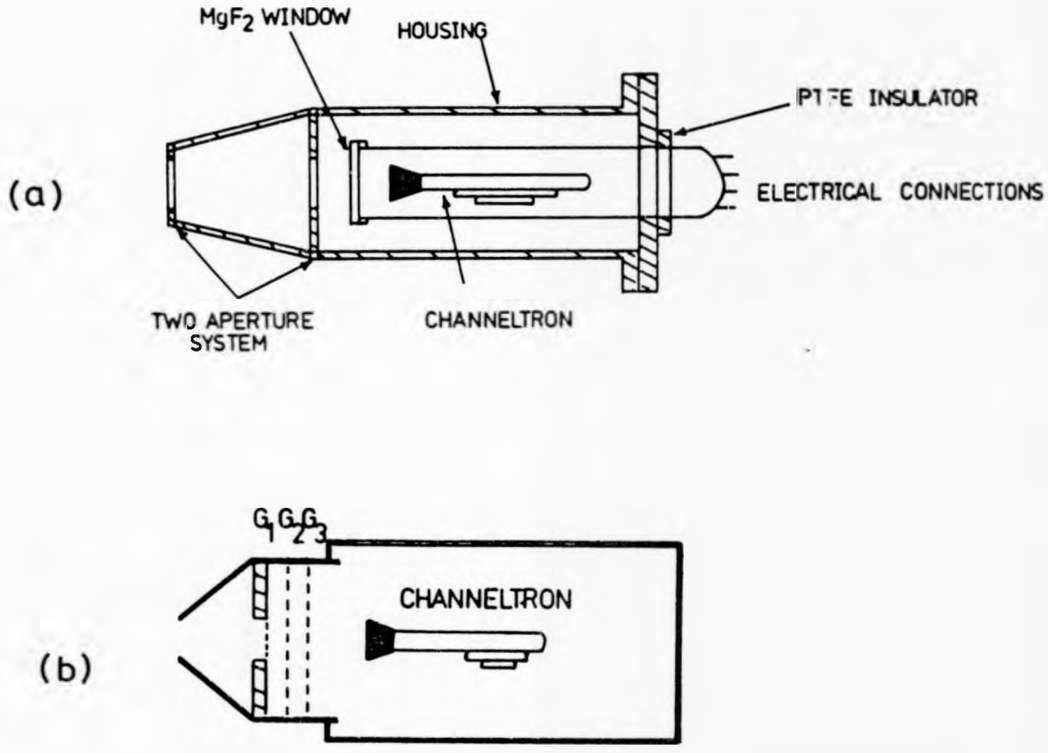

Fig. (2.6): The upper part shows the photon detector equipped with MgF_2 window while the lower part shows an electron channeltron with the retarding grids used as a photon detector

and the centre of the interaction region is about 10 mm. This detector is used for the detection of the UV photons emitted from Kr and Xe because the wavelengths in these cases are longer than 1140 Å.

2. A channeltron electron multiplier (CEM) (Mullard type B318BL)

A schematic diagram of this detector is shown in Fig. (2.6b). Three grids, each of 80% transparency, are mounted in front of the detector and biased to prevent charged particles from entering the CEM. The detector is also housed inside a non-magnetic stainless steel tube. This detector operated at 3500 volts and is used for the detection of the UV photons emitted from He, Ne and Ar because the wavelengths of these transitions are shorter than 1140 Å (short wavelength cut-off of the MgF_2 window).

2.8 Alignment of electron optics and detection system

To study the angular intensity distribution of photons or electrons, an accurate alignment of all components involved is necessary (any misalignment for example of the photon detector with the whole interaction region will cause an alteration of the angular intensity distribution). This means that the axis of the atomic beam nozzle, the axis passing through the centre of the output lens of the monochromator, the axis passing through the centre of the nozzle in front of the photon detector, and the axis passing through the centre of the Faraday cup must meet at one point, which is the centre of the interaction region. This alignment is achieved by using oxide ceramic rods of 1.5 mm diameter which are mounted at the centre of brass rods fitted to each of the output lenses of the monochromator and to the nozzle in front of the photon detector as shown in Fig. (2.7).

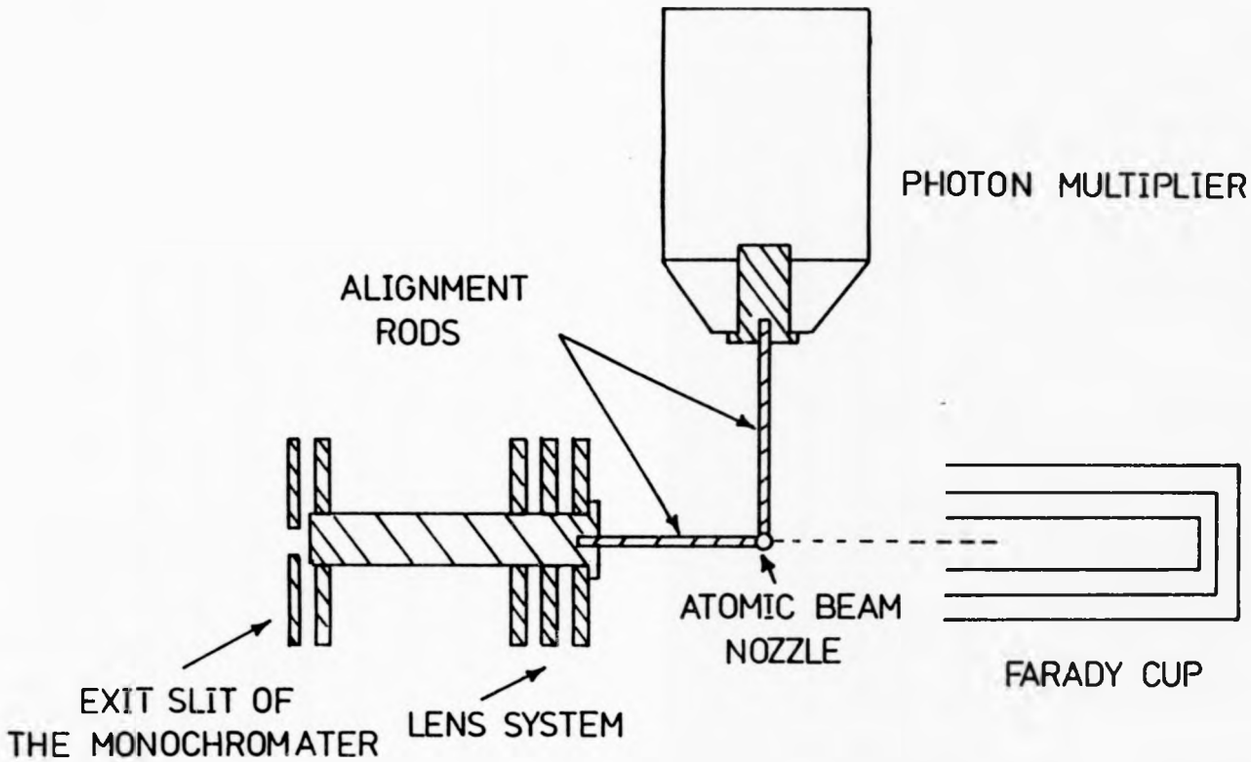

Fig. (2.7): The alignment rods fitted in front of the photon detector and in the output lens system of the monochromator.

2.9 Electronics and data collection

2.9.1 Timing electronics

The block diagram of the electron-photon coincidence circuit is shown in Fig. (2.8). The signal from each of the electron and photon detectors is passed through a fast amplifier (LRS model 234). The amplified pulses are fed into a constant fraction timing discriminator CFTD (Ortec model 473). The photon timing pulse from CFTD provides a start pulse to the time to amplitude converter TAC (Ortec model 467). The electron timing pulse is delayed and provides a stop signal. The amplitude of the TAC output signal is proportional to the difference between start and stop pulses. The pulse height distribution spectrum from TAC is recorded in a multichannel analyser.

2.9.2 Multichannel analyser (MCA)

The excitation function for UV photons from rare gas atoms is obtained by measuring the number of photons as a function of incident energy. In these measurements a multichannel analyser (Intertechnique DIDAC 800) is used in its multiscaling mode. This analyser has 800 channels and any number between 0 - 800 channel can be preselected. In the multiscaling mode the channels are addressed sequentically by a clock module and the counting time per channel can be varied. The parallel output from the address register is fed into a digital to analogue device which converts the digital output into a ramp voltage between 0 - 8 volts for the full number of 800 channels. The data from the MCA can be printed out on paper tape by using a teletype machine.

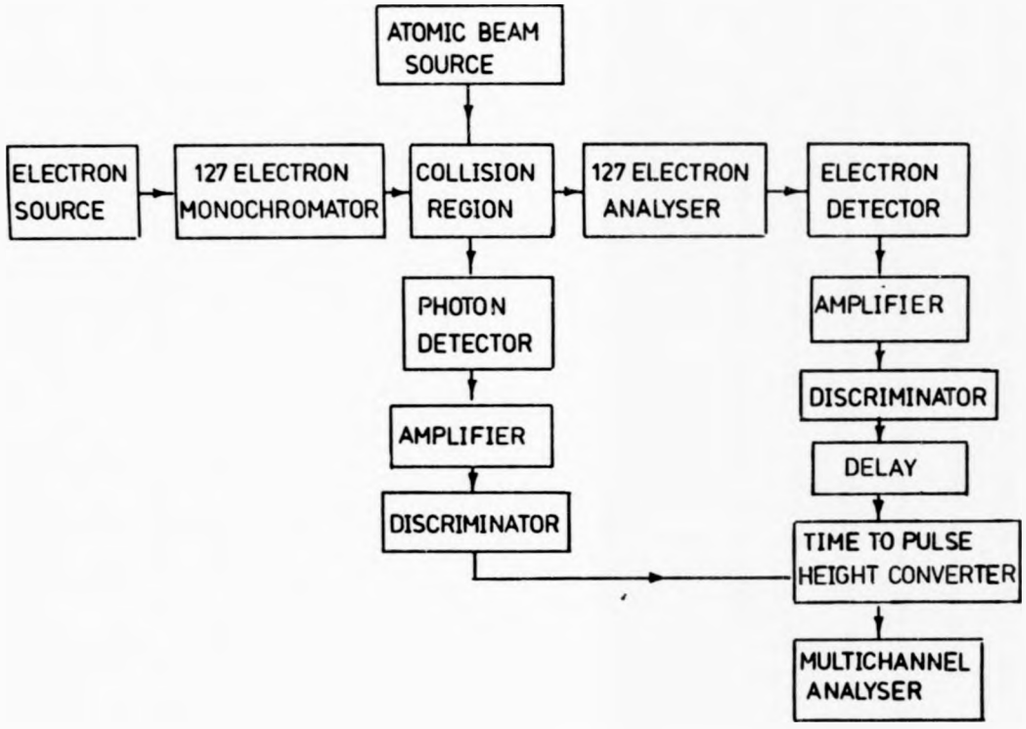

Fig. (2.8): A block diagram of the electron-photon coincidence circuit

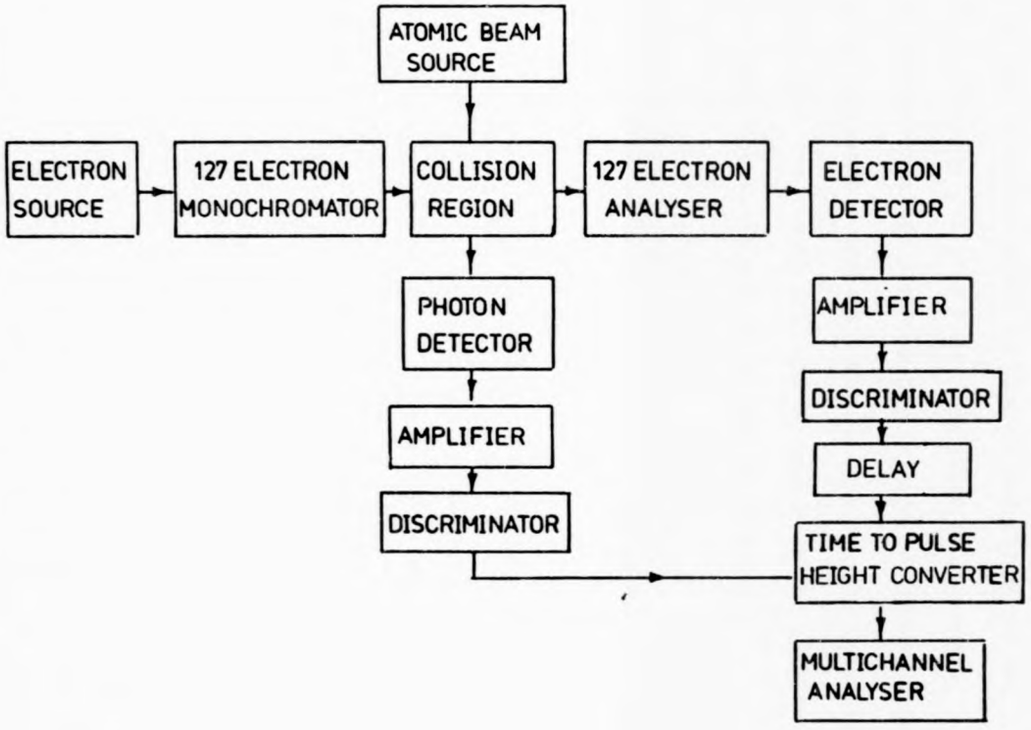

Fig. (2.8): A block diagram of the electron-photon coincidence circuit

2.10 Electrical power supplies

A schematic diagram of the electronic circuit for the electron spectrometer is shown in Fig. (2.3). All the voltages required for the various elements of the monochromator, analyser and lens system are derived from individual stabilized power supplies. These voltages are relative to one reference point in each of monochromator and analyser. This reference point is biased relative to the earth potential. A constant current power supply is used for the tungsten filament. Three independent constant current supplies are used for the Helmholtz coils. Two stabilised high voltage supplies (Fluke model 4088) are used for the electron and photon detectors.

CHAPTER 3

STRUCTURE IN NEAR THRESHOLD ELECTRON EXCITATION OF RARE GAS ATOMS

3.1 Introduction

Within the last two decades, great progress has been made in the field of resonances in electron-atom collisions (Schulz (1973) and Heddle (1976)). The phenomenon of resonances in electron-atom scattering can be explained by the formation of compound states (temporary negative ions) having a short lifetime of the order 10^{-13} sec and then decaying into the original components. The resonance process can be represented by

$$e(E_{res}) + A(\text{target}) \rightarrow A^{-*} \rightarrow \begin{cases} A^{*} + e(E_{res} - E_n) \\ A + h\nu \text{ photon} \end{cases}$$

The compound state can be described as doublet or multiplet excited states of ions and thus formed by adding the impact electron into an excited state of a target atom. Such compound states are called core excited resonance states. There are two types of such resonances, namely, type I (closed channel or feshbach resonances) and type II (open channel or shape resonances).

Type I : can occur when the interaction potential between the impact electron and an excited state of an atom is strong enough to support a bound state. The energy positions of these resonances lie below the possible excited states of an atom and are subject to certain selection rules of autoionization. The selection rules are that the parity and the angular momentum must be conserved. These types of resonances are distinguished by having a relatively long lifetime and a

narrow width.

Type II : In this case the impact electron is trapped by a penetrable barrier formed by the angular momentum of the electron with L>0 (i.e., P, d, and f wave resonances). The energy positions of these resonances lie above the excited states of the atom and preferentially decay to the parent state. These types of resonances have a relatively short lifetime and their widths are large.

The first theoretical prediction of the existence of compound states in electron-atom scattering was postulated by Baranger and Gerjuoy (1957), (1958). These ideas were confirmed by Burke and Schey (1962) who predicted resonances in the electron scattering cross section of electrons on atomic hydrogen. In (1963) Schulz reported a sharp resonance at an electron energy 19.3 eV in the elastic scattering of electrons on helium at a scattering angle of 72°. The energy position of this resonance is often used for the purpose of energy calibration. The classification of these resonances are classified in terms of spectroscopic configurations (see, for example, Read et al (1976) and Spence (1977)).

The heavy rare gases Ne, Ar, Kr, and Xe show a marked similarity in terms of their resonances. These resonances consist of two s electrons attached to the positive ion core (np^5). The positive ion core is therefore a doublet (J = 1/2 and J = 3/2). The lowest resonance states of the above gases are ($2p^5\ 3s^2$), ($3p^5\ 4s^2$), ($4p^5\ 5s^2$), and ($5p^5\ 6s^2$) $^2P_{1/2,3/2}$ respectively. The lower resonance $^2P_{3/2}$ for Kr and Xe lies approximately 0.5 eV below the inelastic threshold, while the upper resonance $^2P_{1/2}$ lies above the inelastic threshold. The upper resonance decays strongly into the $^3P_1$ channel but the lower resonances $^2P_{3/2,1/2}$ for Ne and Ar are located approximately 0.5 eV below the inelastic

threshold.

The doublet splitting of the above resonances are closely related to the fine structure of the ion core (Kuyatt (1965)). The schematic energy level diagrams for the above gases (Candler (1964)) are shown in Figs. (3.1) and (3.2).

The excitation functions are measured by observing the UV photons emitted during the decay of the first excited states of Kr, Xe, Ne, Ar, and He at different photon angles with respect to the electron beam direction. These measurements have been performed in the low gas pressure region where radiation trapping is negligible (gas inlet pressure is measured in the excitation chamber with an ionization gauge).

Since metastable atoms are detected as well by the CEM detector, the energy scale for He, Ne, and Ar is calibrated with respect to threshold excitation of metastable states. The energy positions of the prominent features of these resonances show good agreement with the total cross section for metastable excitation by Pichanic and Simpson (1968) (metastable atoms $^3P_0$ and $^3P_2$ are detected in the interaction region by electron ejection from a metal surface. The yield was studied as a function of electron energy at an energy resolution of 50 meV). The results for Kr and Xe are also compared with the results of Pichanic and Simpson (1968).

The features in the excitation function of all these gases are also compared with the transmission experiment of Sanche and Schulz (1972) and with the excitation function for UV photons of Brunt et al (1977a,b). Brunt et al detected the UV photons with an open electron channeltron and used a time-of-flight technique to avoid the detection of metastable atoms. The energy resolution was 30 meV. Present results show good agreement with those of the above authors except for helium where the

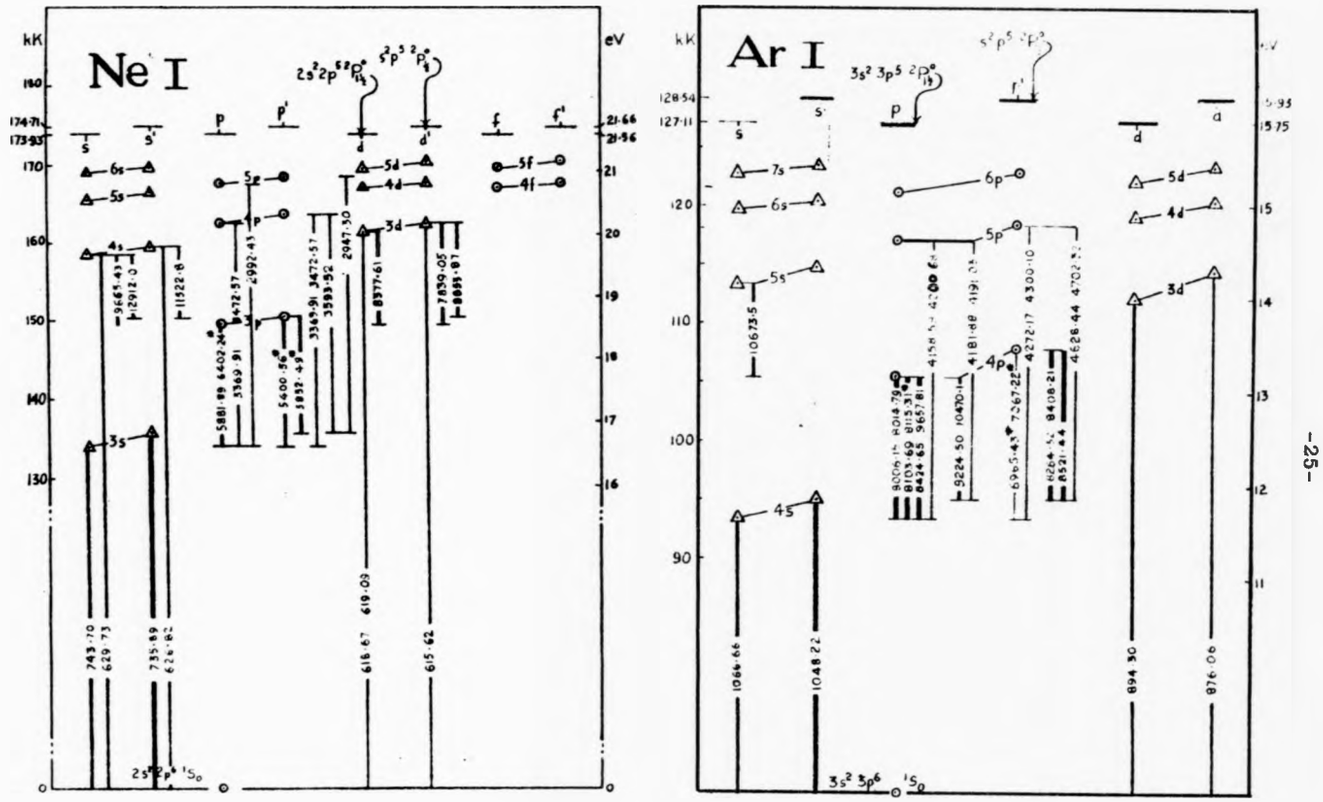

Fig. (3.1): Energy level diagrams for Ne and Ar

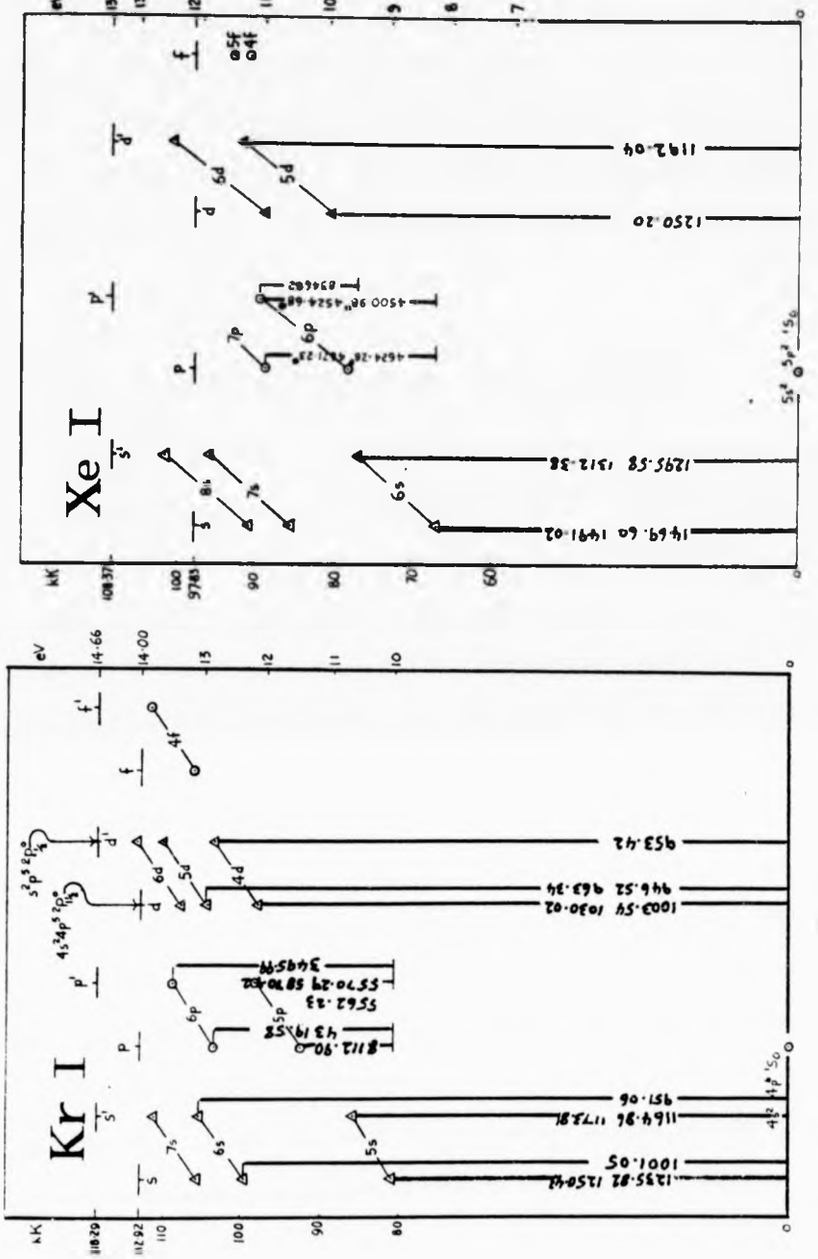

Fig. (3.2): Energy level diagrams for Kr and Xe

features in the excitation function are probably dominated by metastable atoms. The results also show discontinuities in the slope of the excitation function, probably indicating further resonances. The energy resolution of the features is of the order of 100 meV.

3.2 Results

3.2.1 Dependence of the photon signal on the gas pressure

The dependence of the photon signal has been studied over a certain range of gas pressures for each of He, Ne, Ar, Kr and Xe as shown in Figs. (3.3), (3.4) and (3.5). The results show a linear dependence of the photon signal in the specified range of gas pressure, thus indicating that resonance trapping is negligible. Resonance trapping or imprisonment of radiation occurs when the radiation emitted from the excited atoms is absorbed by the ground state of atoms before reaching the detector (Moiseiwitsch and Smith (1968)). Such an effect may significantly alter the nature of the radiation emitted, for if a state is populated by this process instead of by direct collision, the resulting radiation will have no preferred direction. Consequently, the trapped radiation will be re-emitted isotopically, causing an apparent depolarization of the primary impact radiation. To avoid this process, the gas pressure inside the excitation chamber should be operated in the linear region of the photon intensity gas pressure relation.

3.2.2 Measurements of the UV excitation functions of He, Ne, Ar, Kr and Xe

3.2.2.1 Helium

The measurement of the excitation function for UV photons and metastable atoms (at 90^{o} and 75^{o}) is shown in Fig. (3.6). The energy scale is calibrated by normalizing to the threshold excitation energy

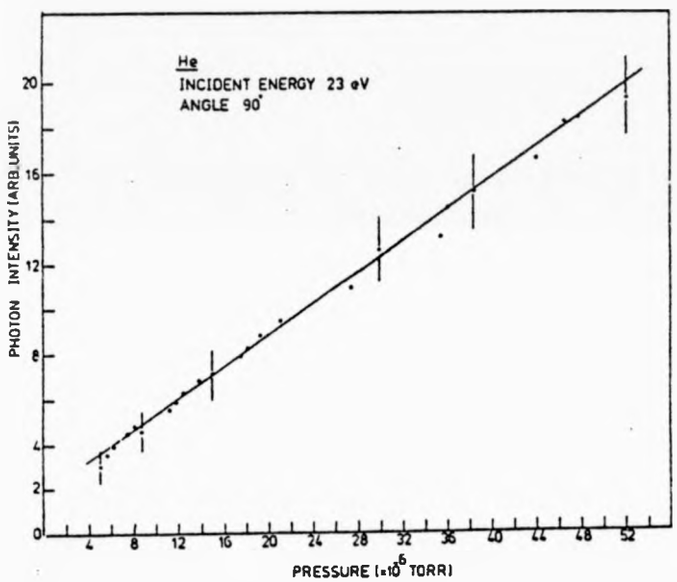

Fig. (3.3): Dependence of the photon intensity on the gas pressure for Helium (1 rms error).

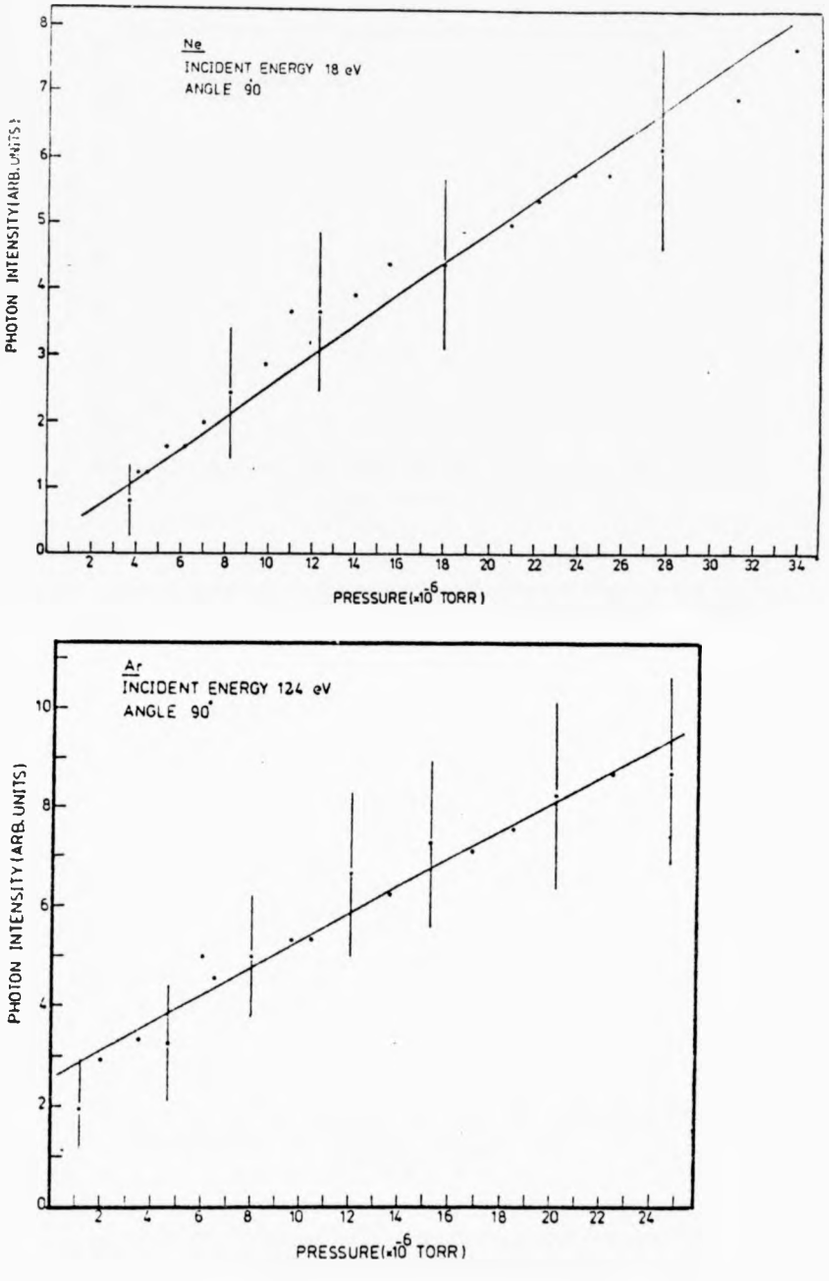

Fig. (3.4): Dependence of the photon intensity on the gas pressure for Neon and Argon (1 rms error)

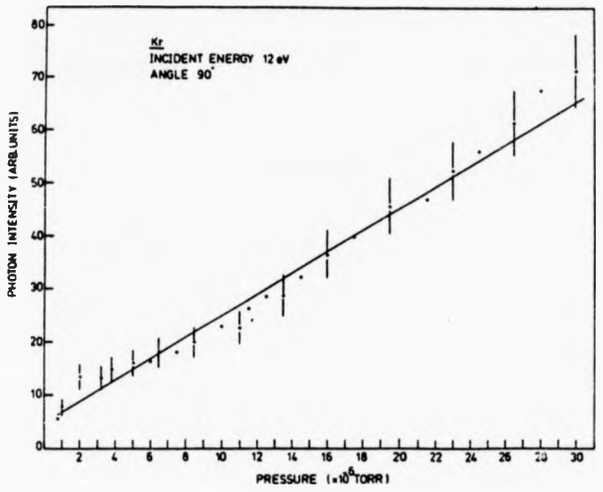

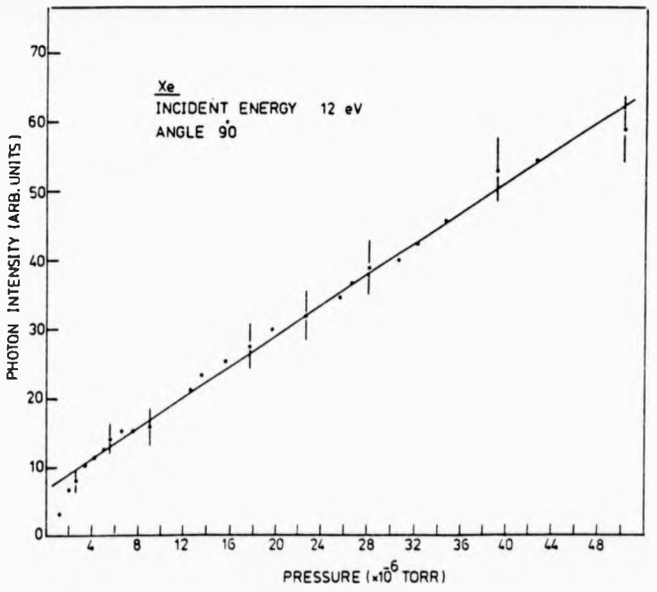

Fig. (3.5): Dependence of the photon intensity on the gas pressure for Kr and Xe (1 rms error)

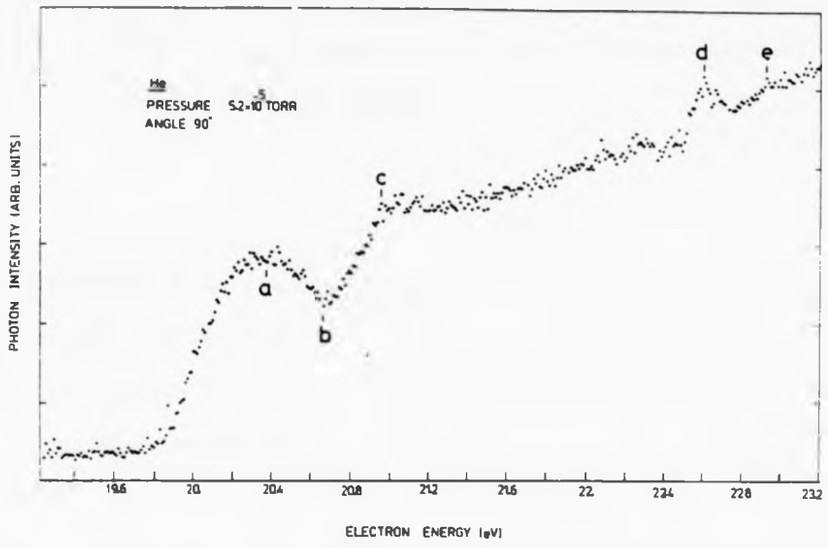

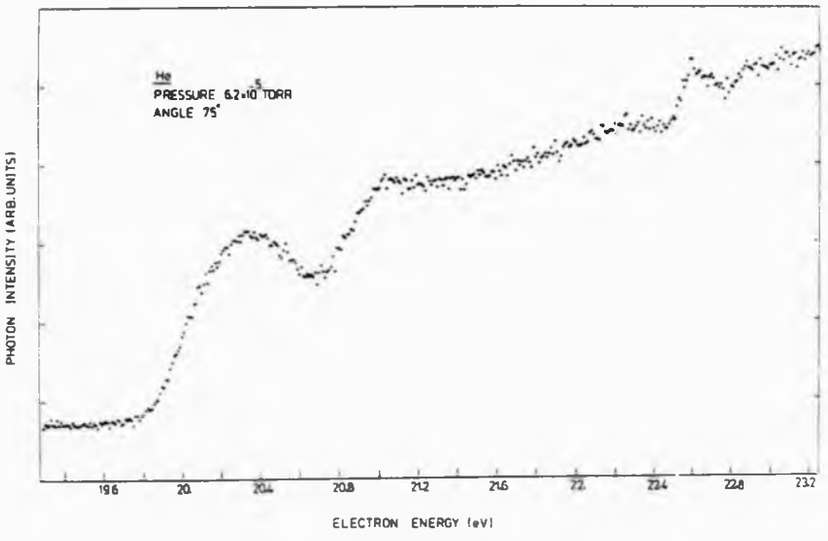

Fig. (3.6): Excitation function of combination of the UV photons and metastable atoms of Helium. The energies of the labelled features are given in Table (3.1)

of the metastable state of He at 18.82 eV (2^3S). The energy width of each channel is 10 meV. The energy positions of resonances shown in the upper part of Fig. (3.6) are summarized in Table (3.1) and compared with results of Pichanic and Simpson (1968).

3.2.2.2 Neon

The measurement of the excitation function for UV photons of the $2p^5\ 3s$ ($^3P_1$ and $^1P_1$) and ($^3P_0$ and $^3P_2$) states of Ne (at 90^o and 105^o) is shown in Fig. (3.7). The $^3P_1$ and $^1P_1$ states decay to $2p^6\ ^1S_0$ ground state by emission of 743.70 Å and 735.89 Å respectively. The energy scale is calibrated by normalizing to the threshold excitation of the metastable state of Ne at 16.62 eV (onset of $^3P_2$ is at 16.62 eV). The energy width of each channel is 10 meV. The energy positions of the resonances shown in the upper part of Fig. (3.7) are compared with other experiments and summarized in Table (3.2). Two sharp resonances are observed at 16.92 eV and 18.65 eV.

3.2.2.3 Argon

The measurement of the excitation function for UV photons of $3p^5\ 4s$ ($^3P_1$ and $^1P_1$) and ($^3P_0$ and $^3P_2$) states of Ar (at 105^o and 90^o) is shown in Fig. (3.8). The $^3P_1$ and $^1P_1$ states decay to the $3p^6\ ^1S_0$ ground state by emission of 1066.66 Å and 1048.22 Å respectively. The energy scale is calibrated by normalizing to the threshold excitation of metastable Ar at 11.55 eV. The energy width of each channel is 10 meV. The energy positions of the resonances shown in the upper part of Fig. (3.8) are compared with other experiments and summarized in Table (3.3).

	Present work	Metastable production Pichanic and Simpson (1968)
a	20.37	20.34
b	20.67	20.62
c	20.96	20.99
d	22.62	22.55
e	22.92	22.86

Table (3.1): Measured energies (eV) of the features in the excitation function for He. Fig. (3.6). These values are estimated to be accurate to ±0.02 eV.

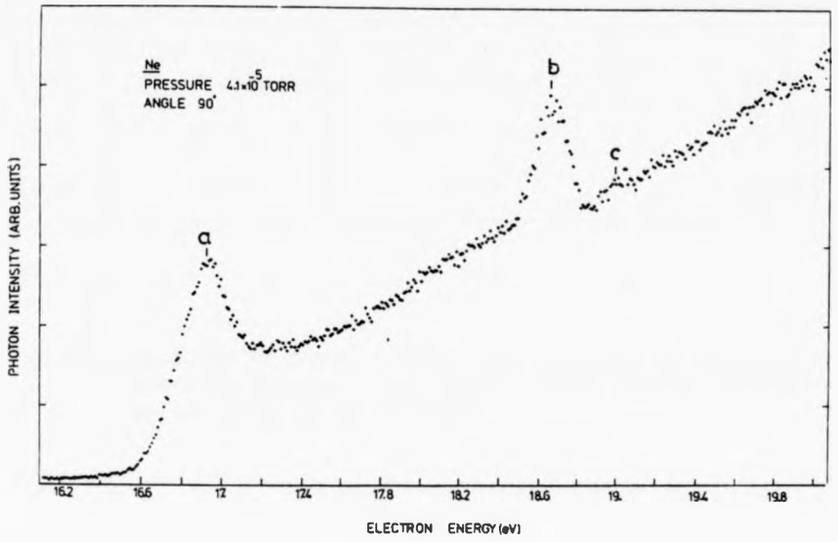

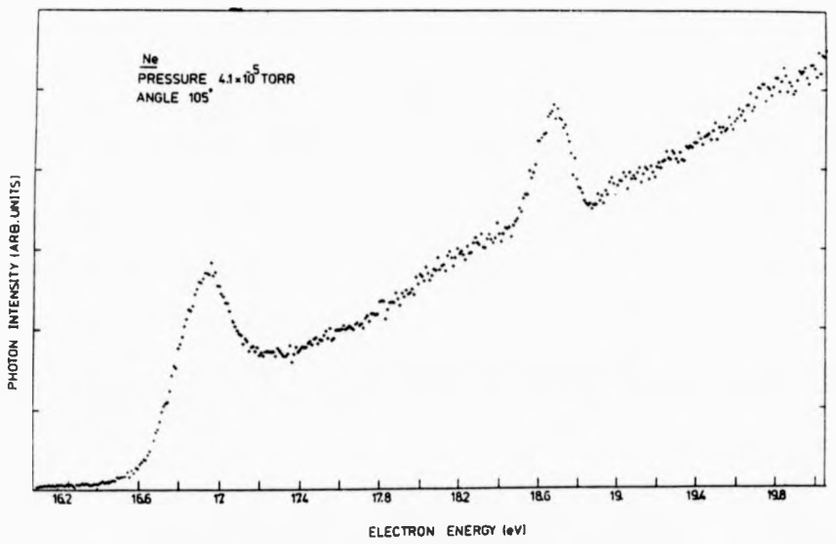

Fig. (3.7): Excitation function of $2p^5$ 3s ($^3P_1$ and $^1P_1$) and ($^3P_0$ and $^3P_2$) states of Ne. The energies of the labelled features are given in Table (3.2)

	Present work	Metastable production Pichanic and Simpson (1968)	Transmission expt. Sanche and Shulz (1972)	UV excitation function Brunt et al (1977a)
a	16.92	16.92	16.85 - 16.91	16.95
b	18.65	18.66	18.65 - 18.70	18.683
c	18.99	18.97	18.95	18.964

Table (3.2): Measured energies (eV) of the features in the excitation function for Ne. Fig. (3.7). These values are estimated to be accurate to ±0.02 eV.

	Present work	Metastable production Pichanic and Simpson (1968)	Transmission expt. Sanche and Schulz (1972)	UV excitation function Brunt et al (1977a)
a	11.76	11.72	11.71	11.664
b	11.91	11.88	11.91	11.845
c	12.67	12.80		
d	13.13	13.08	12.95-13.06-13.11	13.053

Table (3.3): Measured energies (eV) of the features in the excitation function for Ar. Fig. (3.8). These values are estimated to be accurate to ±0.02 eV.

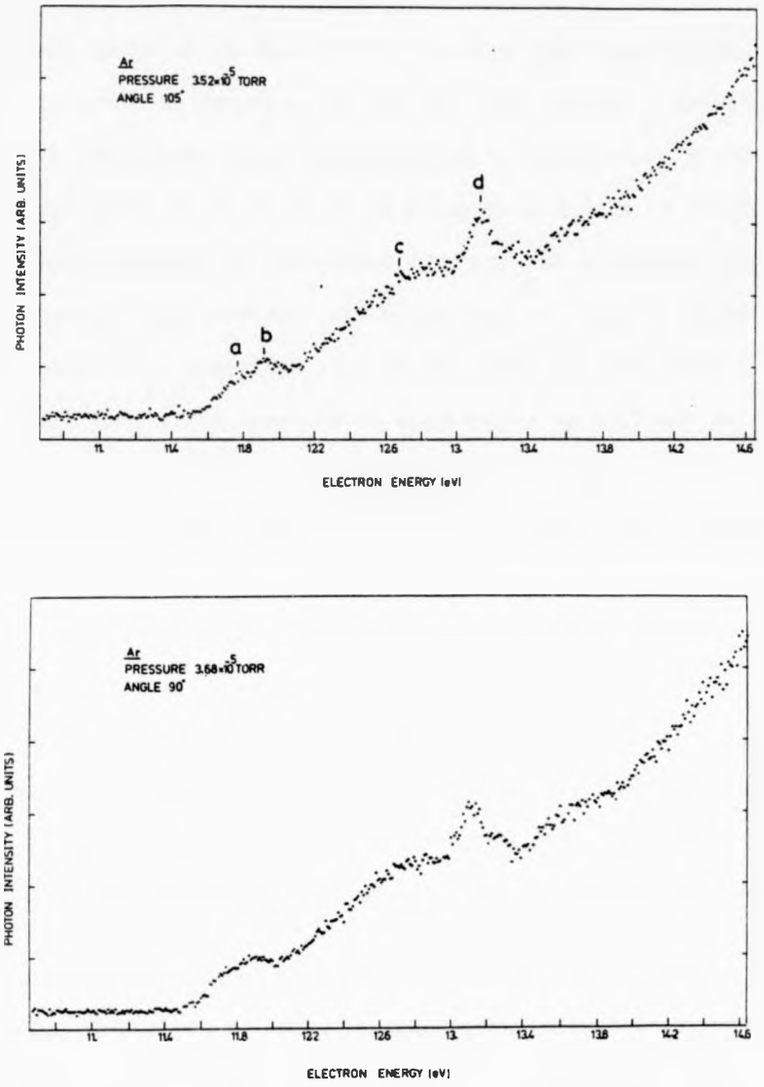

Fig. (3.8): Excitation function of $3p^5$ 4s ($^3P_1$ and $^1P_1$) and ($^3P_0$ and $^3P_2$) states of Argon. The energies of the labelled features are given in Table (3.3)

3.2.2.4 Krypton

The measurement of the excitation function of UV photons for the $4p^5\ 5s\ ^3P_1$ and $^1P_1$ states of Kr (at 90^o with respect to the electron beam direction) is shown in Fig. (3.9). These states decay to the $4P^6\ ^1S_o$ ground state by emission of 1235.82 Å and 1164.86 Å radiation respectively. The energy scale is calibrated by normalizing the strong peak in the spectrum to 10.14 eV on the basis of the work of Koschmieder (1974) who used a mixture of helium and krypton, and calibrated the energy scale by observing simultaneously the helium elastic peak at 19.35 eV and the krypton excitation function. The energy width of each channel is 12.5 meV. This excitation function is extended up to 14.75 eV as shown in Fig. (3.10). Figs. (3.9) and (3.10) show, by looking at the energy levels, that in the region below 10.6 eV the $^3P_1$ state can be excited and a strong resonance appears in this channel (a similar strong resonance is found in the previous experiments of the total cross section for metastable excitation at 10.05 eV by Pichanic and Simpson (1968) and inelastic cross section scattering by Swanson et al (1973 a). At 10.60 eV there is a change in slope of the excitation function, indicating excitation of the $^1P_1$ state. Beyond this region there are discontinuities in the slope of the excitation function, indicating further resonances.

A further measurement of this excitation function is made in the region between 20 - 45 eV as shown in Fig. (3.11). In this figure the photon intensity is normalized with respect to the electron beam current (count/nA). The energy positions of the resonances shown in Fig. (3.9) are compared with other experiments and summarized in Table (3.4).

3.2.2.5 Xenon

The measurement of the excitation function for UV photons of $5p^5\ 6s\ ^3P_1$ and $^1P_1$ states of Xe (at 90^o and 75^o) is shown in Fig. (3.12).

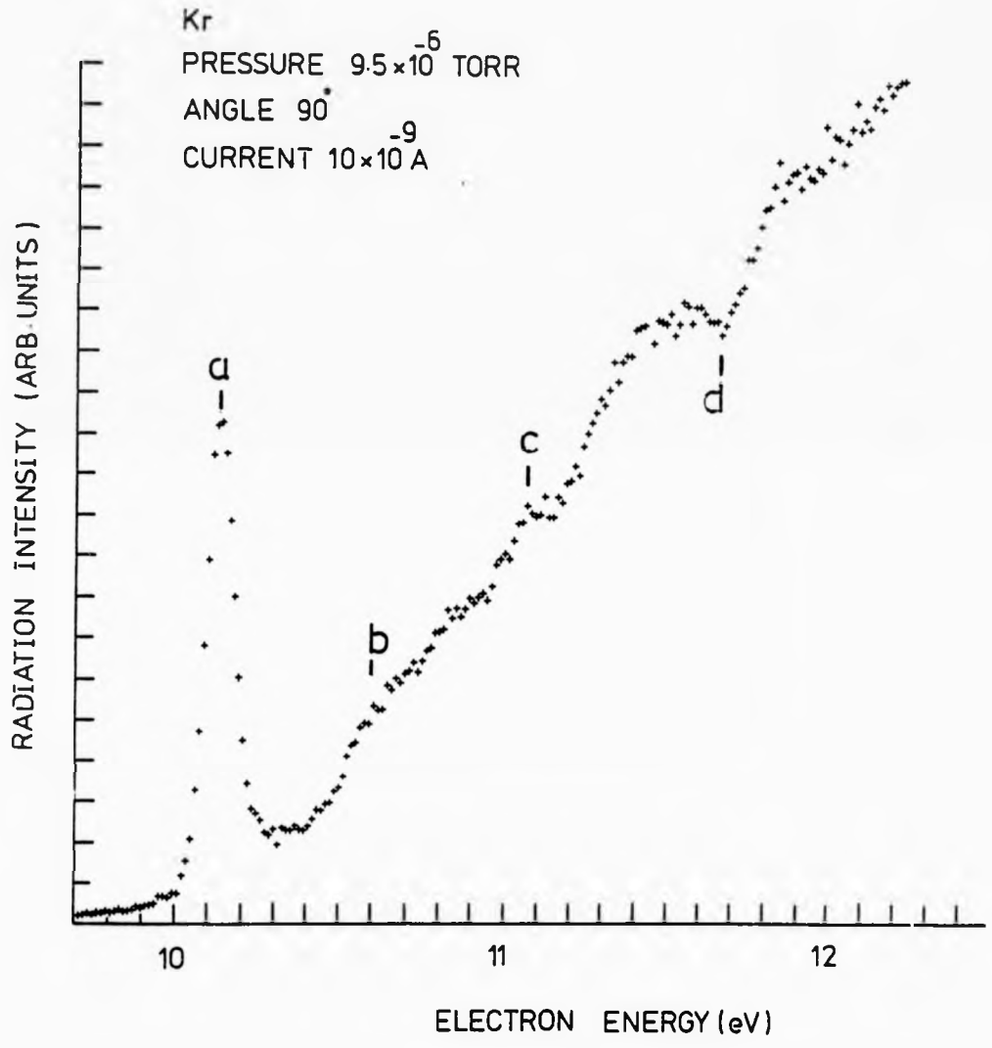

Fig. (3.9): Excitation function of the $4p^5\ 5s\ ^3P_1$ and $^1P_1$ states of Kr. The energies of the labelled features are given in Table (3.4)

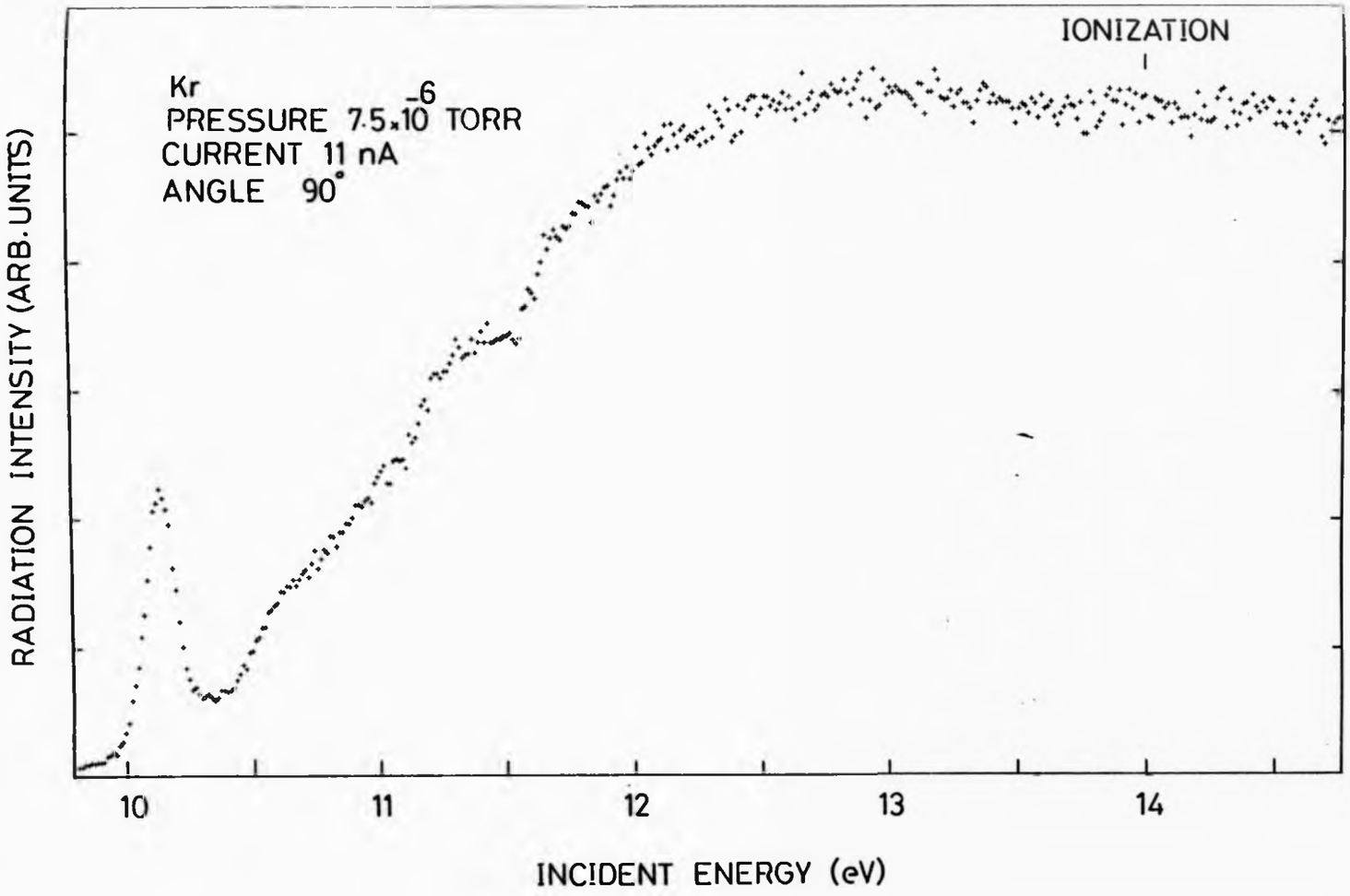

Fig. (3.10): An extension of excitation function shown in Fig. (3.9) up to the electron energy 14.75 eV

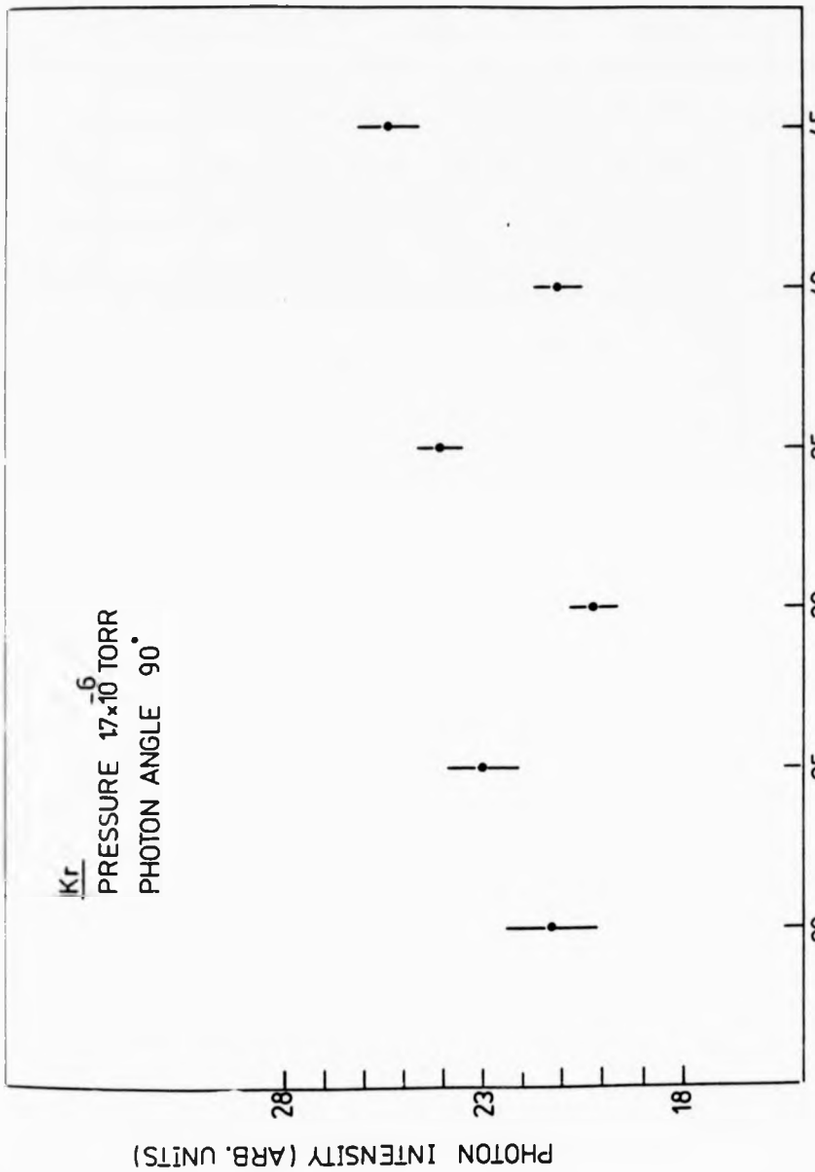

Fig. (3.1): Excitation function of Kr over the impact energy range between 20 - 45 eV

	Present work	Transmission Experiment Sanche and Schulz (1972)	UV Excitation Function Brunt et al (1977a)	Metastable Production Pichanic and Simpson (1968)
a	10.14	10.16 - 10.19	10.128	10.05
b	10.60	10.66 - 10.69	10.671	10.63
c	11.06			11.10
d	11.65	11.67		11.70

Table (3.4): Measured energies (eV) of the features in the excitation function for Kr Fig. (3.9). These values are estimated to be accurate to ±0.02 eV.

These states decay to the $5p^6\ {}^1S_o$ ground state by emission of 1469.60 Å and 1295.58 Å radiation respectively. The energy scale is calibrated by normalizing the onset of excitation to the xenon excitation threshold at 8.44 eV. The energy width of each channel is 10 meV. The energy positions of these resonances, shown in the upper part of Fig. (3.12), are compared with other experiments and summarized in Table (3.5). From the above figure, the strongest feature in the excitation function is the broad peak at about 9.20 eV. This broad feature was seen previously in UV excitation measurements by Swanson et al (1973 b), Elston et al (1973) and recently by Brunt et al (1977 a).

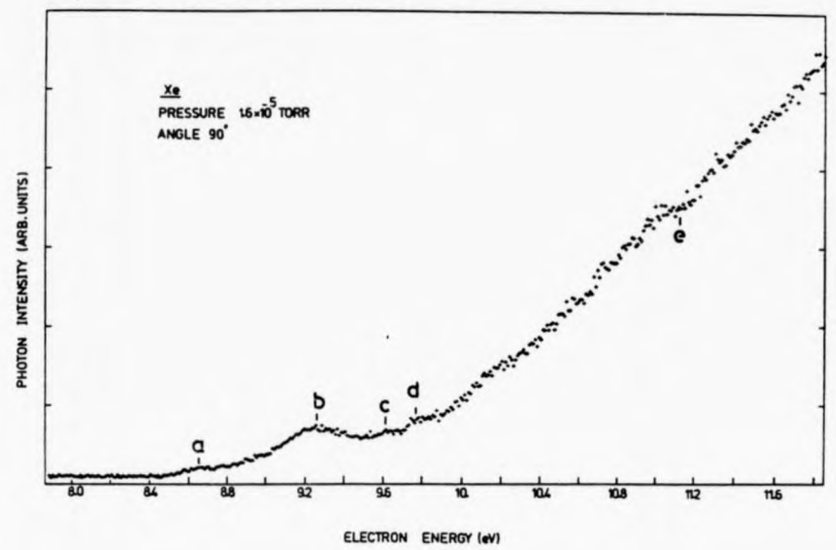

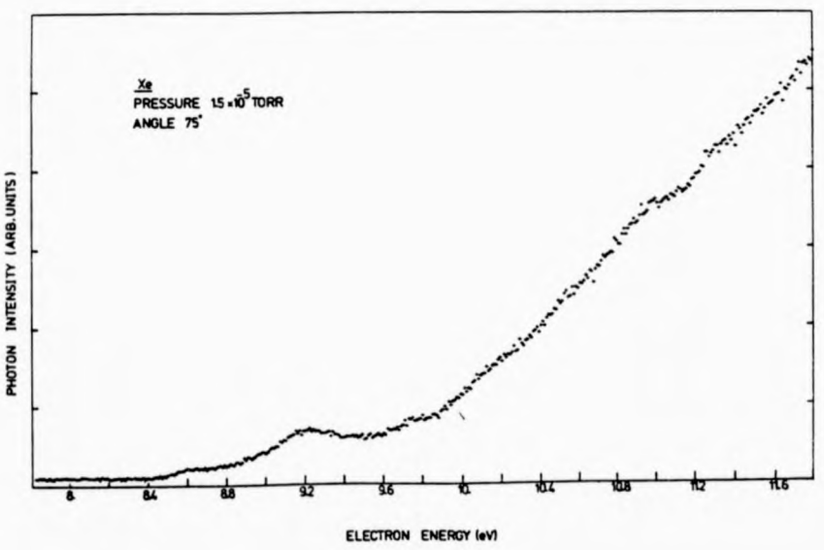

Fig. (3.12): Excitation function of the $5p^5\ 6s\ {}^3P_1$ and ${}^1P_1$ states of Xe. The energies of the labelled features are given in Table (3.5)

	Present work	Metastable production Pichanic and Simpson (1968)	Transmission expt. Sanche and Schulz (1972)	UV excitation function Elston et al. (1973)	UV excitation function Brunt et al (1977a)
a	8.65		8.48	8.54	8.48
b	9.26	9.0	9.11 - 9.26	9.20	9.14
c	9.61	9.5	9.65		9.612
d	9.77			9.70	
e	11.12		11.0	11.0	

Table (3.5): Measured energies (eV) of the features in the excitation function for Xe. Fig. (3.12). These values are estimated to be accurate to ±0.02 eV.

CHAPTER 4

NEAR THRESHOLD POLARIZATION OF ATOMIC LINE RADIATION EXCITED BY ELECTRON IMPACT

4.1 Introduction

When an atom is excited from the ground state to an excited state by electron impact, the radiation emitted by the atom in an electric dipole transition will, in general, be polarized and show an anisotropic angular distribution. The polarization is defined by

$$P = \frac{I_{\parallel} - I_{\perp}}{I_{\parallel} + I_{\perp}} \tag{4.1}$$

where $I_{\parallel}$ and $I_{\perp}$ are the intensities of light observed at right angle to the electron beam with electric vectors oriented parallel and perpendicular to the electron beam. In general, the polarization of line radiation excited by electron impact depends significantly on the electron impact energy, on the excited state configuration, on the natural line width, on the fine and hyperfine structures, and on the atomic beam density.

The first polarization measurements were made in electron-atom collisions, for example, by Elett et al (1926), Skinner (1926), Eldridge and Olsen (1926) and Quadar (1927). Skinner and Appleyard measured the polarization of 28 lines in mercury. They also reported the polarization as a function of electron energy. These results showed the polarization tended towards zero as the electron energy approached the threshold value and then followed by a sharp increase to a maximum and then a gradual decrease as the electron energy was increased.

The theory of polarization was first developed by Oppenheimer (1927a,b) and (1928) and by Penney (1932). They showed that there was disagreement

between the experimental results of Skinner and Appleyard (1927) and what was expected theoretically for the polarization close to threshold. This theory was then developed further by Percival and Seaton (1958) within the framework of quantum mechanics.

Since then, the polarization of line radiation has attracted special interest, particularly close to threshold. McFarland (1964), (1967), Fedorov and Mezentev (1965), Heddle and Keesing (1967), Whitteker and Dalby (1968) and Heideman et al (1969) have reported a rapid change of the polarization close to threshold for a number of lines where the theoretical polarization was actually large. Heddle et al (1974) measured the polarization of the ($4^1D - 2^1P$) line of helium. They explained the rapid fall in the polarization near threshold as due to the existence of the $1s4d^2\ ^2S$ resonance just below threshold. The polarization measurements have also been extended to a number of gas atoms, for example by Ottley and Kleinpoppen (1975) who measured the optical excitation function of the ($6^3P_1 - 6^1S_0$) line of mercury at 2537 Å close to threshold.

There are two prominent resonances which have a major effect on polarization. Hafner et al (1965) studied the polarization of the first resonance line of Li^6, Li^7 and Na^{23} isotope compositions. The data showed that the polarization increases monotonically from high energy to threshold value. These results showed that polarization is sensitive to the natural width and to the fine and hyperfine separation of the excited states.

Recently, Zaidi et al (1978) showed the effects of hyperfine structure on the polarization of ($6^3P_1 - 6^1S_0$) line of mercury. In (1972) Enemark and Gallagher measured the polarization of sodium D lines from lower electron energy to 100 eV. The results showed good agreement

with the theoretical value. Ehlers and Gallagher (1973) measured the polarization of the ($^1P_1$ - $^1S_0$) line of Ca. The results showed that threshold polarization is 100% which is in excellent agreement with the theoretical value.

Most previous polarization studies have been concerned with transitions in the visible region of the spectrum. Polarization measurements for UV transitions are exceedingly rare in literature and limited to the (1s - 2p) Lyman-α transition in atomic hydrogen, for example, Ott et al (1970).

Recently, Dassen et al (1977) reported on the polarization of the 104.8 and 106.7 nm resonance lines of Ar over a wide range of incident electron energy (in their experiment, the radiation emerging from the interaction region passed a triple polarizer before entering an electron detector).

Present work is concerned with the measurements of the polarization of UV photons emitted from the first excited state of Kr and Xe with configurations $4p^5 5s\ ^3P_1$ and $^1P_1$ and $5p^5 6s\ ^3P_1$ and $^1P_1$ respectively. These results are deduced from the theoretical relation between the angular intensity distribution $I(\theta)$ and the polarization (p) (Al-Shamma and Kleinpoppen (1977, 1978)). This method was first suggested by Smit (1935) who measured the polarization fractions of visible radiation from helium. In (1963) McFarland and Soltysik measured the polarization of the (4^1D - 2^1P) line of He using this method. Mumma et al (1974) reported on the first experimental data of the angular intensity distribution and polarization of the (n^1P - 1^1S) resonance line of He where the emitted photons are in the extreme UV range.

Comprehensive reviews on polarization are given by Kleinpoppen (1969, 1975, 1977), Fano and Macek (1973) and by Heddle (1976).

with the theoretical value. Ehlers and Gallagher (1973) measured the polarization of the ($^1P_1$ - ^1S_o) line of Ca. The results showed that threshold polarization is 100% which is in excellent agreement with the theoretical value.

Most previous polarization studies have been concerned with transitions in the visible region of the spectrum. Polarization measurements for UV transitions are exceedingly rare in literature and limited to the (1s - 2p) Lyman-α transition in atomic hydrogen, for example, Ott et al (1970).

Recently, Dassen et al (1977) reported on the polarization of the 104.8 and 106.7 nm resonance lines of Ar over a wide range of incident electron energy (in their experiment, the radiation emerging from the interaction region passed a triple polarizer before entering an electron detector).

Present work is concerned with the measurements of the polarization of UV photons emitted from the first excited state of Kr and Xe with configurations $4p^5 5s\ ^3P_1$ and $^1P_1$ and $5p^5 6s\ ^3P_1$ and $^1P_1$ respectively. These results are deduced from the theoretical relation between the angular intensity distribution $I(\Theta)$ and the polarization (p) (Al-Shamma and Kleinpoppen (1977, 1978)). This method was first suggested by Smit (1935) who measured the polarization fractions of visible radiation from helium. In (1963) McFarland and Soltysik measured the polarization of the (4^1D - 2^1P) line of He using this method. Mumma et al (1974) reported on the first experimental data of the angular intensity distribution and polarization of the (n^1P - 1^1S) resonance line of He where the emitted photons are in the extreme UV range.

Comprehensive reviews on polarization are given by Kleinpoppen (1969, 1975, 1977), Fano and Macek (1973) and by Heddle (1976).

4.2 Theory of the angular intensity distribution of emitted photons

Assume that a gas atom initially in the ground state at point O is excited by a beam of electrons moving in the z-direction as shown in Fig. (4.1). Photons emitted during the decay process are often polarized and therefore show an anisotropic intensity distribution. The intensity pattern can be described in a classical way by using harmonic oscillators (Smit (1935)). We assume the components of this oscillator along the z-axis are (a) and the corresponding components perpendicular to the electron beam are b and c as shown in Fig. (4.1).

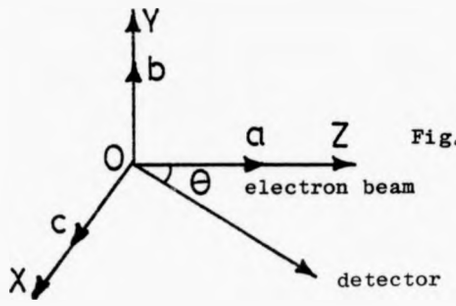

Fig.(4.1)

For a single dipole, the intensity of the dipole radiation in a direction making an angle Θ with the dipole axis is given by

$$I(\Theta) = I_o \sin^2\Theta \qquad (4.2)$$

where I_o is the total intensity perpendicular to the dipole axis. Let us define $I_{||}$ and $I_{\perp}$ as the intensities observed at right angle to the direction of the electron beam with electric vectors parallel and perpendicular to the electron beam.

$$I_{\perp} = K^2 b^2 \qquad (4.3)$$

$$I_{||}(\Theta) = (Ka \sin\Theta)^2 + (Kc \cos\Theta)^2 \qquad (4.4)$$

$$= (Ka \sin\Theta)^2 + (Kb \cos\Theta)^2 \quad \text{For axial symmetry } b = c$$

where K is a constant.

The total intensity $I(\Theta)$ observed at an angle Θ is given by

$$I(\Theta) = I_{\perp} + I_{\parallel}(\Theta)$$
$$= K^2(a^2 + b^2) + K^2(b^2 - a^2)\cos^2\Theta \qquad (4.5)$$

For $\Theta = 90^{\circ}$

$$I(90) = K^2(a^2 + b^2) \quad . \qquad (4.6)$$

Combining Eqs. (4.5) and (4.6) we obtain:

$$\frac{I(\Theta)}{I(90)} = 1 - \frac{a^2 - b^2}{a^2 + b^2}\cos^2\Theta$$

The polarization $p = \dfrac{a^2 - b^2}{a^2 + b^2}$,

therefore, $I(\Theta) = I(90)\{1 - p\cos^2\Theta\}$ (4.7)

This equation shows that a measurement of the ratio of $I(\Theta)$ to $I(90)$ for any angle Θ permits the polarization p to be deduced.

4.3 Results

The polarization of the first excited states of Kr and Xe with the configurations ($4p^5 5s\ ^3P_1$ and $^1P_1$) and ($5p^5 6s\ ^3P_1$ and $^1P_1$) respectively is obtained by measuring the angular intensity distribution of photons with respect to the electron beam axis.

The apparatus was first checked by measuring the angular intensity distribution of the O1($^3S - {}^3P$) resonance multiplet at 1304 Å. Theoretically, the photons of this transition are expected to show an isotropic distribution because they originate from an L=0 term ($^3S^{\circ}$) (Lawrence (1970)). A photon detector equipped with a MgF_2 window is used in this experiment. The only strong emission line which can be excited in the wavelength range of the MgF_2 window by electron impact on O_2 is the O1(1304 Å) (Mumma and Zipf (1971)). This transition is excited by dissociative excitation of O_2 by electron impact. The

excitation process can be described by

$$e + O_2 \rightarrow O(3s^1\ {}^3S^o) + O(2p^4\ {}^3P) + e$$

$$O({}^3S^o) \rightarrow O({}^3P) + h\nu(9.54\ eV)$$

$$K.E_{min} = D_o^o(O\text{-}O) + E\ photons$$

$$= 5.11 + 9.54 = 14.65\ eV$$

Fig. (4.2) shows the experimental results of the photon yield resulting from dissociative excitation as a function of electron energy. This graph indicates a maximum at about 110 eV which is in good agreement with the absolute cross section measurements of Lawrence (1970) as shown in the above figure. The dependence of the photon intensity is also studied as a function of gas pressure as shown in Fig. (4.3).

The angular intensity distribution of photons is measured in the angular range of 67 - 112.5° as shown in Fig. (4.4). The impact electron energy is 100 eV. An isotropic distribution is obtained within the experimental errors.

Next, the angular intensity distribution of photons of the above states of Kr is measured at angles (67.5, 75, 82.5, 90, 97.5, 105 and 112.5°). The data $I(\Theta)$ are plotted against Θ (where Θ is the direction of observation with reference to the electron beam). A number of typical angular intensity distributions at various electron energies are shown in Figs. (4.5) and (4.6). From these measurements, the fitted data $I(\Theta)$ appear to be symmetrical around 90° and the minimum intensity $I(\Theta)$ occurs at this angle. The data $I(\Theta)$ are analysed by plotting $I(\Theta)$ against $\cos^2\Theta$ and then the polarization is obtained from the relation (4.7) by using a least square fitting procedure as shown in Fig. (4.7). A check is made to estimate the shift in angle of the minimum intensity from the expected 90° for negative polarization (Fig. (4.8)) by using the relation

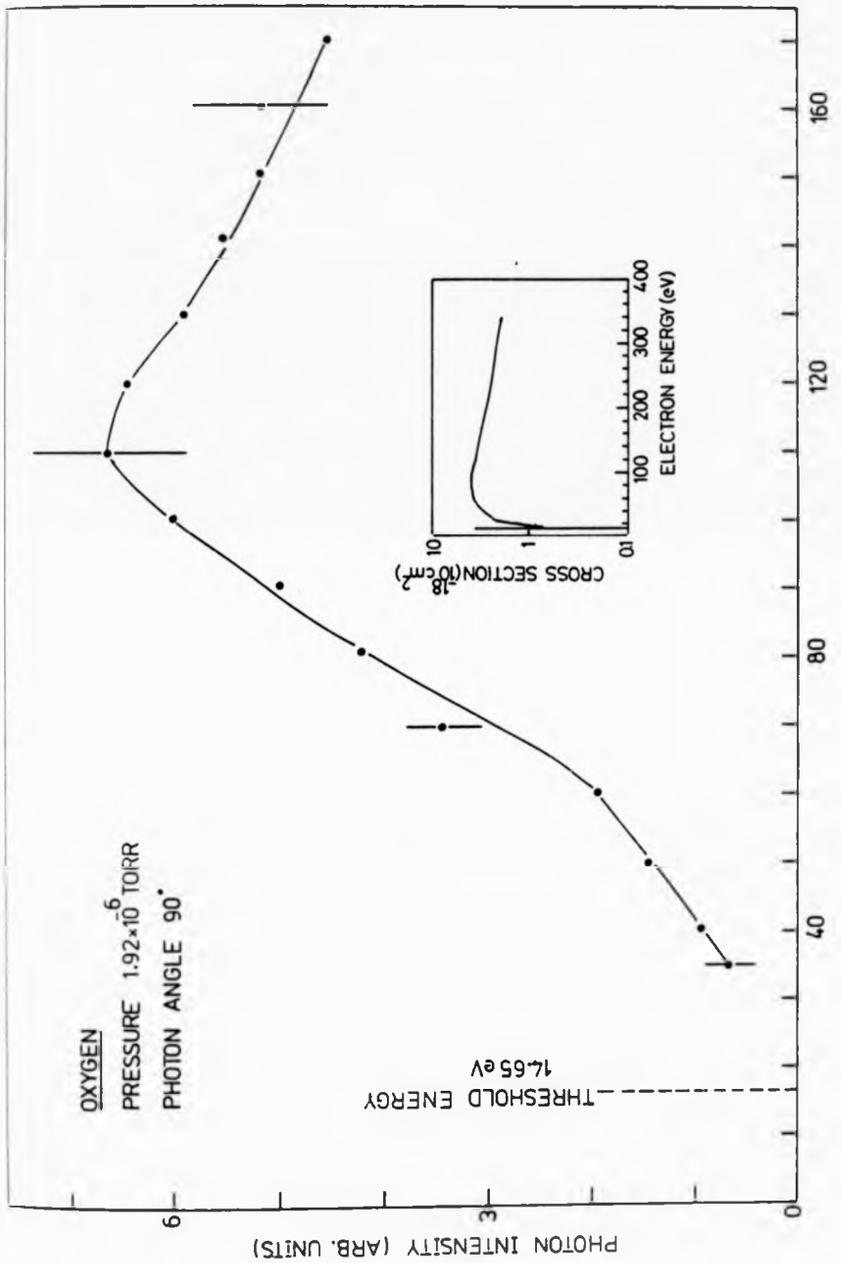

Fig. (4.2): The excitation function of O1(1304 Å) multiplet resulting from the dissociative excitation of O_2 by electron impact (1 rms error). The inset shows the absolute cross section of O1(1304 Å) (Lawrence (1970)).

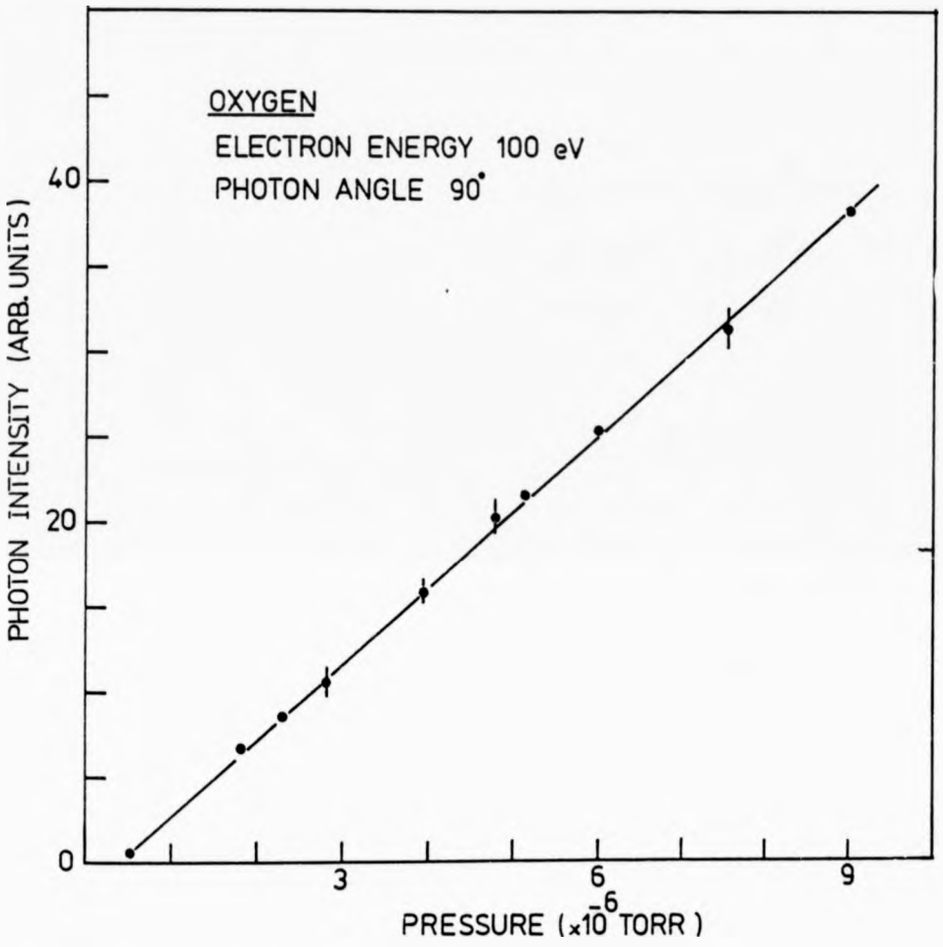

Fig. (4.3): Dependence of the photon intensity of O1(1304 Å) multiplet on the gas pressure (1 rms error)

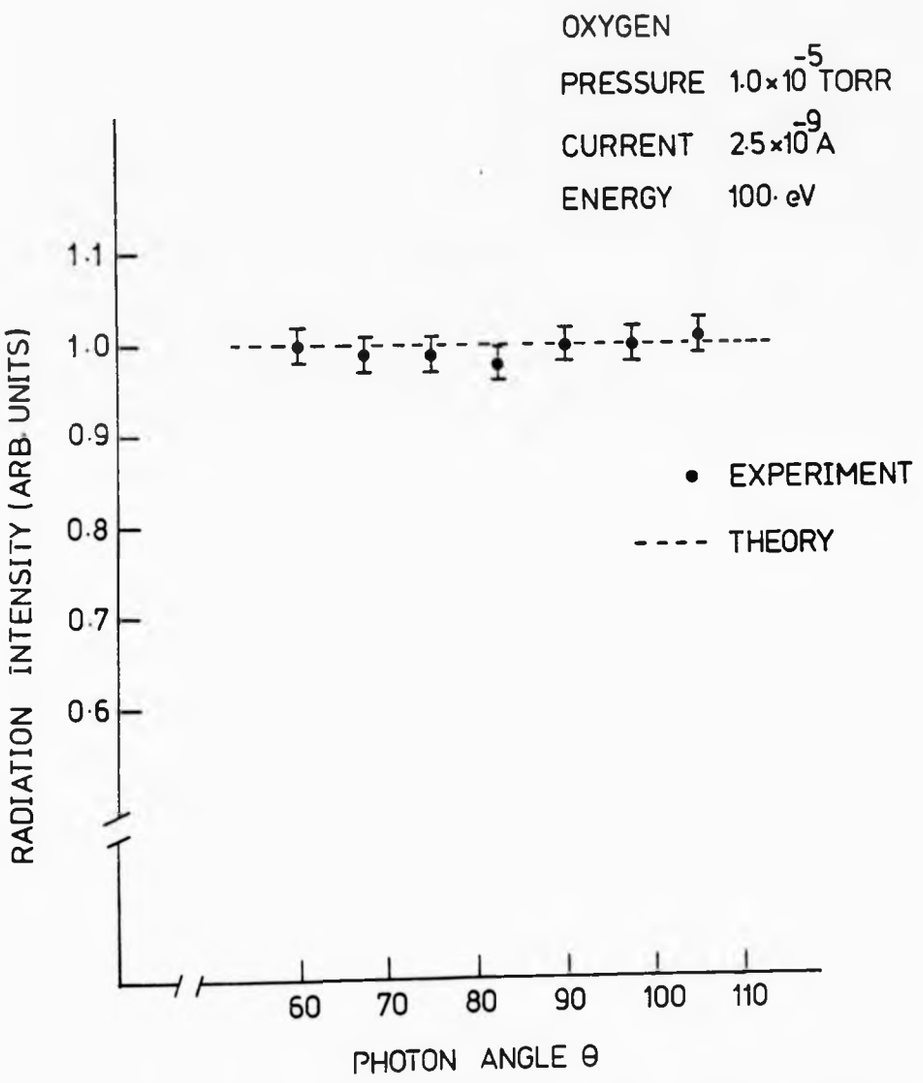

Fig. (4.4): Angular intensity distribution of O1(1304 Å) multiplet (1 rms error)

Fig. (4.5): Angular intensity distributions of photons emitted from $4p^5\ 5s\ {}^3P_1$ and ${}^1P_1$ states of Kr. The crosses represent the experimental data while the closed circles represent the fitted data using a least square fitting procedure of Eq. (4.7) (1 rms error).

Fig. (4.5): Angular intensity distributions of photons emitted from $4p^5\ 5s\ ^3P_1$ and $^1P_1$ states of Kr. The crosses represent the experimental data while the closed circles represent the fitted data using a least square fitting procedure of Eq. (4.7) (1 rms error).

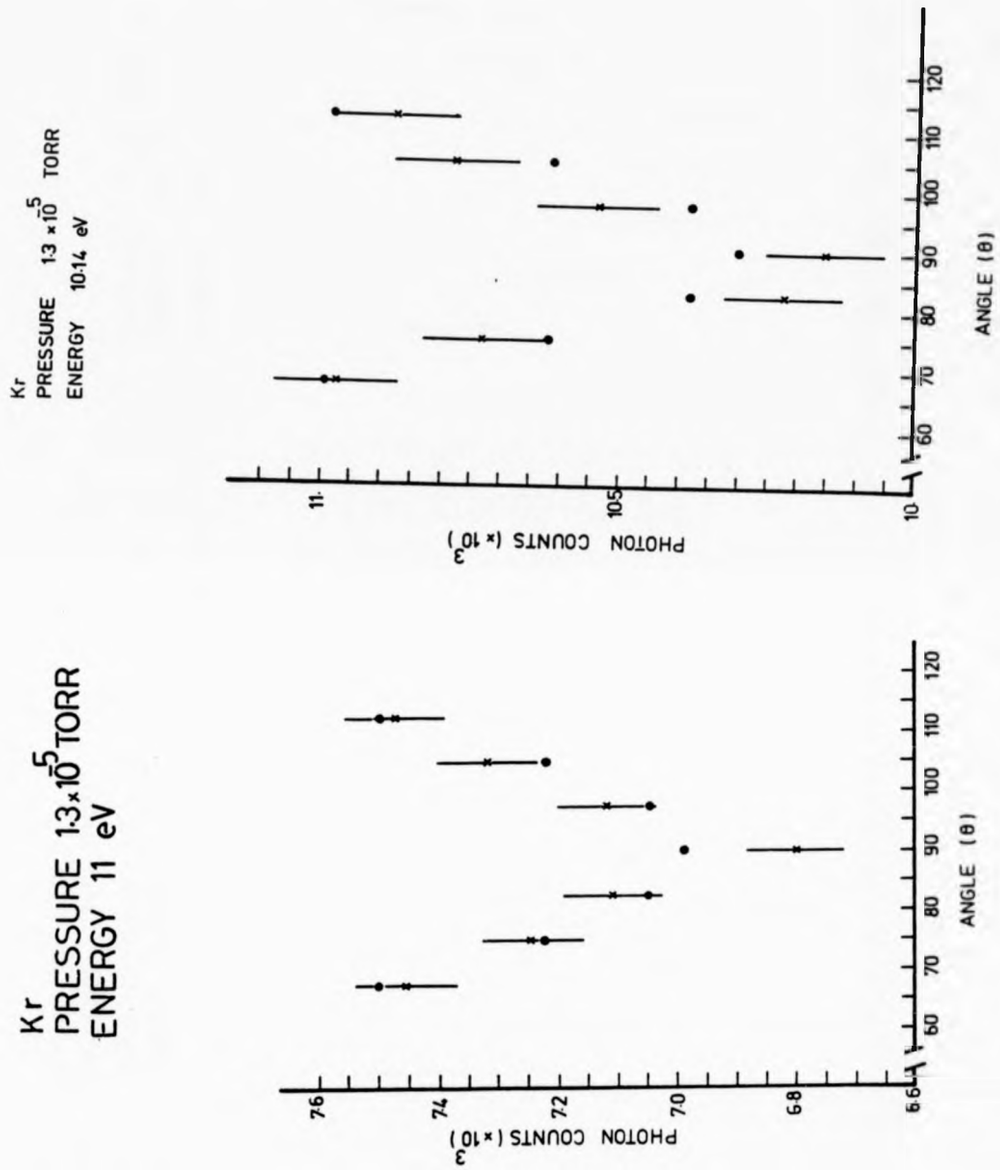
Kr
PRESSURE 1·3 ×10⁻⁵ TORR
ENERGY 10·14 eV
PHOTON COUNTS (×10³)
ANGLE (θ)
Kr
PRESSURE 1·3×10⁻⁵ TORR
ENERGY 11 eV
PHOTON COUNTS (×10³)
ANGLE (θ)

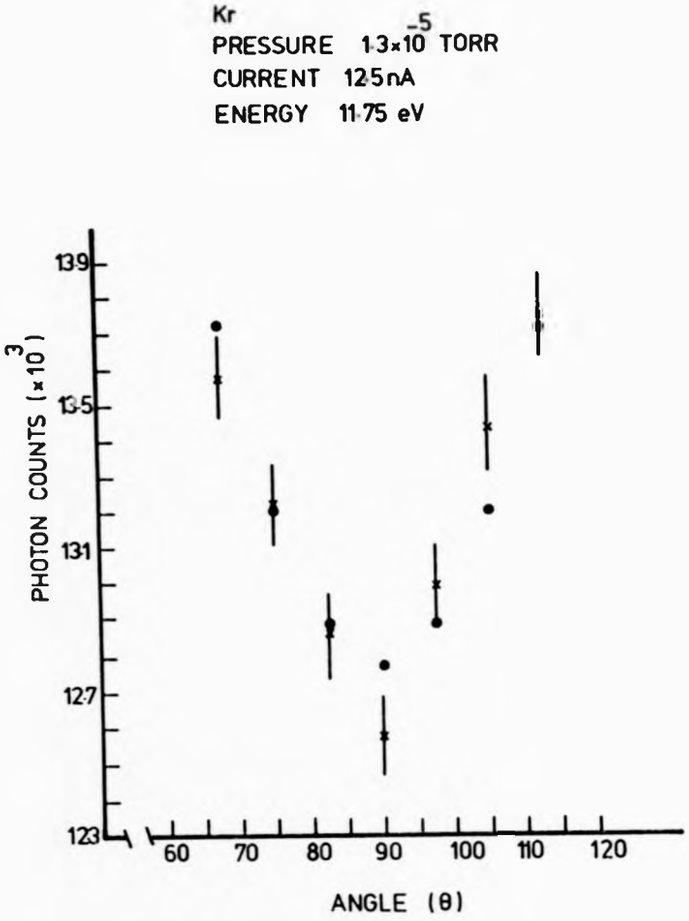

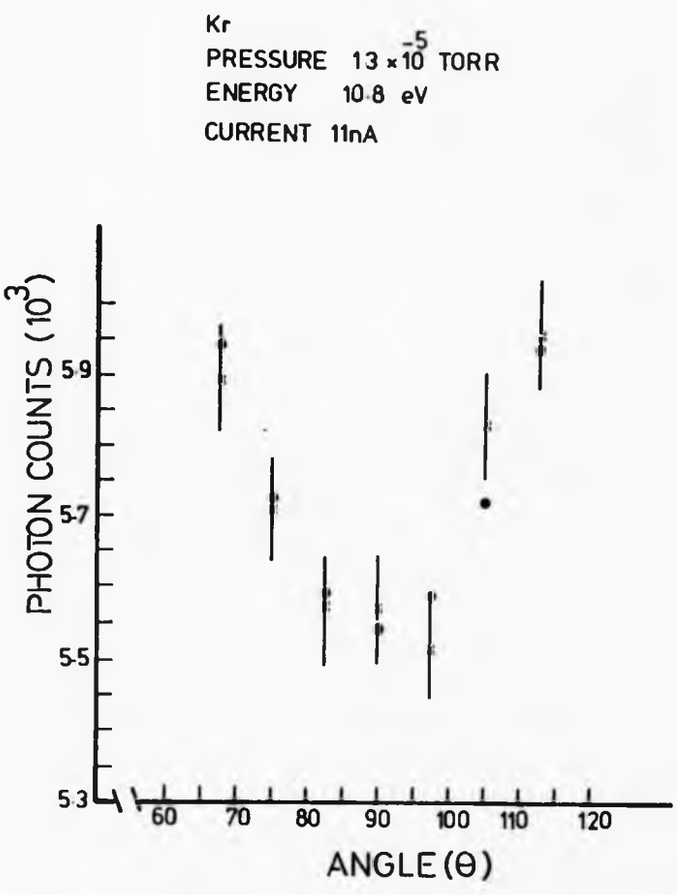

Fig. (4.6): Same caption as for Fig. (4.5)

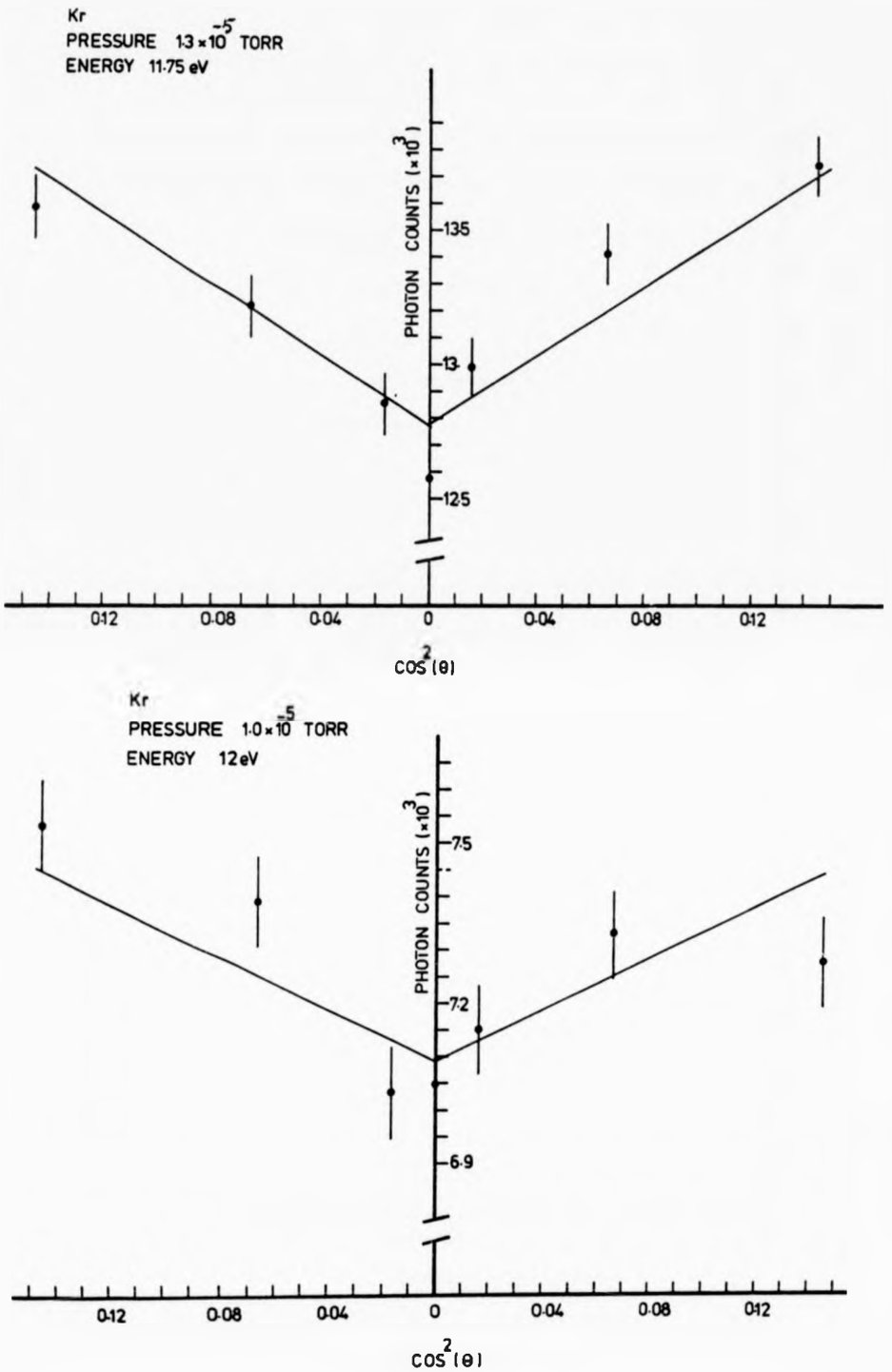

Fig. (4.7): The intensity $I(\theta)$ is plotted as a function of $\cos^2\theta$. The solid line represents the best fit of the data points by applying a least square fitting procedure of Eq. (4.7) (1 rms error)

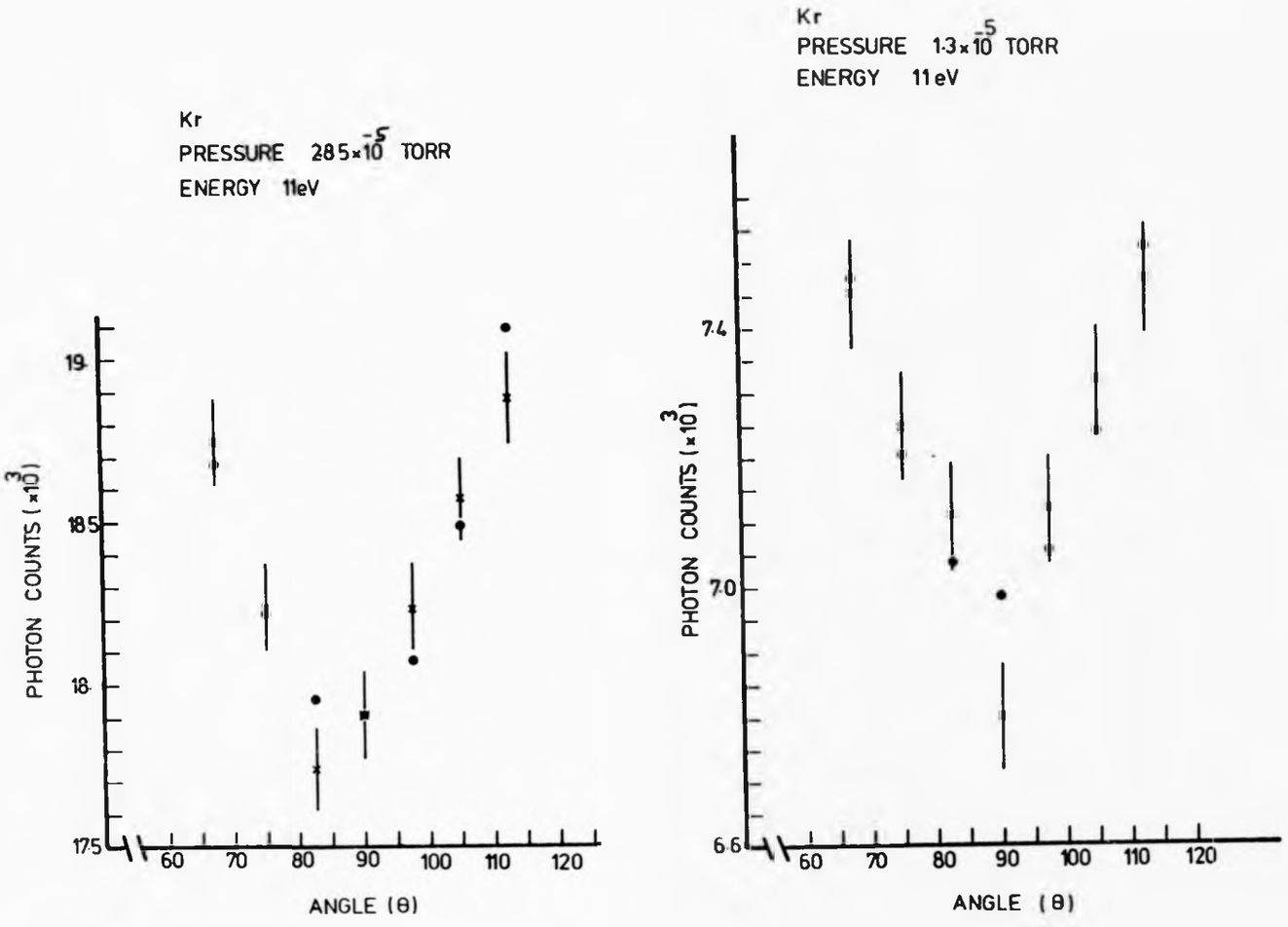

Fig. (4.8): Same as for Fig. (4.5) except the closed circles represent the fitted data using a least square fitting procedure of Eq. (4.8) (1 rms error)

$$I(\Theta) = I(90)\ \{1 - p \cos^2 (\Theta-\phi)\} \qquad (4.8)$$

where ϕ is a small shift in angle.

The maximum shift which appeared from these measurements is $\sim 4^{o}$. The polarization of photons as a function of gas pressure is shown in Fig. (4.9). These measurements have been carried out in the gas pressure range $1 - 7.5 * 10^{-5}$ torr. The polarization appears to be constant in this range of gas pressure.

The upper part of Fig. (4.10) shows the excitation function of the above states of Kr while the lower part gives the polarization of these transitions as a function of the electron energy. Results show that the polarization has a negative value in that range of electron energy.

The data shown in Figs. (4.9) and (4.10) are the average values of three angular intensity distributions obtained under the same experimental conditions. One of the problems associated with the measurements is that the intensity observed from a large volume of gas depends on the observation angle and, therefore, the intensity in this case must be corrected by multiplying it by $\sin\Theta$. We found, however, that such a correction is negligible because the interaction region arising from the intersection of electron and atomic beams is small. The polarization results for Xe are shown in Figs. (4.11), (4.12), (4.13), (4.14) and (4.15). Again the polarization is negative in the electron energy range studied. To our knowledge, no theoretical predictions for the polarization of the above transitions in Kr and Xe exist.

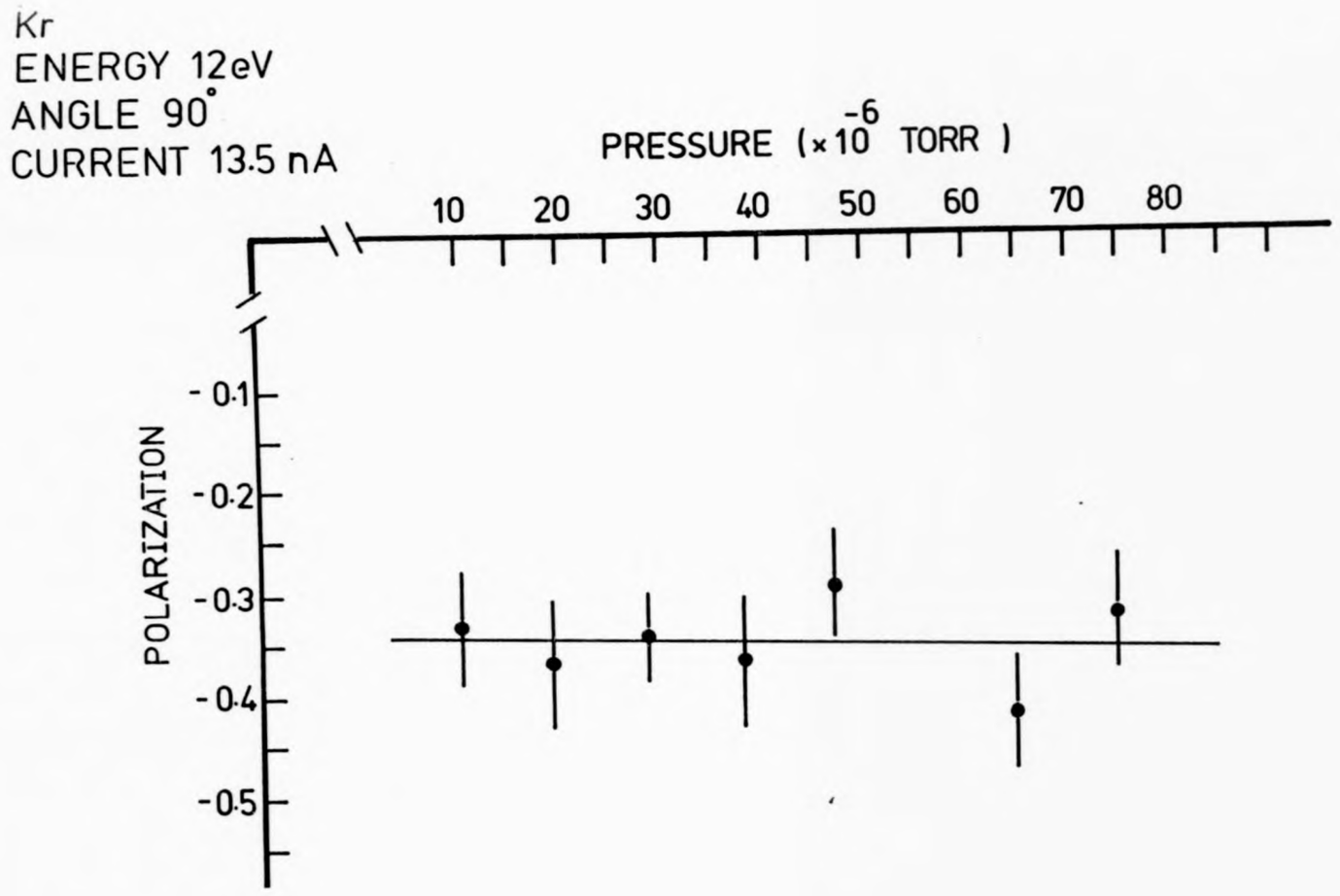

Fig. (4.9): Dependence of the polarization on the gas pressure. The solid line represents the best fit of data points using a least square fitting procedure (1 rms error)

Fig. (4.10): The upper part shows the combined excitation function of $4p^5\ 5s\ {}^3P_1$ and ${}^1P_1$ states of Kr.

The lower part gives the polarization of these transitions as a function of electron energy (1 rms error).

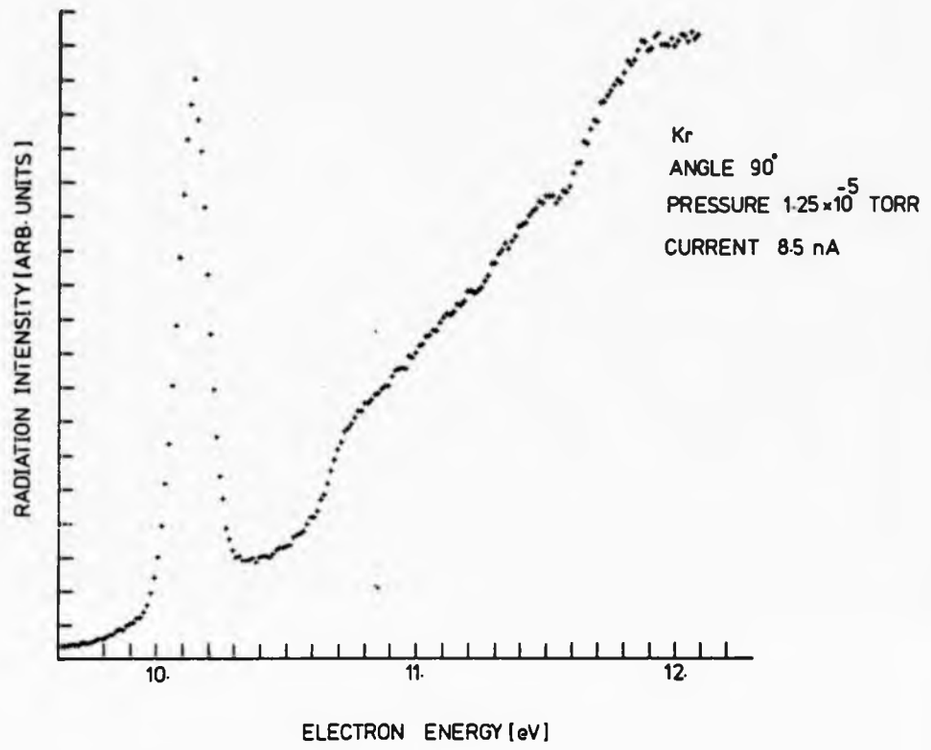
RADIATION INTENSITY [ARB. UNITS]
Kr
ANGLE 90°
PRESSURE 1·25×10⁻⁵ TORR
CURRENT 8·5 nA
10.
11.
12.
ELECTRON ENERGY [eV]

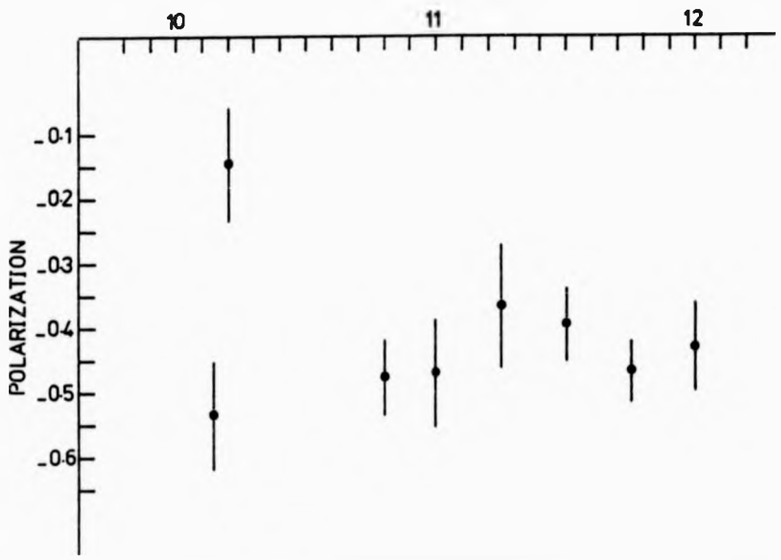
10
11
12
-0·1
-0·2
-0·3
-0·4
-0·5
-0·6
POLARIZATION

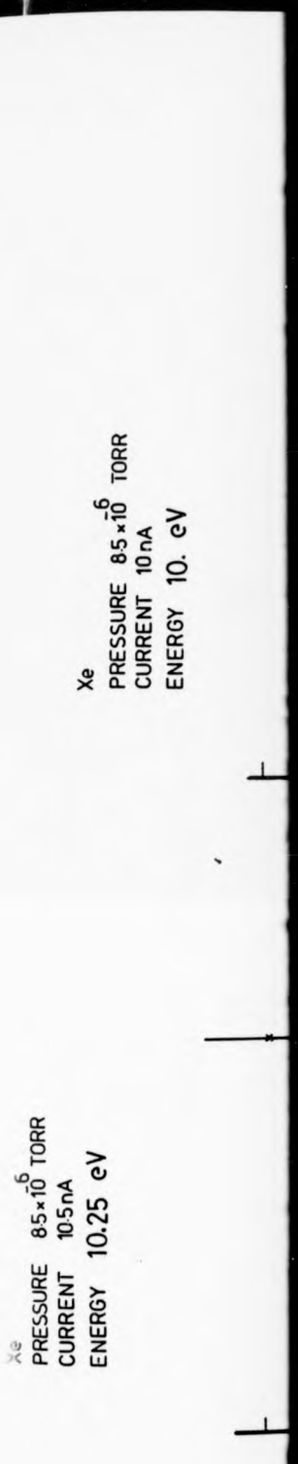

Fig. (4.11): Angular intensity distributions of photons emitted from $5p^5\ 6s\ ^3P_1$ and $^1P_1$ states of Xe. The crosses represent the experimental data while the closed circles represent the fitted data using a least square fitting procedure of Eq. (4.7) (1 rms error).

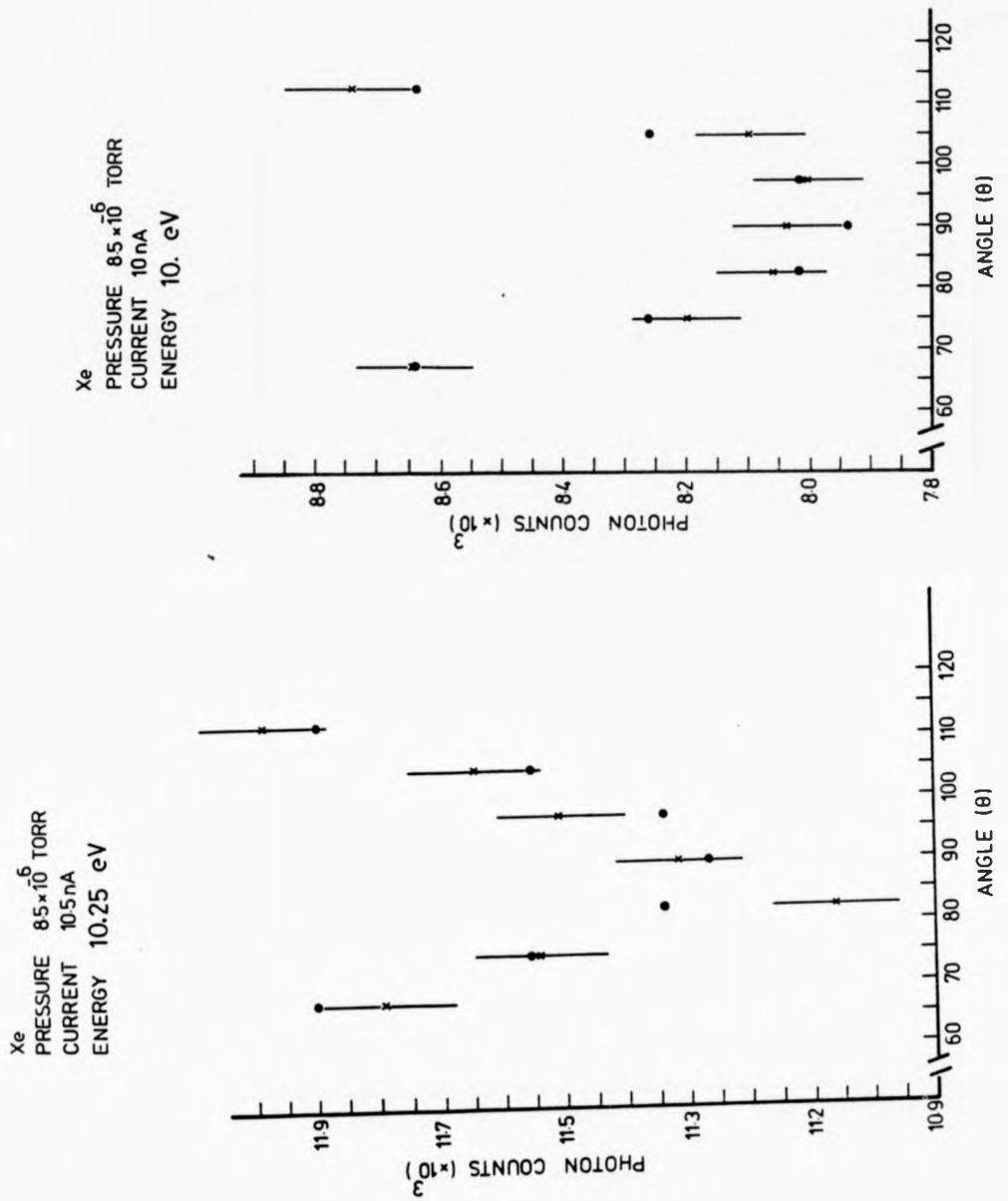

photons

he crosses

circles

itting

Xe
PRESSURE 8.5×10^{-6} TORR
CURRENT 10.5nA
ENERGY 10.5 eV

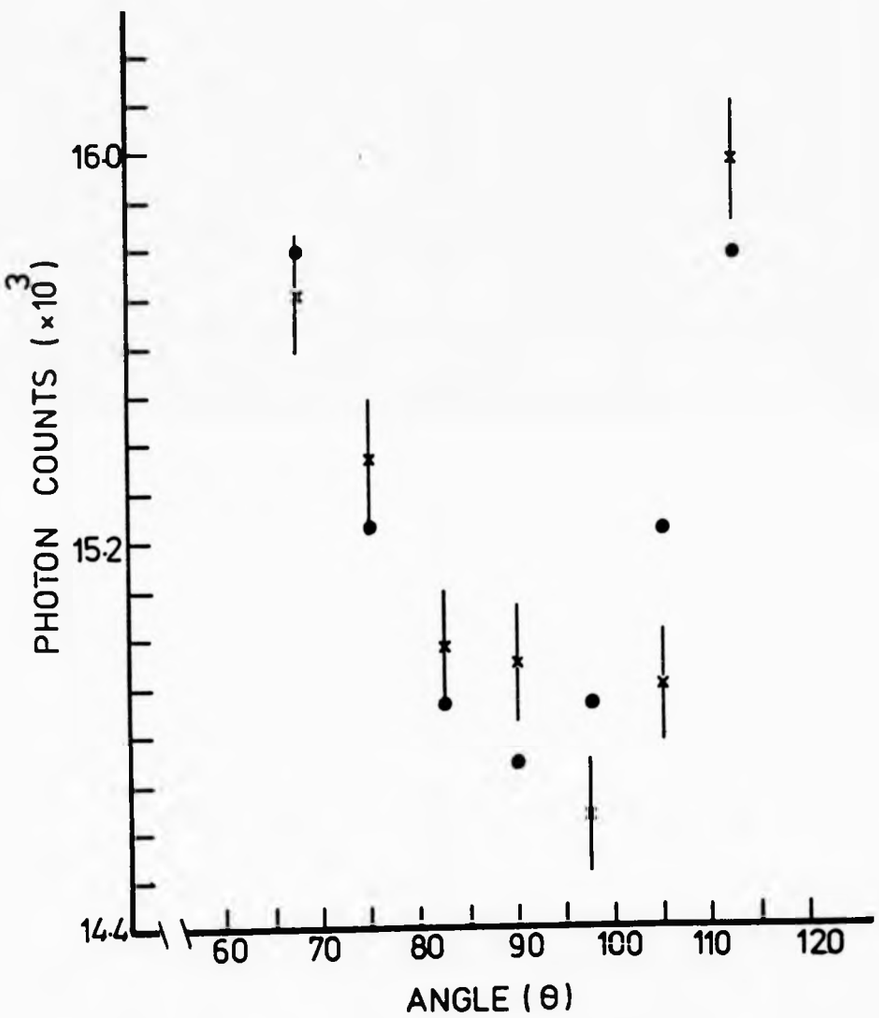

Fig. (4.12): As caption for Fig. (4.11)

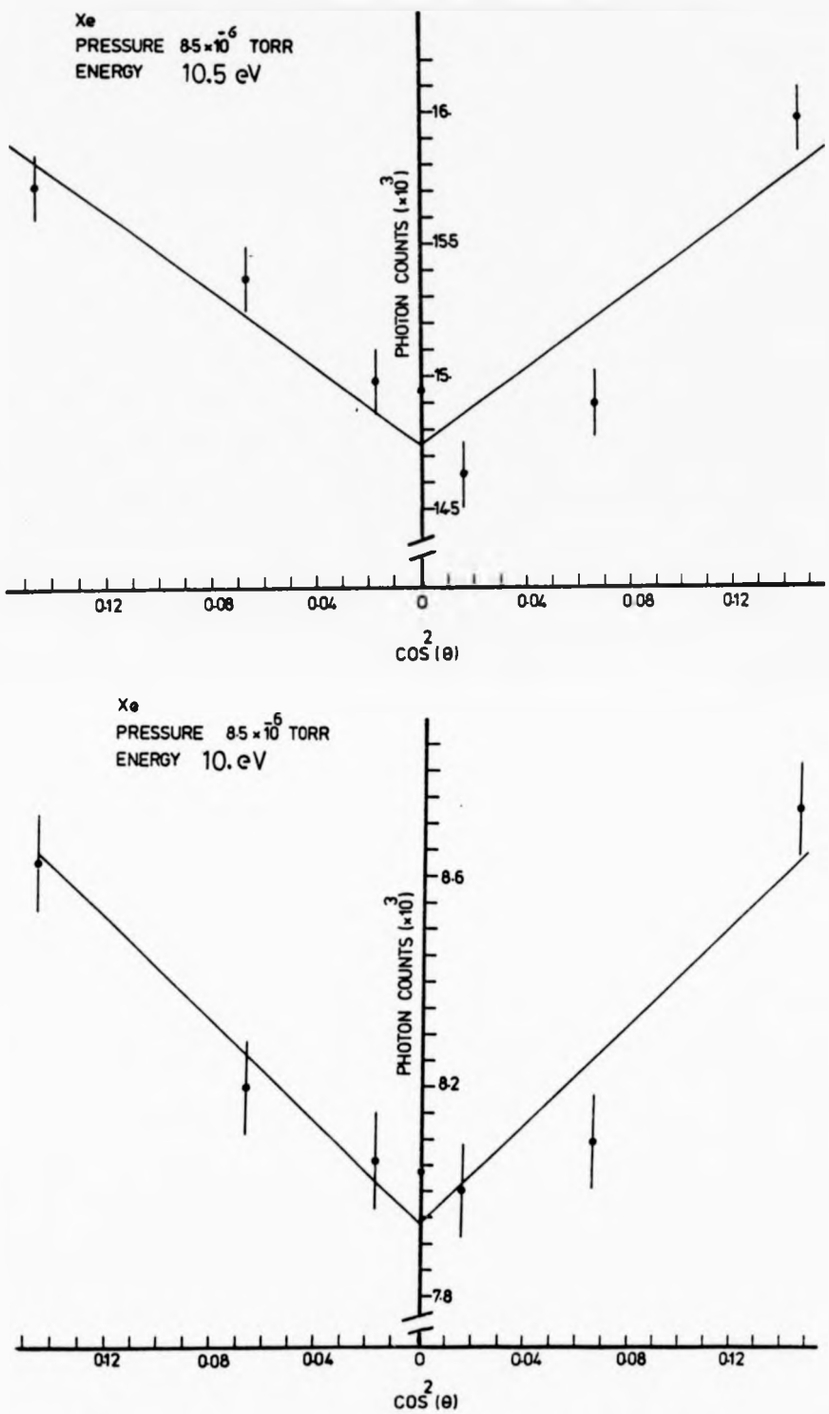

Fig. (4.13): The intensity $I(\theta)$ is plotted as a function of $\cos^2\theta$. The solid line represents the best fit of the data points using a least square fitting procedure of Eq. (4.7) (1 rms error)

Fig. (4.14): Same caption as Fig. (4.11) except the closed circles represent the best fit of data point using a least square fitting procedure of Fig. (4.8) (1 rms error).

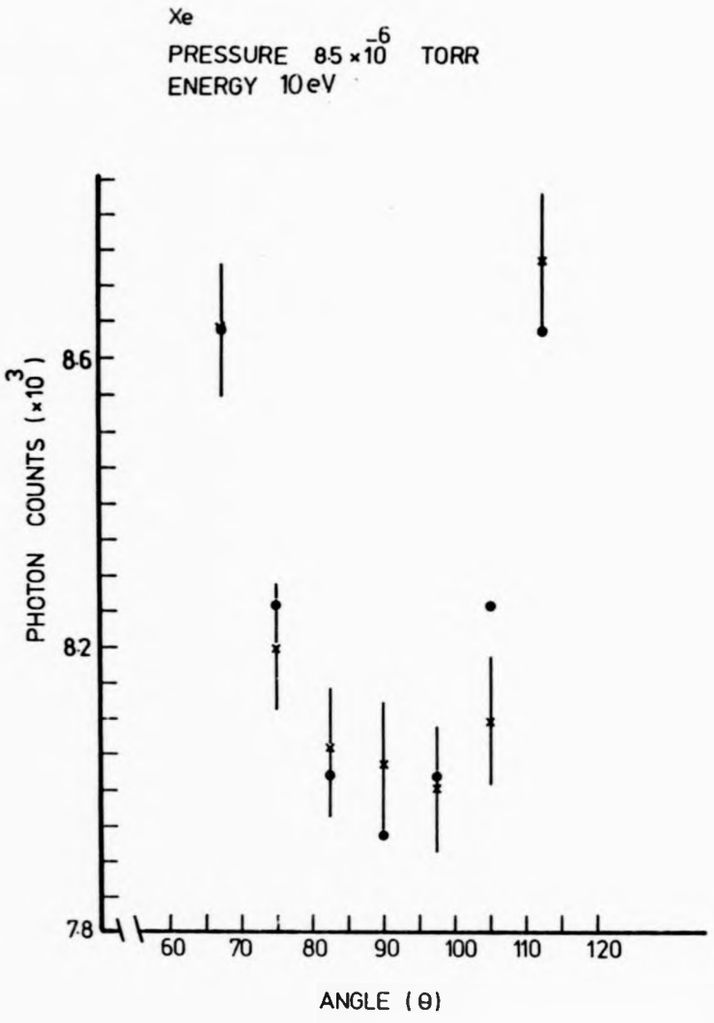
Xe
PRESSURE 8·5 × 10⁻⁶ TORR
ENERGY 10 eV
PHOTON COUNTS (×10³)
8·6
8·2
7·8
60
70
80
90
100
110
120
ANGLE (θ)

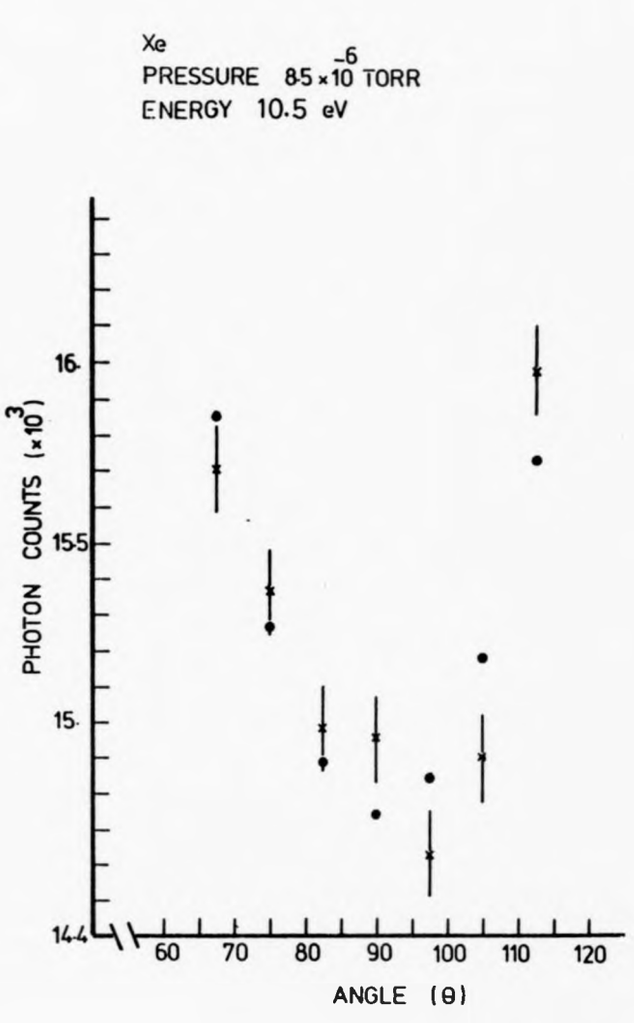
Xe
PRESSURE 8·5 × 10⁻⁶ TORR
ENERGY 10.5 eV
PHOTON COUNTS (×10³)
16·
15·5
15·
14·4
60
70
80
90
100
110
120
ANGLE (θ)

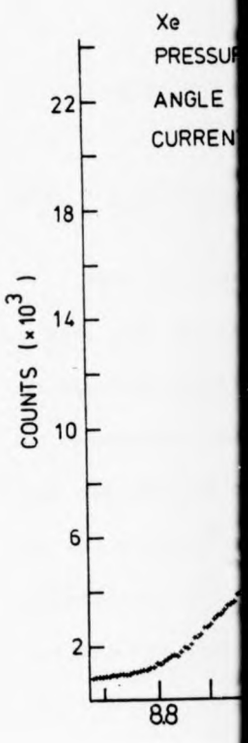

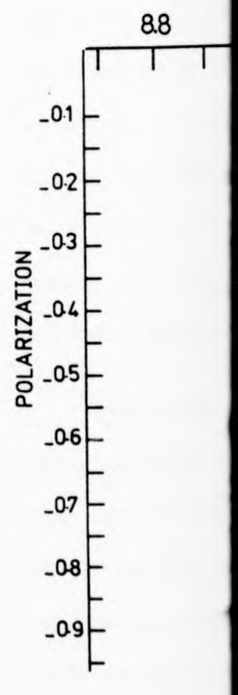

Fig. (4.15): The upper part shows the combined excitation function of $5p^5\ 6s\ {}^3P_1$ and $^1P_1$ states of Xe. The lower part gives the polarization of these transitions as a function of an electron energy (1 rms error).

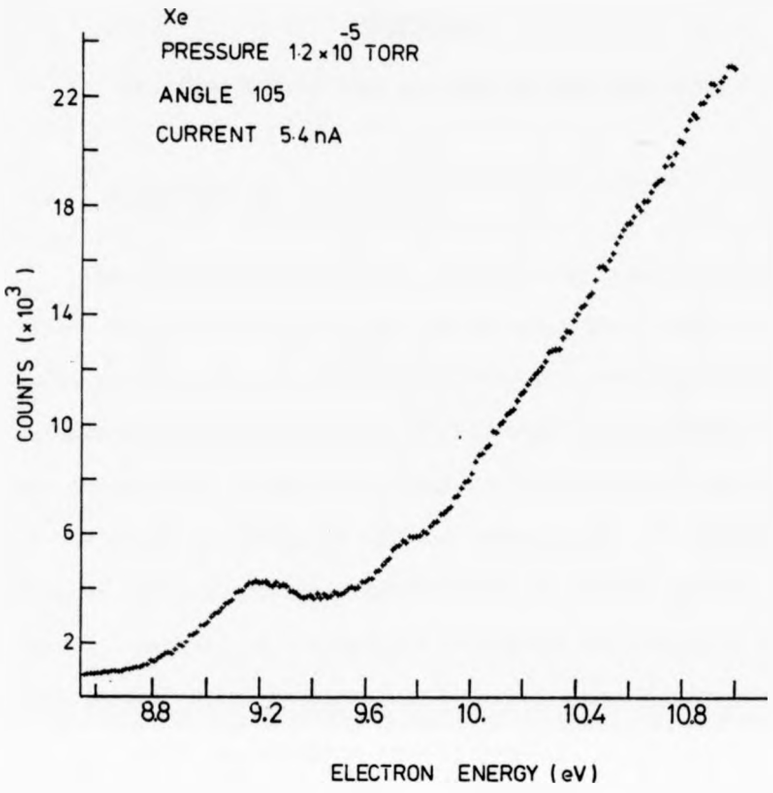
Xe
PRESSURE 1·2 × 10⁻⁵ TORR
ANGLE 105
CURRENT 5·4 nA
COUNTS (× 10³)
22
18
14
10
6
2
8.8
9.2
9.6
10.
10.4
10.8
ELECTRON ENERGY (eV)

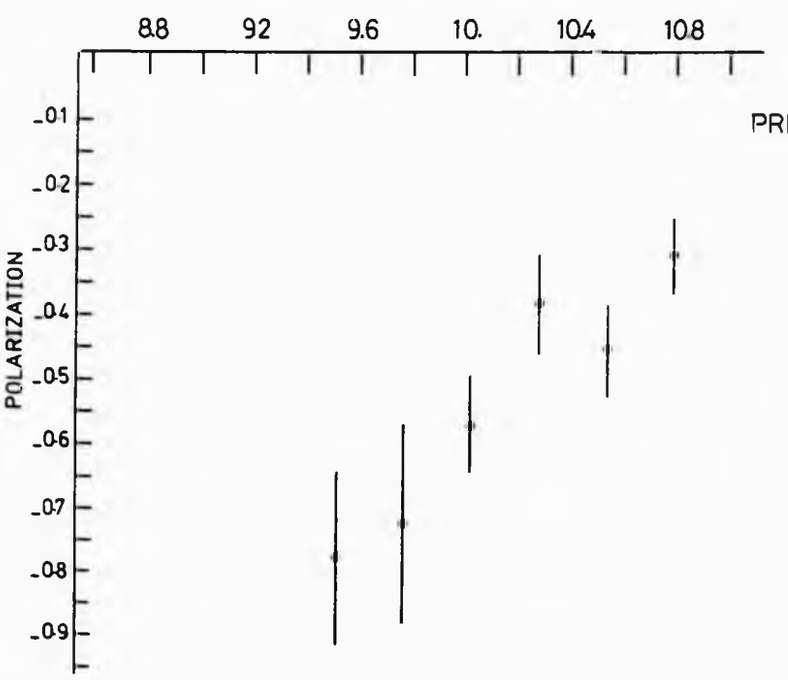
8.8
9.2
9.6
10.
10.4
10.8
PRESSURE 8·5 × 10⁻⁶ TORR
POLARIZATION
-0·1
-0·2
-0·3
-0·4
-0·5
-0·6
-0·7
-0·8
-0·9

CHAPTER 5

ELECTRON ENERGY LOSS SPECTRA OF RARE GAS ATOMS

5.1 Introduction

When an electron collides with an atom, many processes can take place, such as excitation and ionization. The probability of a particular process is characterised by its cross section. Information on excitation cross sections can be obtained by optical techniques from the observation of spectral lines. Such techniques (which are limited to the study of optically allowed transitions) are hampered by cascading effects and the technical difficulties in the UV region. The cross section can also be obtained by analysing the energy of electrons after collisions. Such processes can be carried out by using an electrostatic monochromator and analyser combination.

The electronic circuit for the detection of scattered electrons is shown in Fig. (2.3). Scattered electrons from the interaction region are analysed by a 127^{o} analyser and subsequently counted by an electron detector. We measured the energy loss spectra of Kr, Xe, Ar, and He by a method in which an electron beam of energy (E_i) excites a target atom to a state of energy (E_{ex}) and leaves the interaction region with an energy ($E_i - E_{ex}$) at a scattering angle (Θ). This electron is detected when the analyser is tuned to the energy ($E_i - E_{ex}$).

Two types of experiment have been carried out. The first one is involved with the energy loss spectra for each of the above gases over various incident electron energies at two scattering angles (27^{o} and 40^{o}). These spectra are obtained by scanning the reference voltage of the analyser. The spectra so obtained show a series of peaks corresponding to different energy levels of the target atom. The peak heights represent

the relative cross sections for exciting these states at energy (E_i) and scattering angle (Θ). The energy scale is calibrated with reference to the elastic peak (zero energy loss). The sharp features obtained and their energy positions are in good agreement with Moor's energy levels. Relative intensity (P_{loss}/P_{elast}) of the prominent peaks are measured and then plotted as a function of incident electron energy. The inelastic cross sections (σ_{loss}) of those peaks from the relative intensity is then deduced by using the following relation

$$\sigma_{loss} = \frac{P_{loss}}{P_{elast}} \times \sigma_{elast} \qquad (5.1)$$

where σ_{elast} is the elastic cross section.

In these measurements, the background intensity has been subtracted from all peaks. In addition gas pressure and electron beam current are adjusted so that the electron channeltron is not saturated.

The second experiment deals with the differential excitation functions for a number of energy states of the above gases. By tuning the analyser to the state of interest at certain incident electron energies and scattering angles (Θ), one then counts the number of electrons (counts/sec.). A similar procedure is applied by tuning the analyser to the same state at various incident electron energies. The count rates obtained are normalized with respect to the electron current (count/nA). The normalized count rates are then plotted as a function of incident electron energy. The same procedure is carried out with the residual gas. From these data we then derive the ratio of normalized gas signal/ normalized background gas signal.

Most previous studies in this field have been concentrated on electron collision with helium because helium is the simplest gas atom and easy to work with. Delage et al (1975) measured the energy loss

spectrum of Kr with high energy resolution. They observed twenty seven peaks of Krlbelow the first and second ionization potential. Swanson et al (1973a) measured the differential excitation function of the ($^3P_1$ and $^1P_1$) states of Kr over an incident electron energy range of (10 - 13 eV) at 45° scattering angle. The instrumental resolution was 50 meV. In (1973) Williams et al measured the energy loss spectra of Xe at 20 eV incident electron energy and over an angular scattering range of (5 - 135°). Swanson et al (1976) reported the energy loss spectrum of Xe at 14 eV incident electron energy and at 45° scattering angle. In (1968) Lassettre et al measured the energy loss spectra of Ar at 50 and 60 eV incident electron energies and at 0 and 15° scattering angles. Lewis et al in (1975) reported differential inelastic cross sections of 3p - 4s, s' for Ar at 30° scattering angle as a function of incident electron energy. These results are normalized to the optical model theory of Lewis et al (1974) at 200 eV and 30° scattering angle. Theoretically, Swada et al (1971) calculated the differential inelastic cross section of 3p - 4s, s' for Ar at 30° scattering angle by using a distorted wave theory. Williams and Crowe (1975) and Williams and Willis (1975) reported the absolute differential cross sections for a number of rare gas atoms. These measurements covered a wide range of incident electron energies and scattering angles.

The energy loss spectra of helium have been studied with high energy resolution by many groups (see, for example, Kupperman et al (1968) and Imhof and Read (1971a)).

5.2 Results

5.2.1 Krypton

Fig. (5.1) shows typical energy loss spectra of the background gas. These spectra have been taken at scattering angles of 27° and 40°

and at low gas pressure. The spectra show that as the analyser is tuned to higher energies, the background intensity rises gradually to a maximum and then declines and rises again. This behaviour is probably due to scattering electrons inside the anslyser and not due to the residual gases. Figs. (5.2) and (5.3) show the electron energy loss spectra of Kr taken at 27^{o} scattering angle and over an incident energy range of (30 - 45 eV). Similarly, Figs. (5.4), (5.5), and (5.6) show the same set of measurements for a 40^{o} scattering angle and over an incident energy range of (25 - 45 eV). Sharp features are observed at energies 10.1, 10.7, 11.5, 12.4, and 13.1 eV. The energy position of these features are in good agreement with the energy levels of Moore (1952) at 10.03, 10.64, 11.52, 12.35, and 13.0 eV respectively. The spectroscopic configurations of these levels are shown in Fig. (5.2). Figs. (5.7) and (5.8) show the relative intensity ratio (P_{loss}/P_{elast}) of the prominent features of the above spectra as a function of incident electron energy. These results are listed in Tables (5.1) and (5.2). The inelastic cross sections of the prominent peaks for the above spectra are estimated from the relation (5.1). From the measurements of Williams and Crowe (1975)the elastic cross sections of Kr are obtained as follows:

$$\sigma_{elast}\ (\sim 27^{o}) = 25\ a_o^2\ Sr^{-1} \qquad \text{for } E_o = 30 \text{ eV}$$

$$\sigma_{elast}\ (\sim 40^{o}) = 7.38 \pm 0.83\ a_o^2\ Sr^{-1} \qquad \text{for } E_o = 30 \text{ eV}$$

$$\sigma_{elast}\ (\sim 40^{o}) = 4.47 \pm 0.49\ a_o^2\ Sr^{-1} \qquad \text{for } E_o = 40 \text{ eV}$$

where a_o is Bohr radius of hydrogen atom.

The estimated inelastic cross sections of the prominent peaks at incident energies 30 and 40 eV and at (27^{o} and 40^{o}) scattering angles are listed in Tables (5.3) and (5.4).

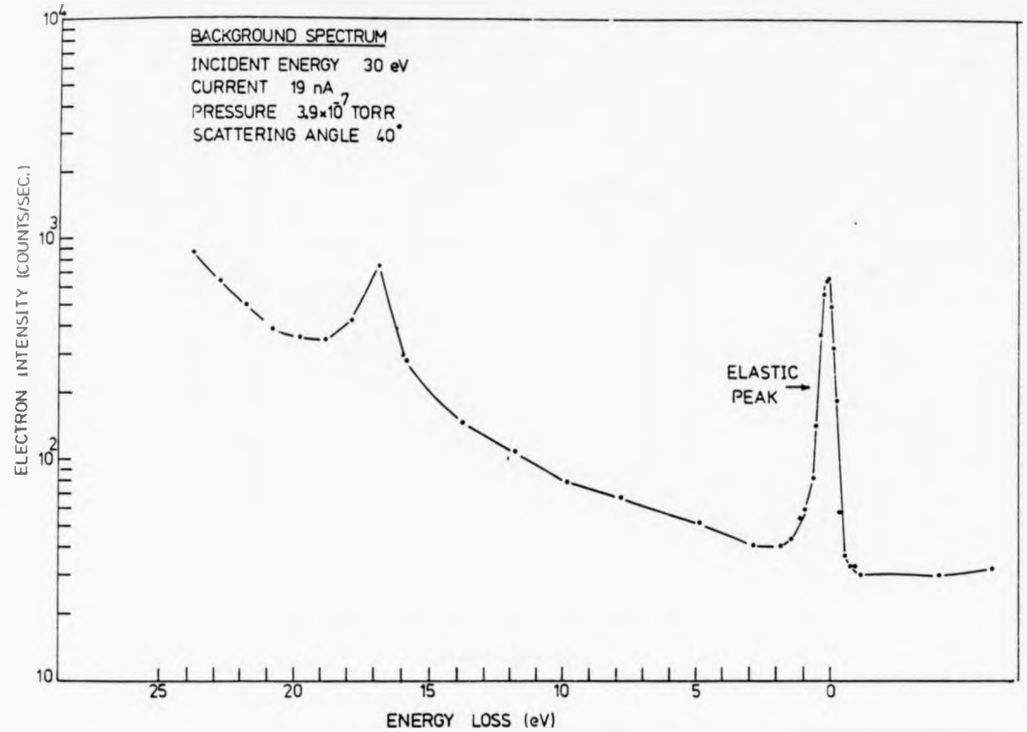

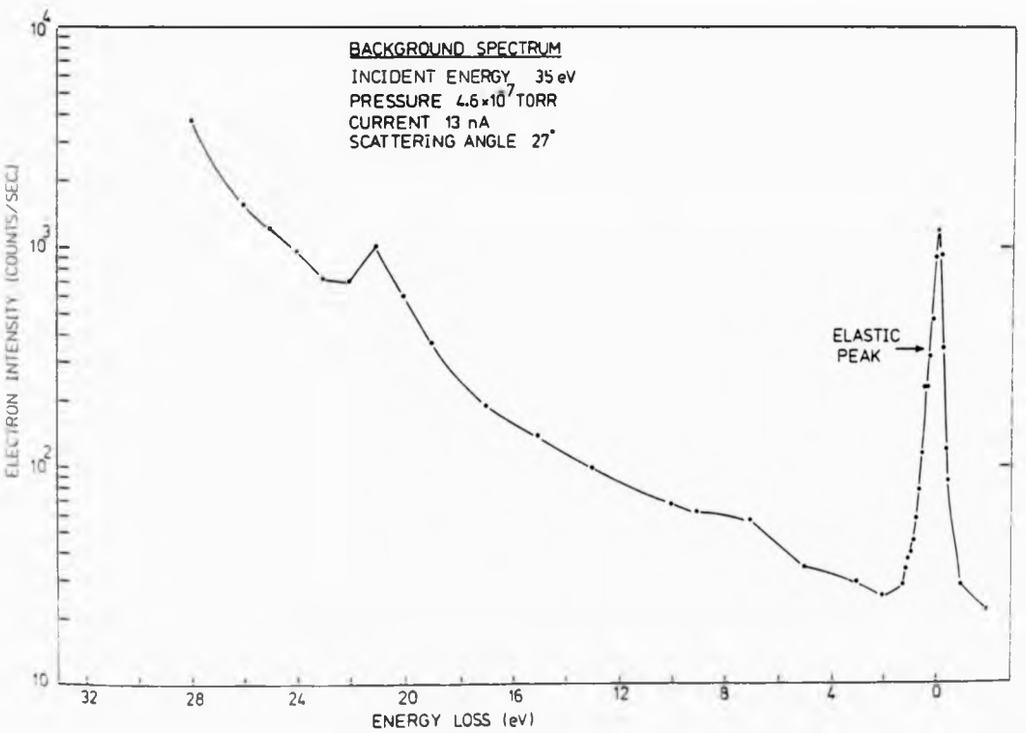

Fig. (5.1): Typical energy loss spectra of background gases

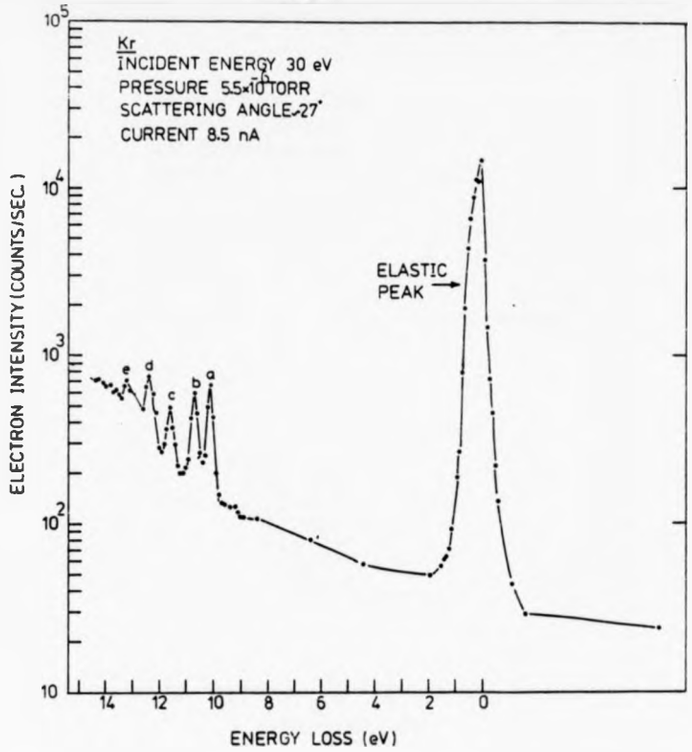

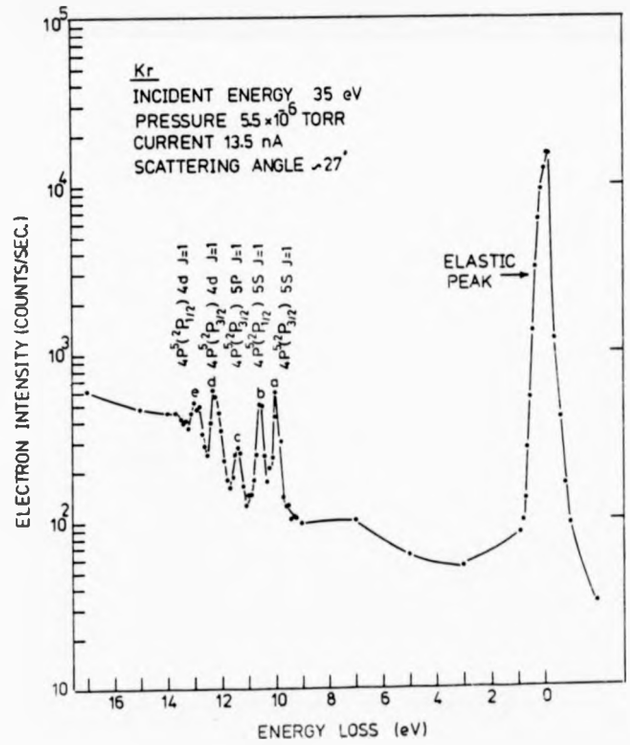

Fig. (5.2): Energy loss spectra of Kr

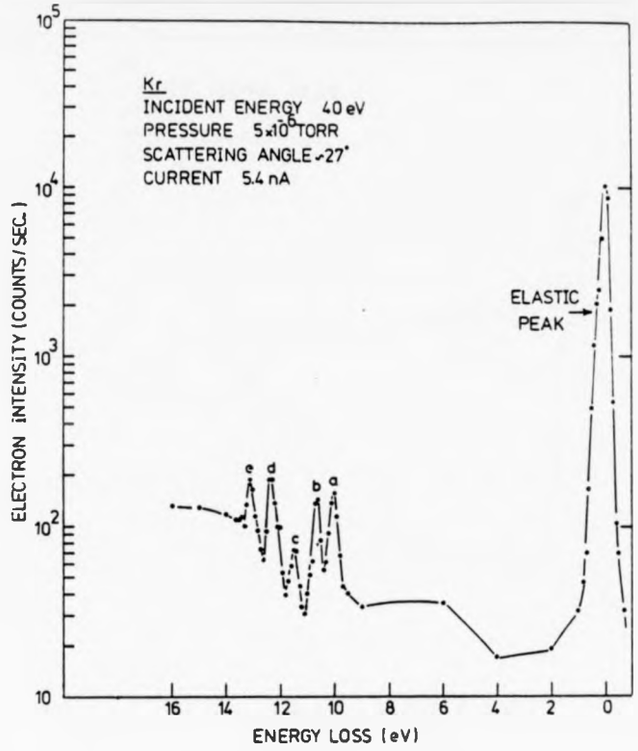

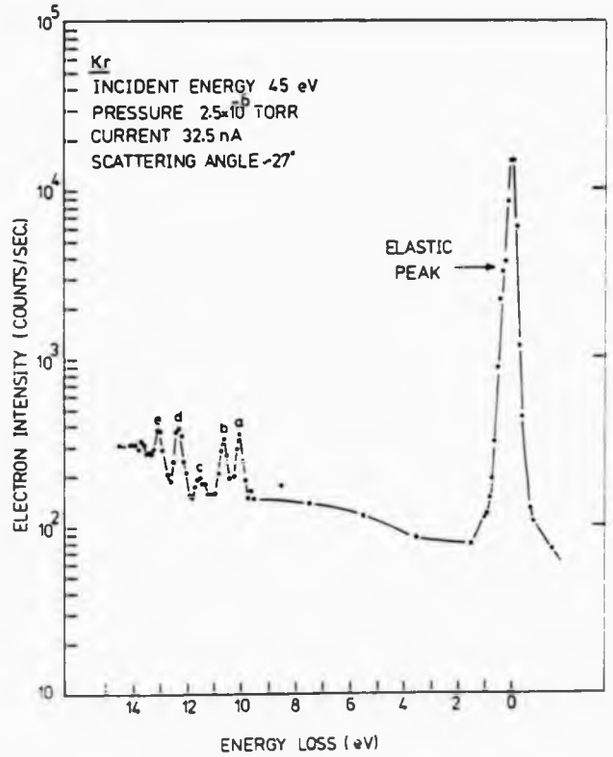

Fig. (5.3): Energy loss spectra of Kr

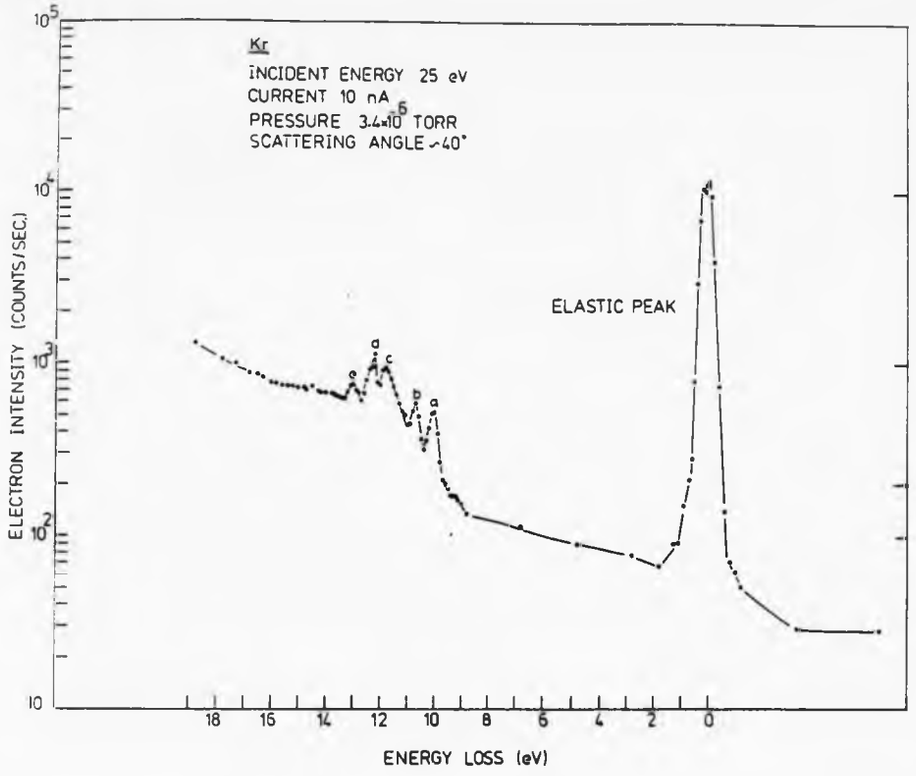

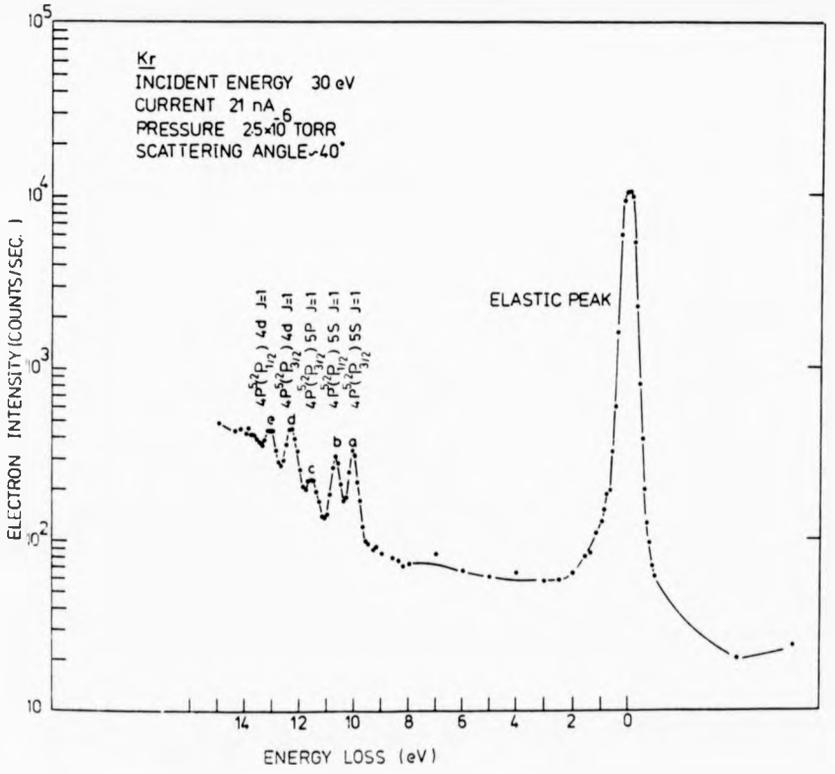

Fig. (5.4): Energy loss spectra of Kr

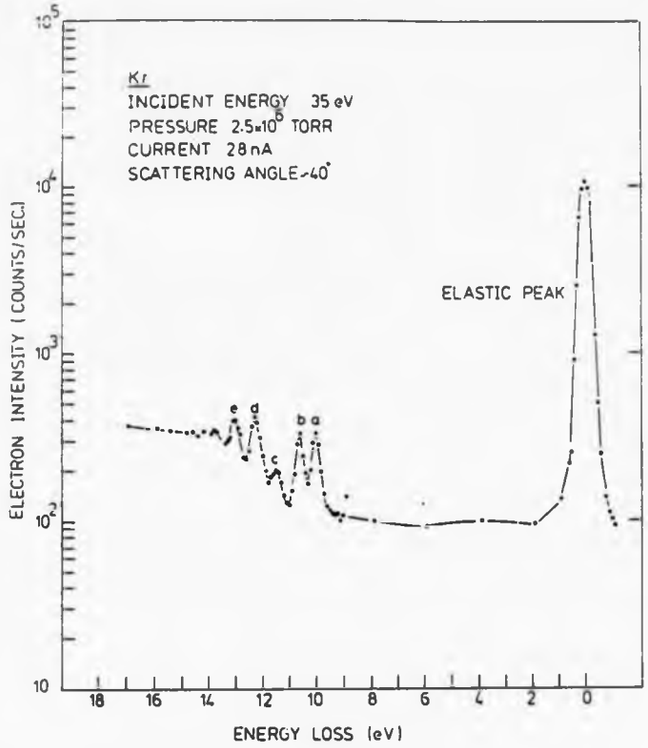

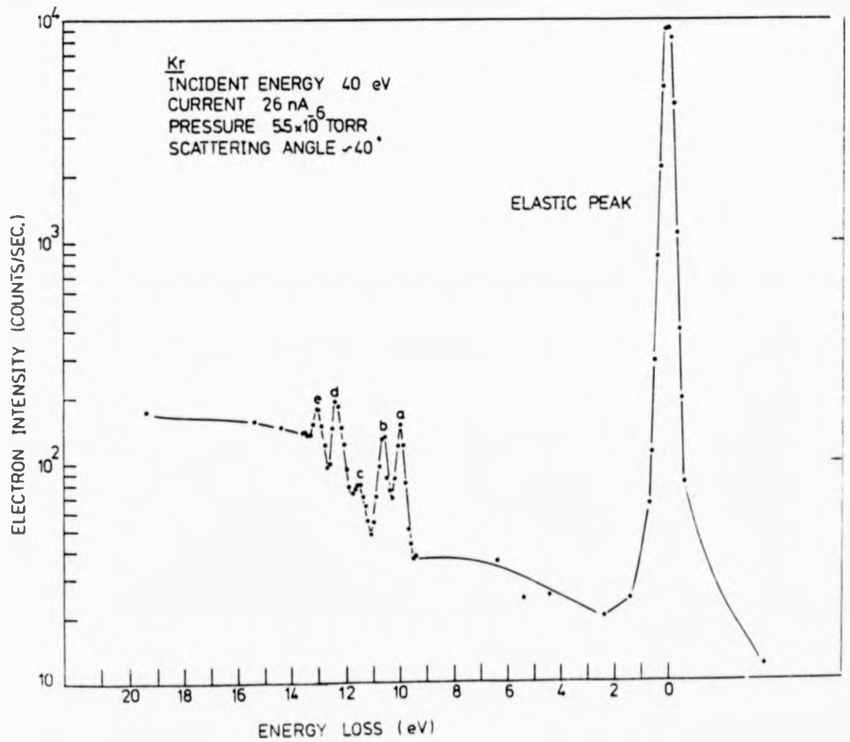

Fig. (5.5): Energy loss spectra of Kr

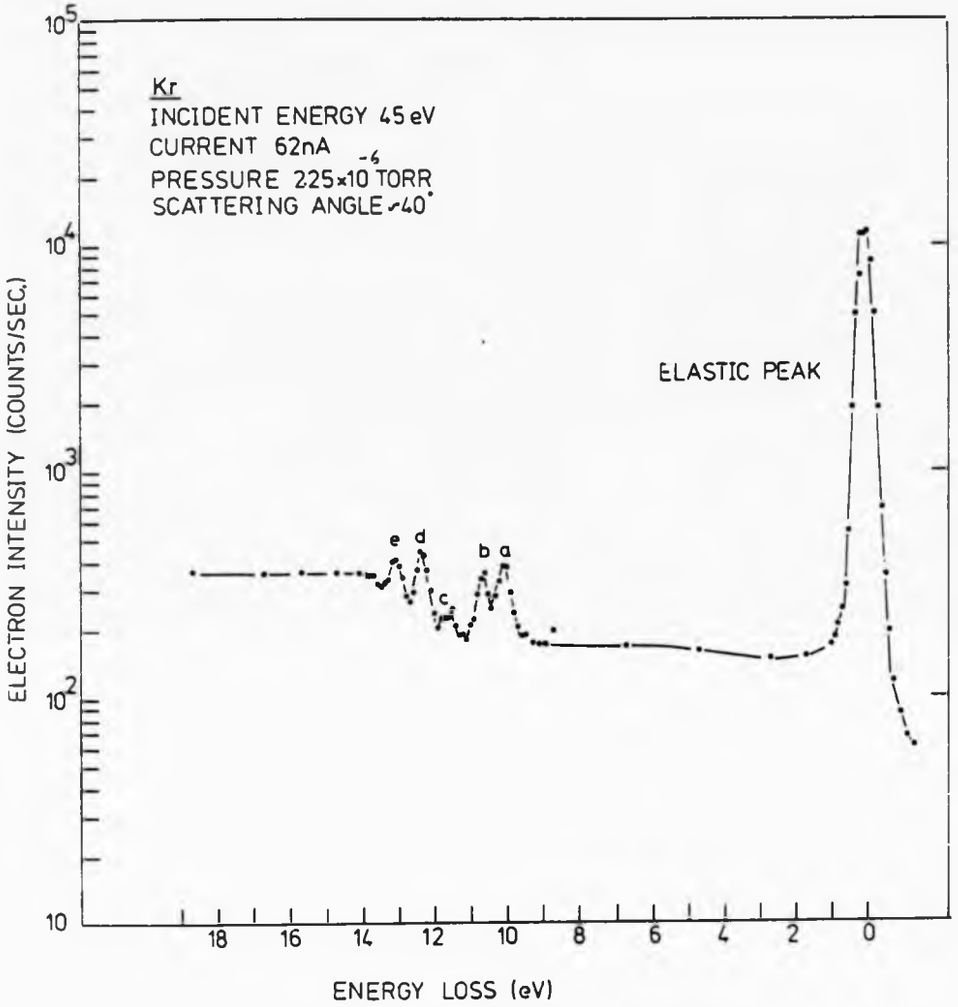

Fig. (5.6): Energy loss spectrum of Kr

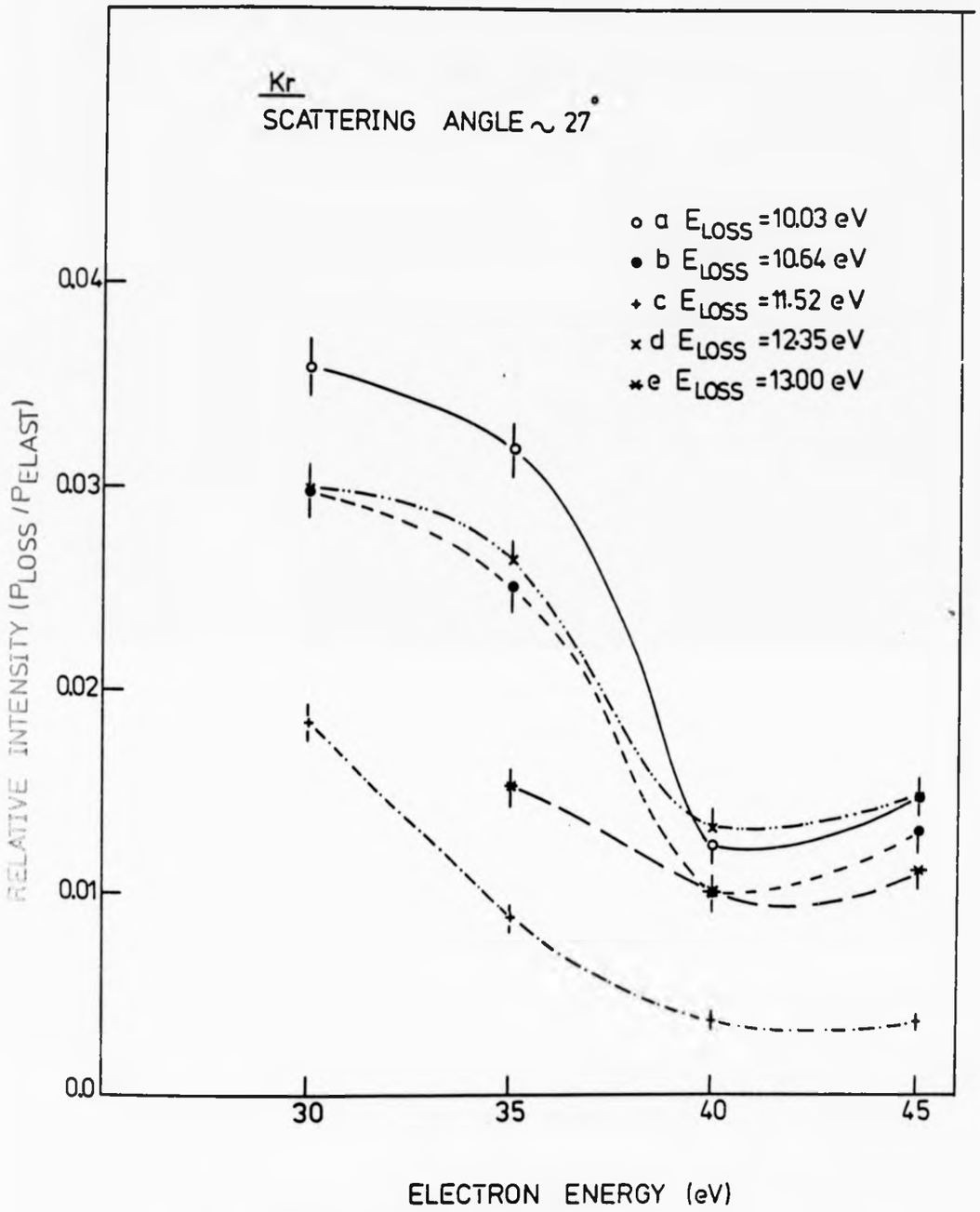

Fig. (5.7): Relative intensity ratio (P_{loss}/P_{elast}) dependence on incident electron energy at 27^{o} scattering angle (1 rms error)

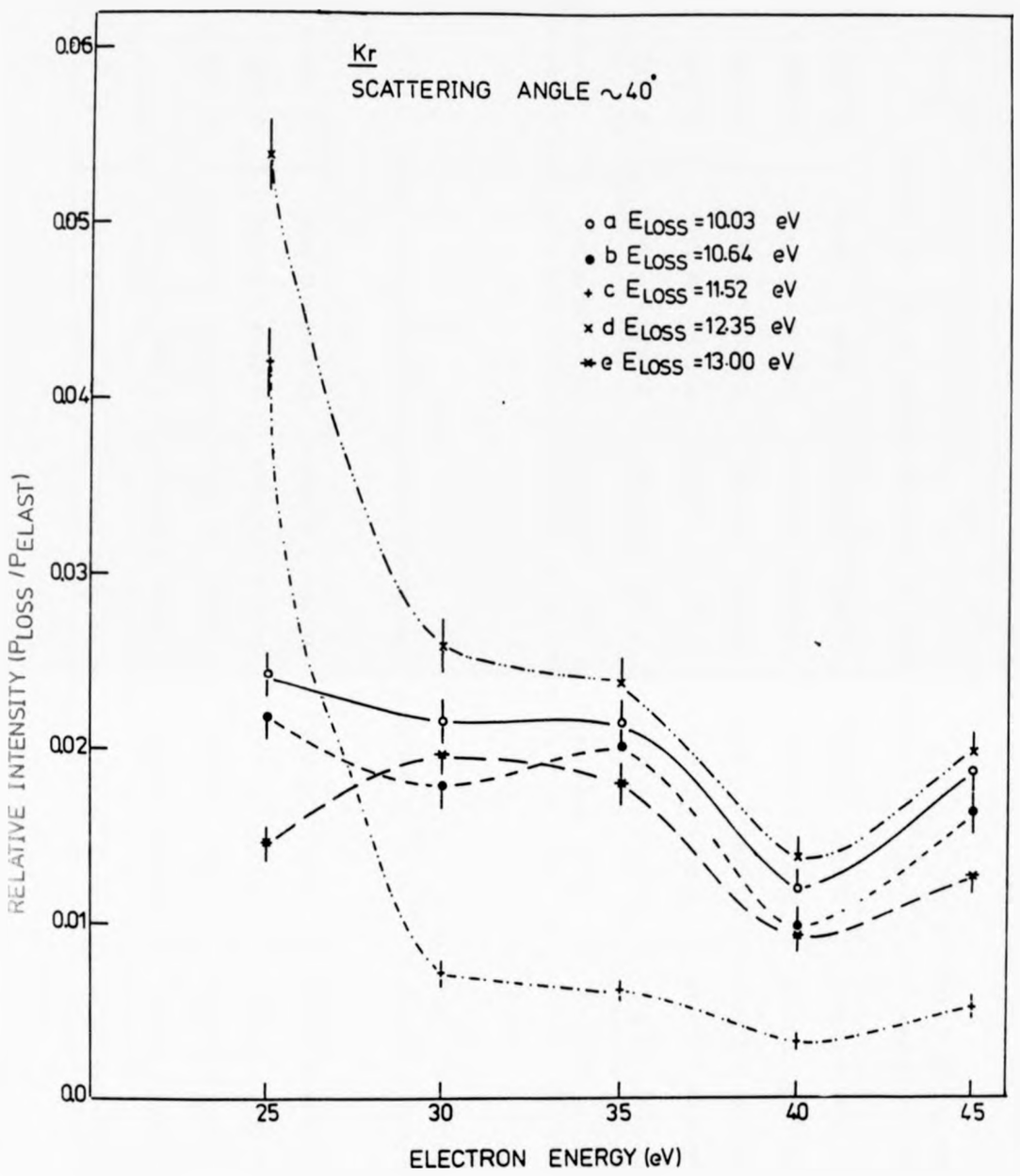

Fig. (5.8): Relative intensity ratio (P_{loss}/P_{elast}) dependence on incident electron energy at 40^{o} scattering angle (1 rms error)

Energy loss / Incident electron energy	E_L = 10.03 eV	E_L = 10.64 eV	E_L = 11.52 eV	E_L = 12.35 eV	E_L = 13.00 eV
30 eV	0.0358 ± 0.0015	0.0298 ± 0.0014	0.0184 ± 0.0011	0.0305 ± 0.0014	
35	0.0319 ± 0.0014	0.0251 ± 0.0012	0.0088 ± 0.0007	0.0264 ± 0.001	0.0153 ± 0.0009
40	0.0124 ± 0.001	0.0109 ± 0.001	0.0037 ± 0.0005	0.0132 ± 0.0011	0.0106 ± 0.001
45	0.0148 ± 0.0009	0.0131 ± 0.0009	0.0037 ± 0.0004	0.0148 ± 0.0009	0.0119 ± 0.0008

Table (5.1): Relative intensity (P_{loss}/P_{elast}) dependence on the incident energy at 27° scattering angle for Kr. (Fig. (5.7)).

Energy loss / Incident electron energy	E_L = 10.03 eV	E_L = 10.64 eV	E_L = 11.52 eV	E_L = 12.35 eV	E_L = 13.00 eV
25 eV	0.0243 ± 0.0014	0.0218 ± 0.0013	0.0421 ± 0.0019	0.0538 ± 0.0021	0.0147 ± 0.0011
30	0.0216 ± 0.0014	0.0179 ± 0.0013	0.0072 ± 0.0008	0.0259 ± 0.0015	0.0197 ± 0.0013
35	0.0215 ± 0.0014	0.0207 ± 0.0014	0.0062 ± 0.0007	0.0238 ± 0.0015	0.0181 ± 0.0013
40	0.0120 ± 0.0011	0.0099 ± 0.001	0.0032 ± 0.0005	0.0138 ± 0.0012	0.0094 ± 0.001
45	0.0188 ± 0.0013	0.0164 ± 0.0012	0.0052 ± 0.0006	0.0199 ± 0.0013	0.0128 ± 0.001

Table (5.2): Relative intensity (P_{loss}/P_{elast}) dependence on the incident energy at 40° scattering angle for Kr. (Fig. (5.8)).

Energy loss / Incident electron energy	E_L = 10.03 eV	E_L = 10.64 eV	E_L = 11.52 eV	E_L = 12.35 eV
30 eV	0.8950	0.7450	0.4600	0.7625

Table (5.3): Inelastic cross sections (in a_o^2 Sr^{-1}) of Kr at 27^o scattering angle.

Energy loss / Incident electron energy	E_L = 10.03 eV	E_L = 10.64 eV	E_L = 11.52 eV	E_L = 12.35 eV	E_L = 13.00 eV
30 eV	0.1595 ± 0.0205	0.1321 ± 0.0175	0.0531 ± 0.0083	0.1911 ± 0.0239	0.1434 ± 0.0188
40	0.0536 ± 0.0077	0.0443 ± 0.0066	0.0143 ± 0.0027	0.0617 ± 0.0086	0.0420 ± 0.0064

Table (5.4): Inelastic cross sections (in a_o^2 Sr^{-1}) of Kr at 40^o scattering angle.

The upper part of Fig. (5.9) shows the differential excitation functions of $^3P_1$ and $^1P_1$ (10.03 and 10.64 eV energy loss) at 27° scattering angles. These results indicate a maximum at 25 eV incident electron energy The lower part shows the ratio of differential excitation functions of the above states to the background intensity. These measurements indicate a maximum at 35 eV incident electron energy. These results guided us (see Chapter 6) in the selection of the most desirable electron energy for the coincidence experiment.

The same set of measurements for a scattering angle of 40° are shown in Fig. (5.10). Again, there is a maximum for the differential excitation function at ∿25 eV energy loss, whereas the 10.64 eV energy loss shows no such maximum (possibly it was missed by not giving low enough energy). The lower part shows the ratio of differential excitation functions of the above state to the background intensity. As in the case of the 27° scattering angle experiment, both states show a maximum at 35 eV.

5.2.2 Xenon

Figs. (5.11) and (5.12) show the energy loss spectra of Xe taken at a scattering angle of 27° and over an incident electron energy range from 30 to 40 eV.

Similarly, Figs. (5.13), (5.14), and (5.15) show the same set of measurements for a scattering angle of 40° over an incident electron energy range from 25 to 45 eV. Sharp features are observed at 8.4, 9.6, 9.9, 10.3, 11, 11.6, and 12.4 eV. The energy position of these features are in good agreement with the energy levels of Moore (1958) at

Fig. (5.9): The upper part shows the differential excitation functions of the $^3P_1$ and $^1P_1$ states (10.03 and 10.64 eV energy loss) of Kr at 27^o scattering angle.

The lower part shows the ratio of differential excitation functions of the above states to the background intensity at the same scattering angle (1 rms error).

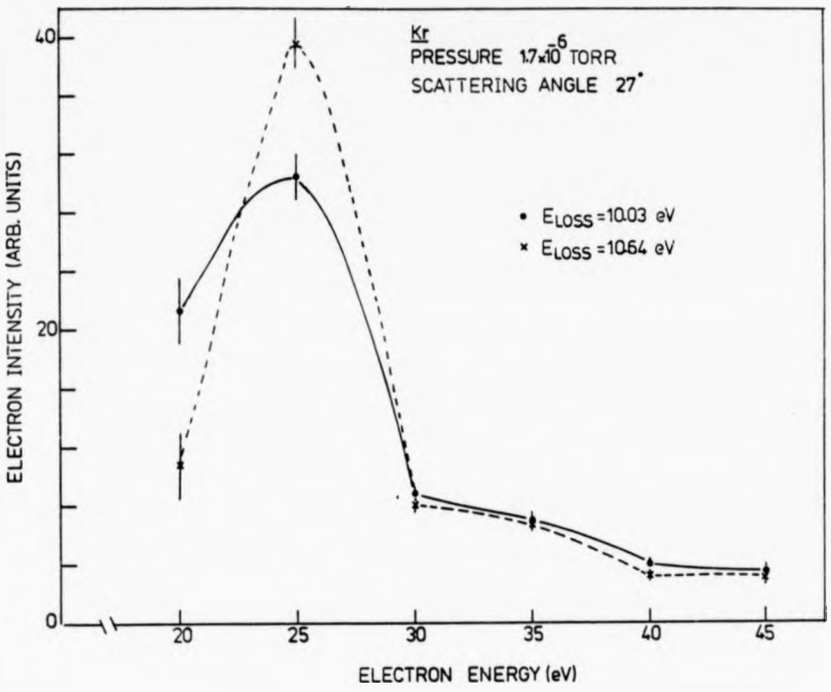
Kr
PRESSURE 1.7×10⁻⁶ TORR
SCATTERING ANGLE 27°
• E_LOSS = 10.03 eV
× E_LOSS = 10.64 eV
ELECTRON INTENSITY (ARB. UNITS)
0
20
40
20
25
30
35
40
45
ELECTRON ENERGY (eV)

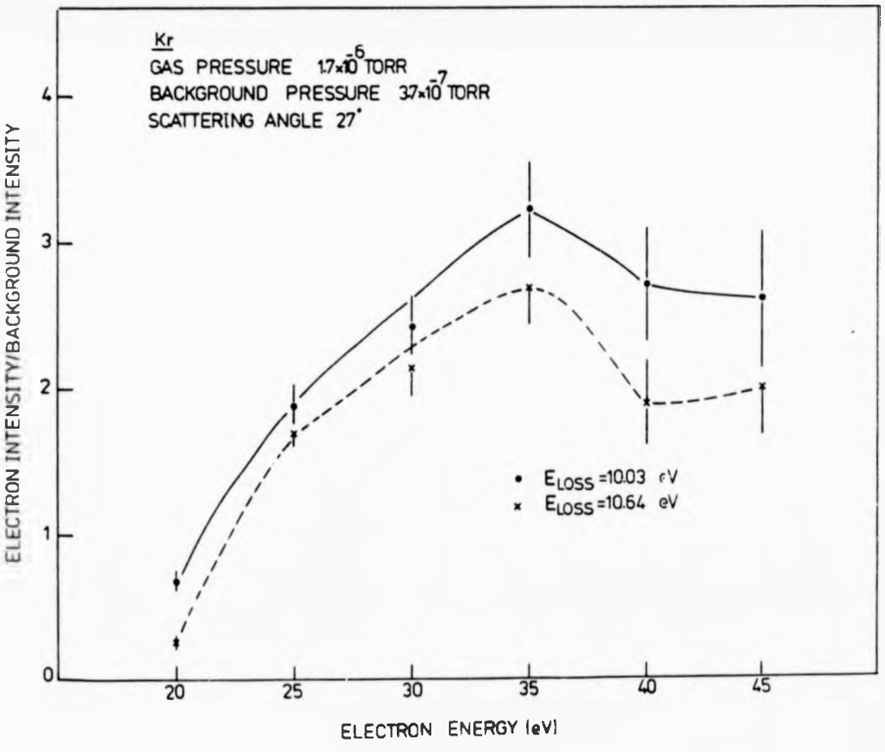
Kr
GAS PRESSURE 1.7×10⁻⁶ TORR
BACKGROUND PRESSURE 3.7×10⁻⁷ TORR
SCATTERING ANGLE 27°
• E_LOSS = 10.03 eV
× E_LOSS = 10.64 eV
ELECTRON INTENSITY/BACKGROUND INTENSITY
0
1
2
3
4
20
25
30
35
40
45
ELECTRON ENERGY (eV)

Fig. (5.10): The upper part shows the differential excitation functions of the $^3P_1$ and $^1P_1$ states of Kr at $\sim 40^o$ scattering angle.

The lower part shows the ratio of the differential excitation functions of the above states to the background intensity at the same scattering angle (1 rms error).

ial excitation

o scattering

al excitation

intensity at

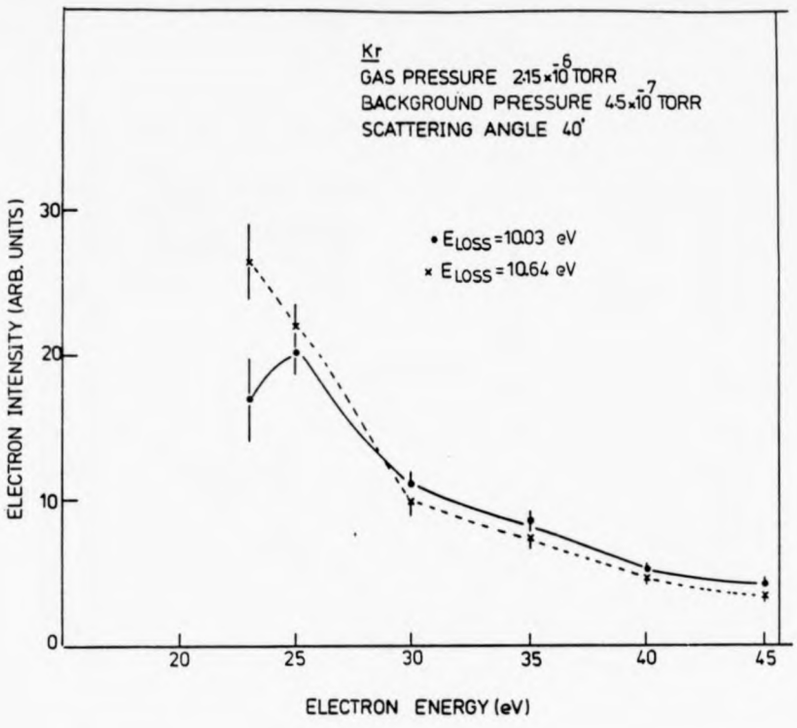

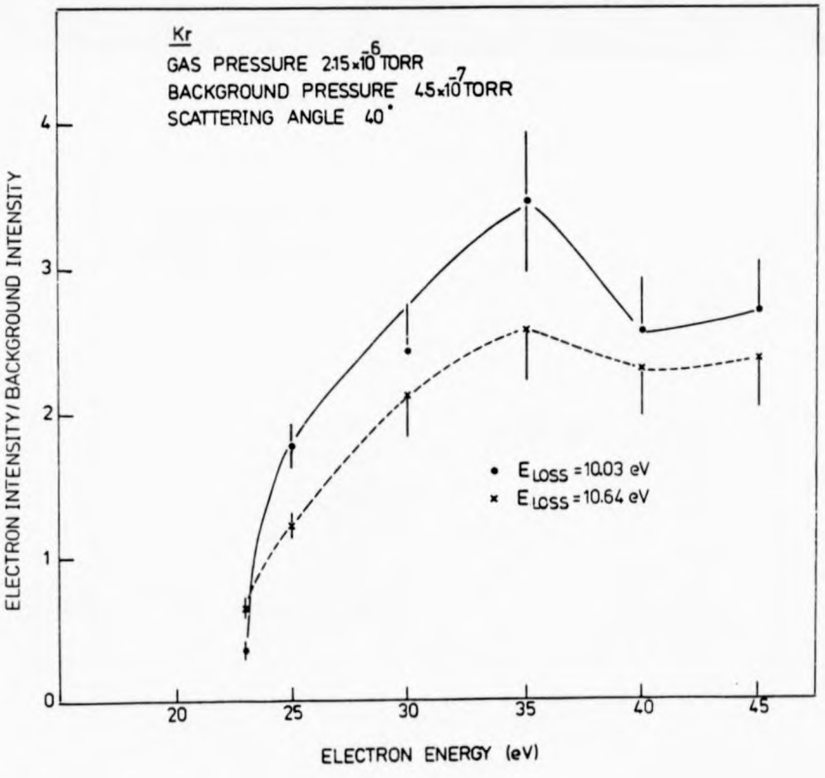

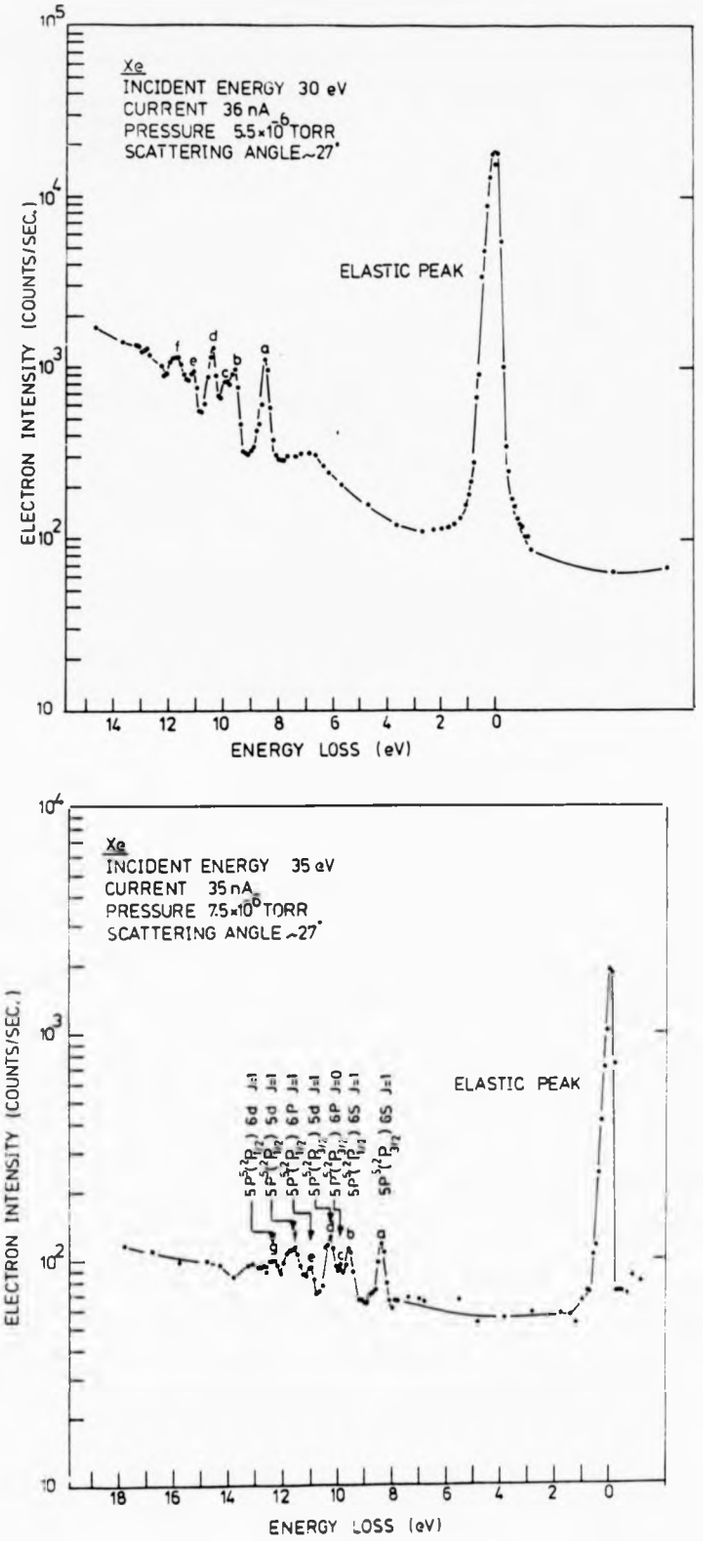

Fig. (5.11): Energy loss spectra of Xe

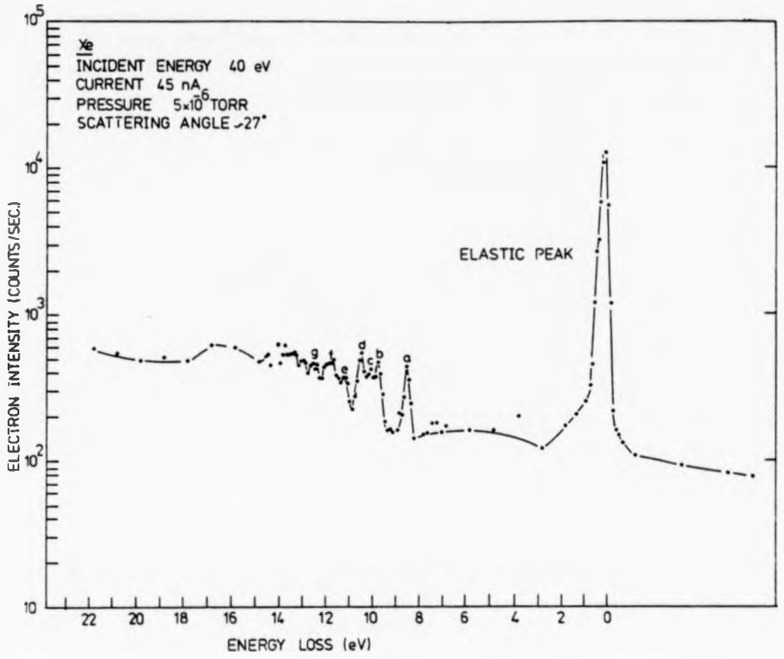

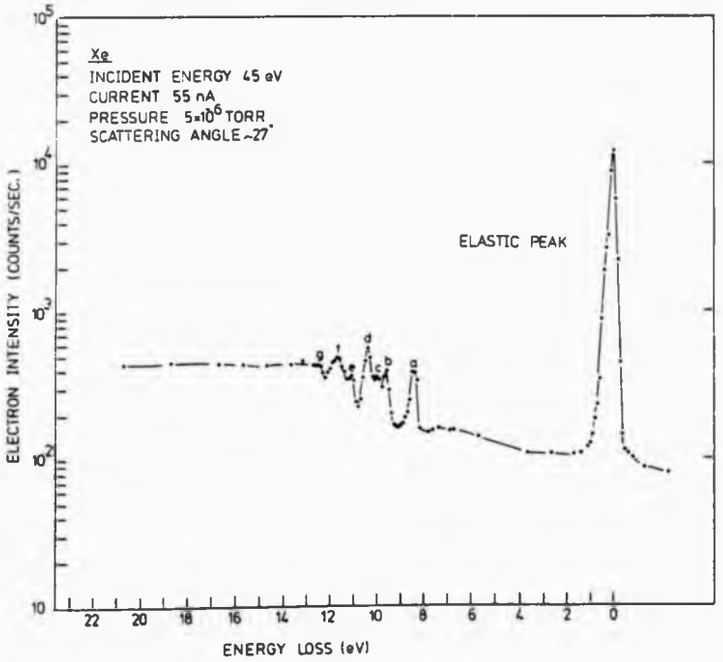

Fig. (5.12): Energy loss spectra of Xe

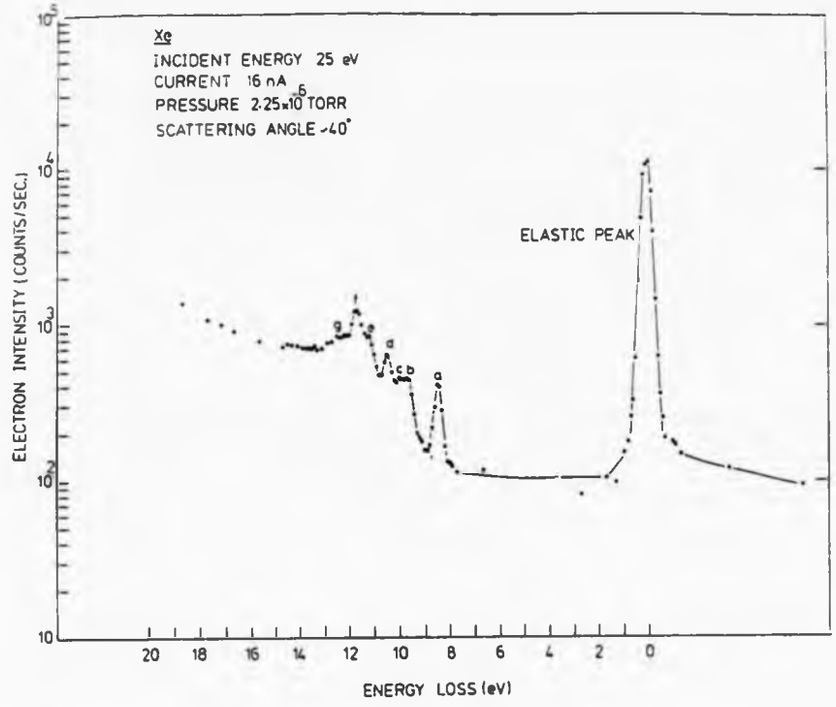

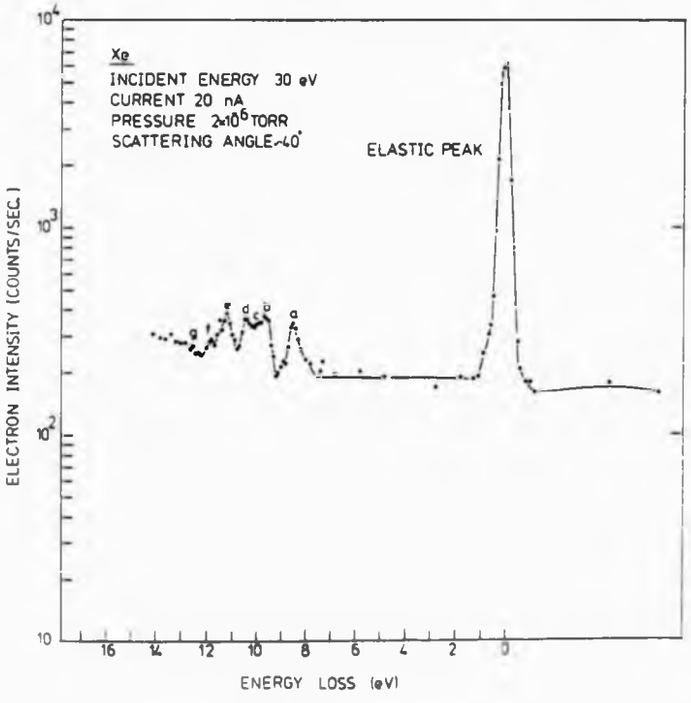

Fig. (5.13): Energy loss spectra of Xe

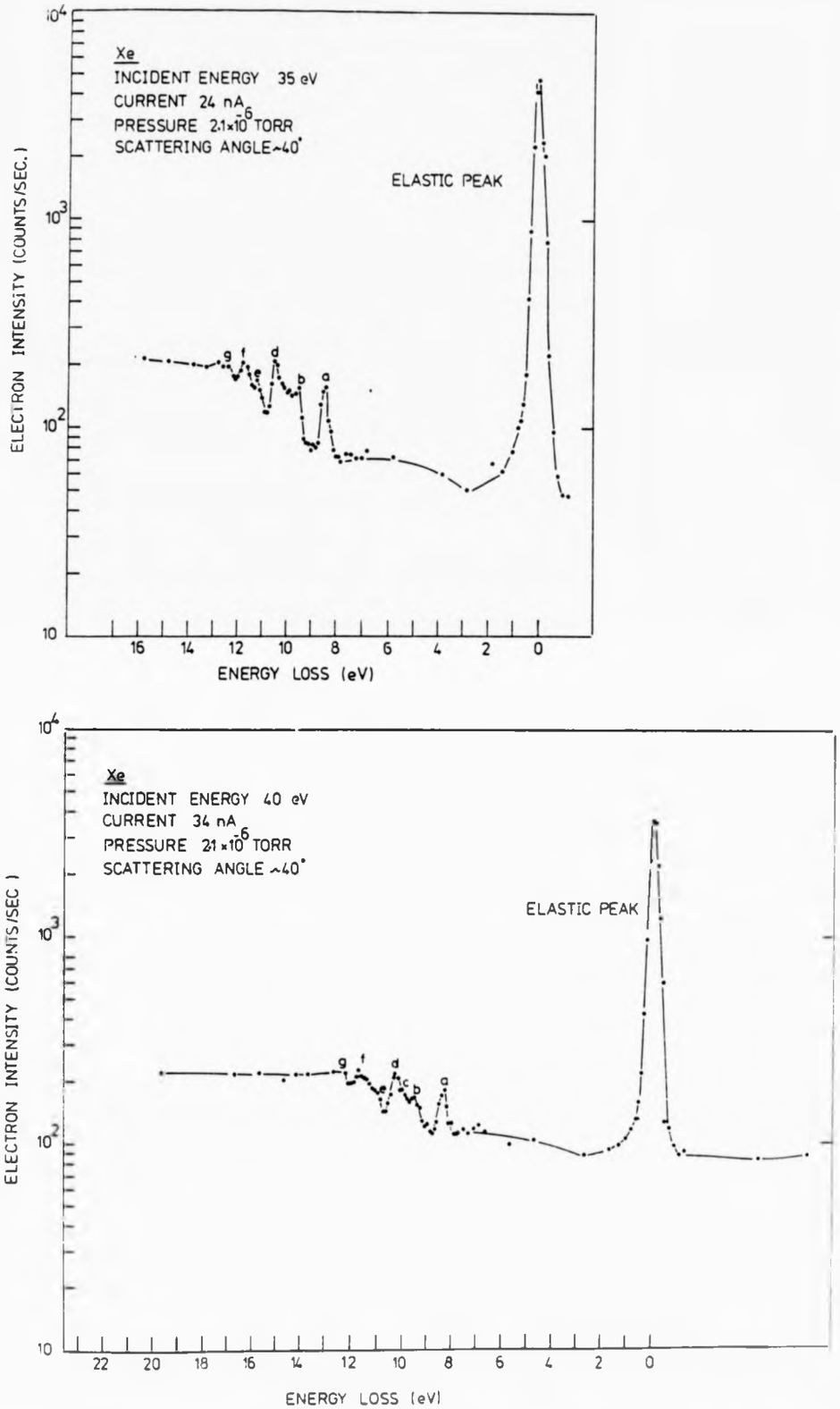

Fig. (5.14): Energy loss spectra of Xe

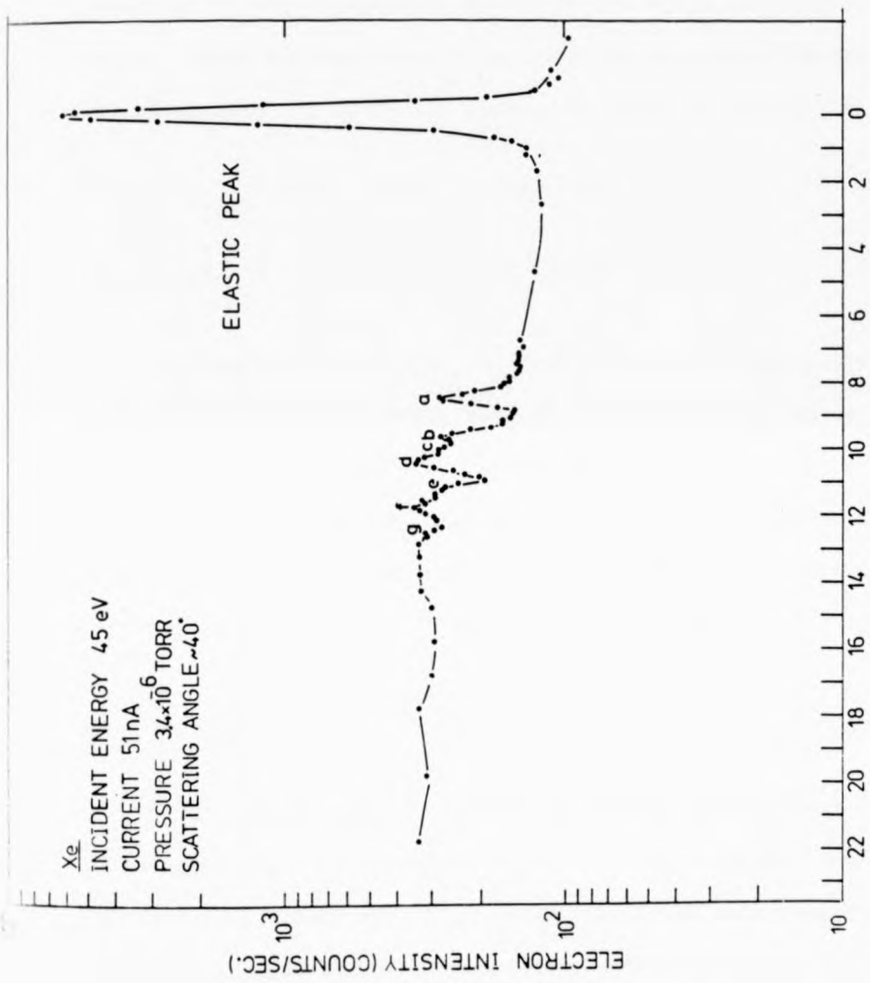

Fig. (5.15): Energy loss spectrum of Xe

8.43, 9.56, 9.93, 10.4, 10.95, 11.60 and 12.45 eV respectively. The spectroscopic configurations of these features are shown in Fig. (5.11). Fig. (5.16) shows the relative intensity ratio (P_{loss}/P_{elast}) of the prominent peaks as a function of incident electron energy. These results are listed in Tables (5.5) and (5.6). The inelastic cross sections of the prominent peaks of Xe are estimated from the relation (5.1). From the measurements of Williams and Crowe (1975) the elastic cross section of Xe at 40^{o} scattering angle is obtained as follows:

$$\sigma_{elast}(\sim 40^{o}) = 6.89 \pm 0.072\ a_o^2\ Sr^{-1} \qquad \text{for } E_o = 30 \text{ eV}$$

$$\therefore \sigma_{loss}(\sim 40^{o}) \text{ for 8.43 energy loss} = 0.1860 \pm 0.0146\ a_o^2\ Sr^{-1} \qquad \text{for } E_o = 30 \text{ eV}$$

The upper part of Fig. (5.17) shows the differential excitation function for 8.43 eV energy loss at a 40^{o} scattering angle. The data show no maximum in the electron energy range of (25 - 45 eV). The lower part shows the ratio of differential excitation functions for the above state to the background intensity. These results indicate a maximum at about 30 eV incident electron energy.

5.2.3 Argon

Figs. (5.18) and (5.19) show the energy loss spectra of Ar at 30^{o} scattering angle and over an incident electron energy range from 30 to 45 eV. Similarly, Fig. (5.20) shows the same measurements at 40^{o} scattering angle and 35 eV incident electron energy. Features are observed at 11.8, 13.3, 13.9, 14.3 and 15.2 eV. The energy positions of these features are in good agreement with the energy levels of Moore (1949) at 11.82, 13.32, 13.90, 14.3 and 15.2 eV respectively. The spectroscopic configurations of these features are shown in Fig. (5.18). Fig. (5.21) shows the relative intensity ratio (P_{loss}/P_{elast}) of the prominent peaks

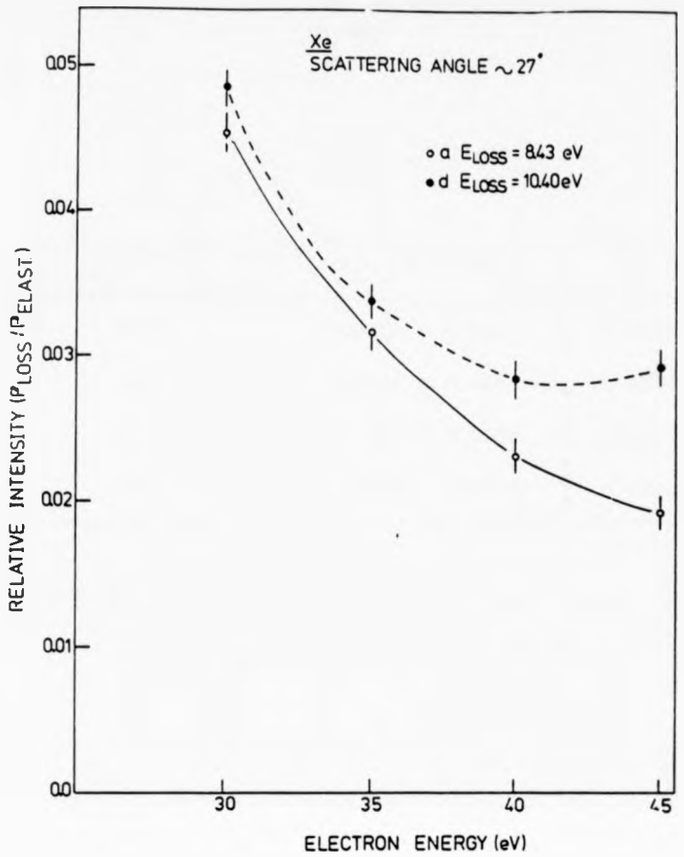

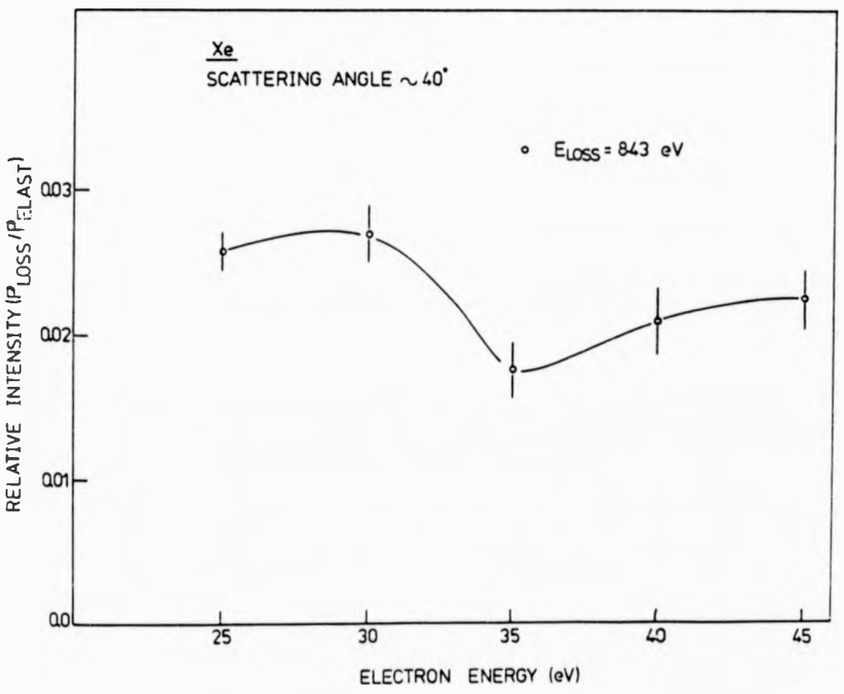

Fig. (5.16): Relative intensity ratio (P_{loss}/P_{elast}) dependence on the incident electron energy at 27° scattering angle (1 rms error)

Energy loss / Incident electron energy	E_L = 8.43 eV	E_L = 10.40 eV
30 eV	0.0454 ± 0.0015	0.0486 ± 0.0016
35	0.0317 ± 0.0013	0.0338 ± 0.0013
40	0.0232 ± 0.0013	0.0285 ± 0.0014
45	0.0193 ± 0.0012	0.0293 ± 0.0015

Table (5.5): Relative intensity (P_{loss}/P_{elast}) dependence on the incident electron energy at $\sim 27^{o}$ scattering angle for Xe. (Fig. (5.16)).

Energy loss / Incident electron energy	E_L = 8.43 eV
25 eV	0.0258 ± 0.0015
30	0.027 ± 0.0021
35	0.0177 ± 0.0019
40	0.0210 ± 0.0024
45	0.0226 ± 0.0019

Table (5.6): Relative intensity (P_{loss}/P_{elast}) dependence on the incident electron energy at 40^{o} scattering angle for Xe. (Fig. (5.16)).

Fig. (5.17): The upper part shows the differential excitation functions of the $^3P_1$ state (8.43 eV energy loss) of Xe at 40^o scattering angle.

The lower part shows the ratio of the differential excitation functions of the above state to the background intensity (1 rms error).

ial excitation

of Xe at 40°

al excitation

ntensity

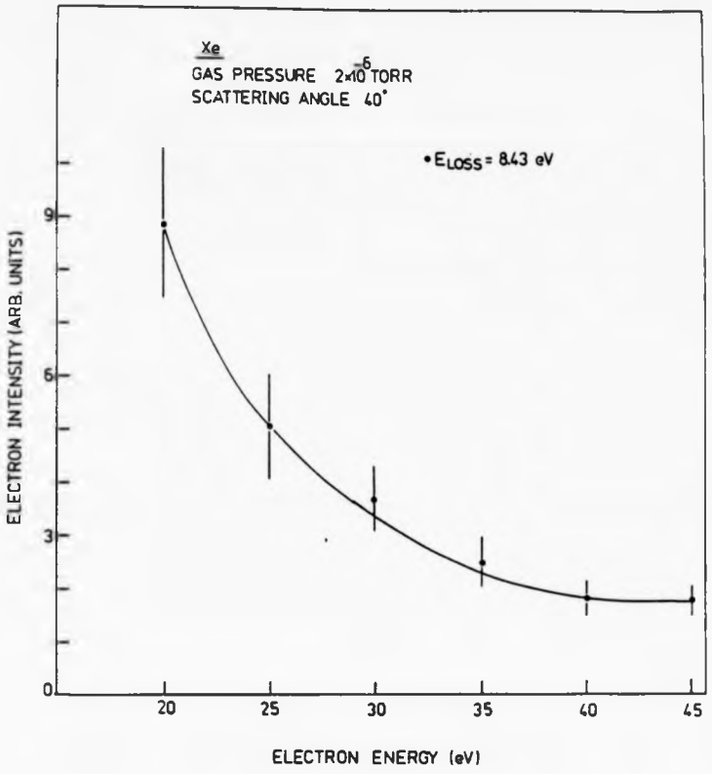

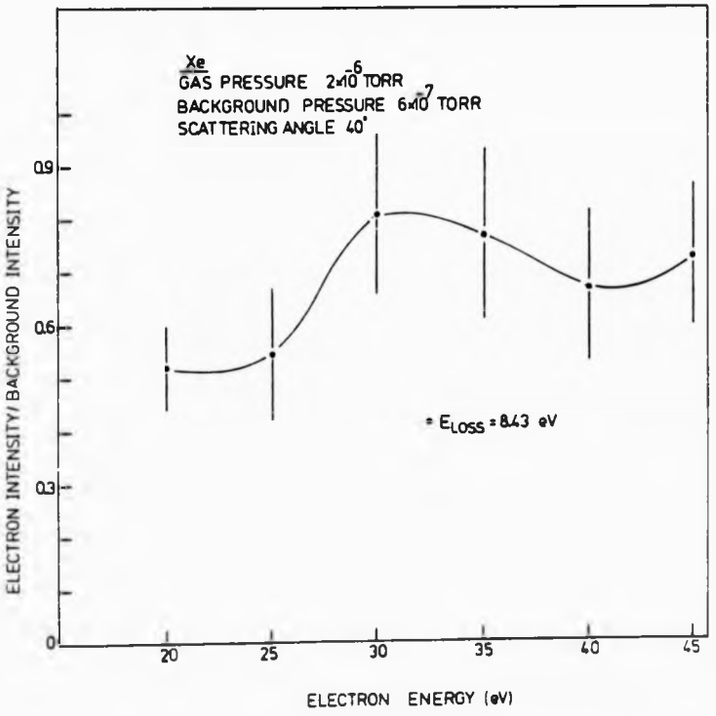

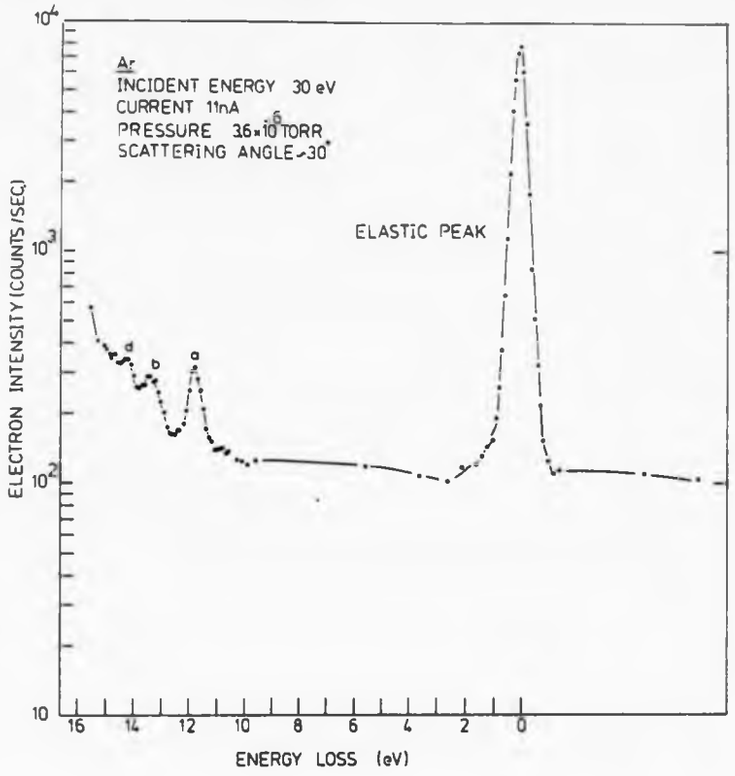

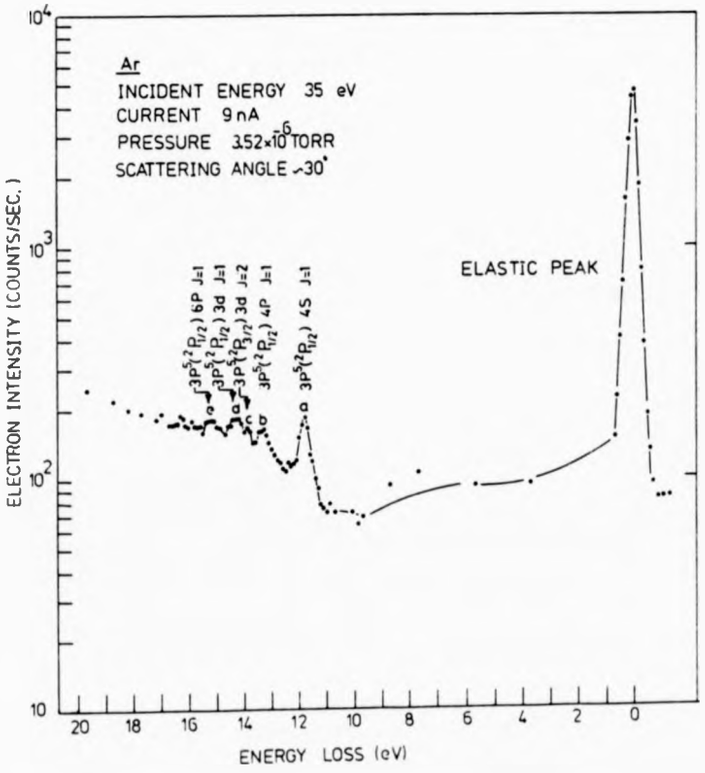

Fig. (5.18): Energy loss spectra of Ar

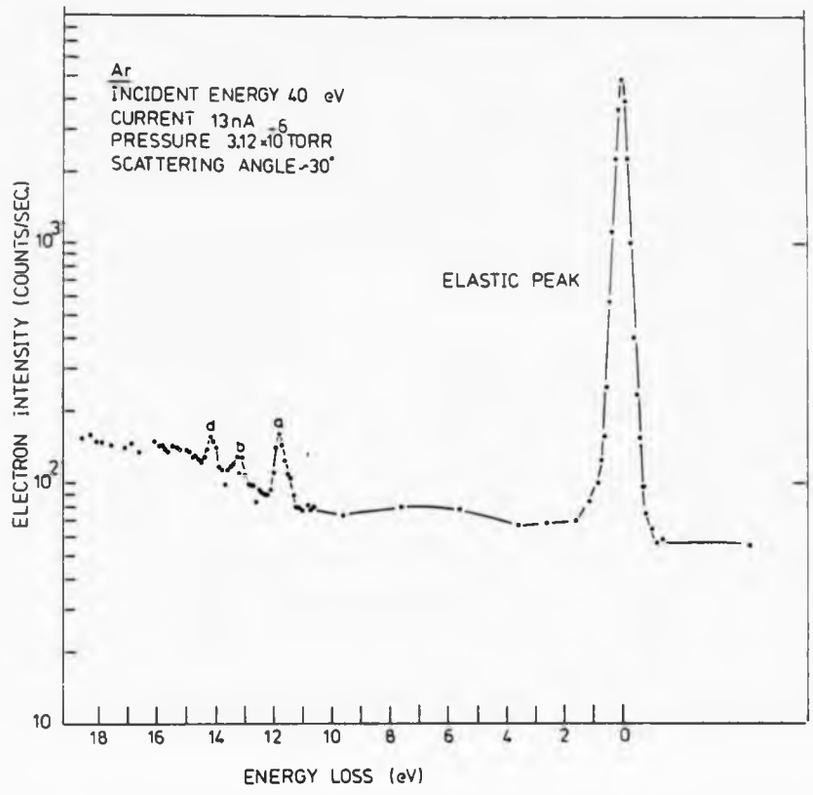

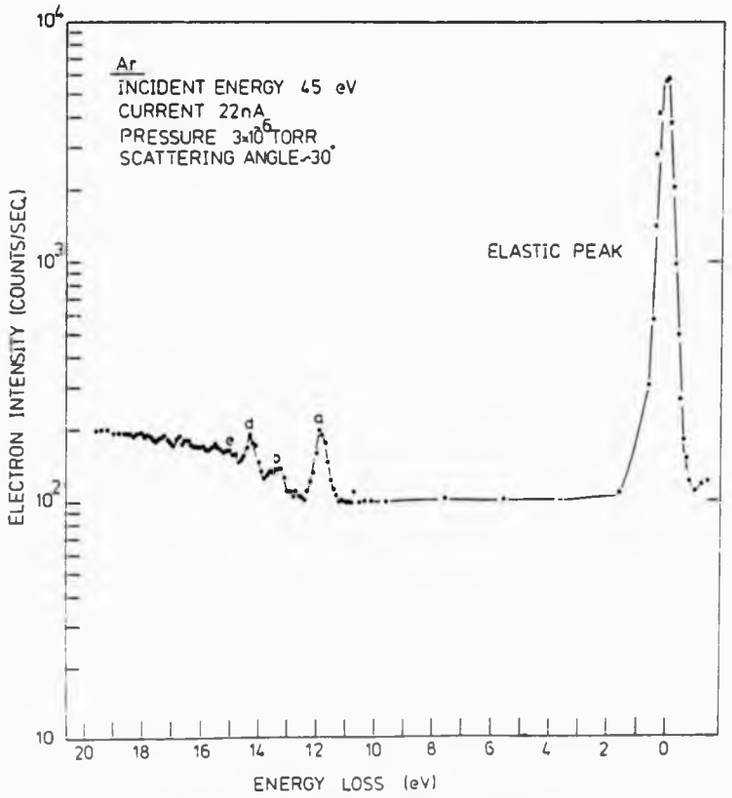

Fig. (5.19): Energy loss spectra of Ar

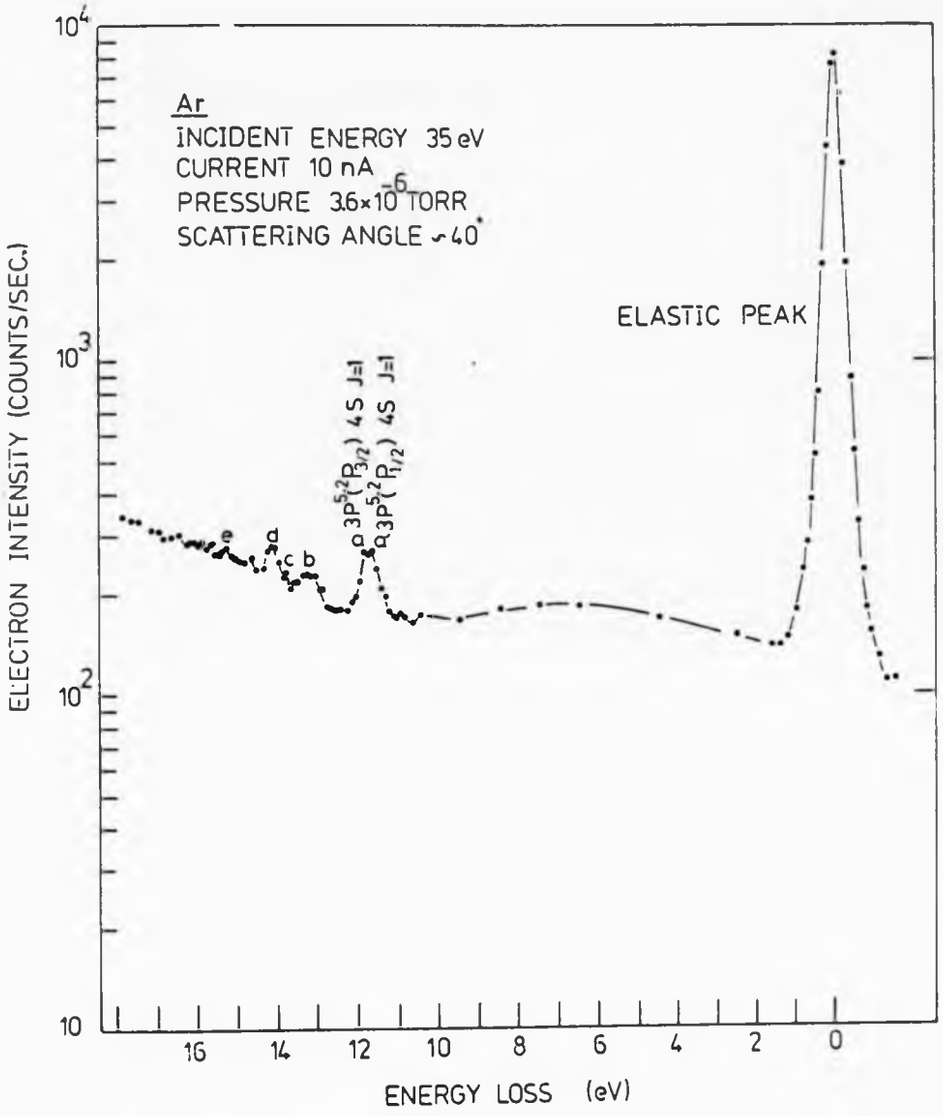

Fig. (4.20): Energy loss spectra of Ar

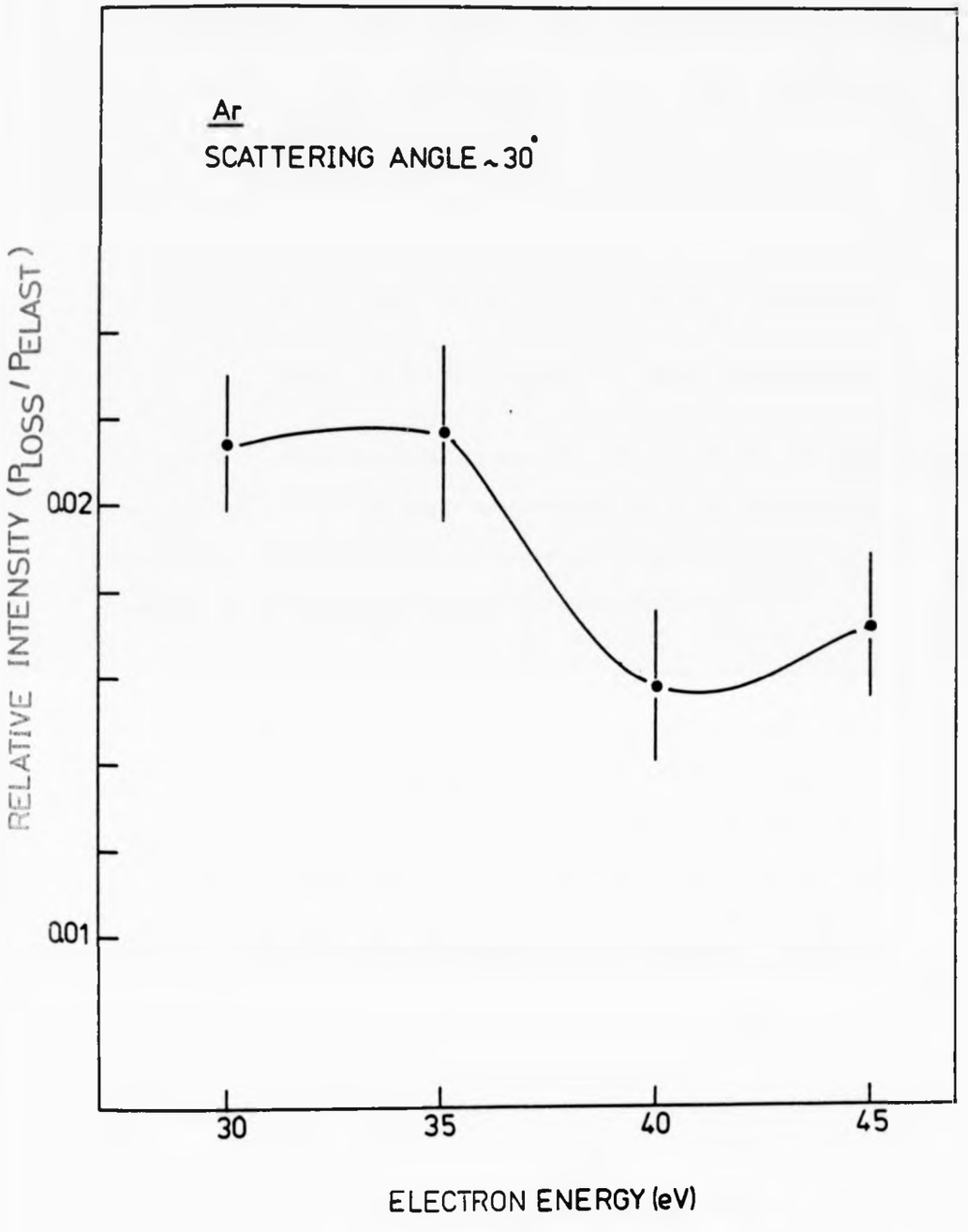

Fig. (5.21): Relative intensity ratio (P_{loss}/P_{elast}) dependence on the incident electron energy at 30^{o} scattering angle (1 rms error).

as a function of incident electron energy. These results are listed in Table (5.7). The inelastic cross sections of the prominent peaks for the above spectra are estimated from the relation (5.1). From the measurements of Williams and Willis (1975) the elastic cross sections of Ar are obtained as follows

$$\sigma_{elast}(30^{o}) = 15.8 \pm 0.18\ a_o^2\ Sr^{-1} \qquad \text{for } E_o = 29.984 \text{ eV}$$

$$\sigma_{elast}(30^{o}) = 10.3 + 0.11\ a_o^2\ Sr^{-1} \qquad \text{for } E_o = 40.002 \text{ eV}$$

The inelastic cross sections of the 3p - 4s, s' (11.62 + 11.82 eV energy loss) at 30^{o} scattering angle are compared with the theoretical predictions of Sawada et al (1971) and with experimental results of Lewis et al (1975) and are listed in Table (5.8).

The upper part of Fig. (5.22) shows the differential excitation function of the 3p - 4s, s' of Ar at 30^{o} scattering angle. This part also shows the energy dependence of the differential inelastic cross section of the above states of Ar at the same scattering angle (Sawada et al, 1971). These results show a maximum at about 25 eV while the present measurements show no maximum at that incident energy. The lower part gives the ratio of differential excitation function of the above states to the background intensity. These results indicate a maximum at about 30 eV incident electron energy.

5.2.4 Helium

Fig. (5.23) shows a typical energy loss spectra of helium at incident electron energies 40 and 45 eV and at 35^{o} scattering angle. The strong peak in the spectrum is the combination of the unresolved 2^1P and 2^3P states which appear at 21.2 eV. The 2^1S state is not

Energy loss / Incident electron energy	E_L = 11.62 + 11.82 eV
30 eV	0.0214 ± 0.0016
35	0.0217 ± 0.0021
40	0.0158 ± 0.0018
45	0.0172 ± 0.0017

Table (5.7): Relative intensity ratio (P_{loss}/P_{elast}) dependence on the incident electron energy at $\sim 30^{o}$ scattering angle (Fig. (5.21)).

Incident energy	Present work	Theoretical values of Sawada et al (1971)	Experimental values of Lewis et al (1975)
30 eV	0.3381±0.0253	∿0.3	∿0.07
40 eV	0.1627±0.0185	∿0.224	∿0.08

Table (5.8): Inelastic cross sections (in $a_o^2\ Sr^{-1}$) of 3p - 4s s' states of Ar at 30^{o} scattering angle are compared with the theoretical values of Sawada et al (1971) and with the experimental values of Lewis et al (1975).

Fig. (5.22): The upper part shows the differential excitation function of the 3p - 4s, s' states (11.62 + 11.82 eV energy loss) of Ar at 30^{o} scattering angle.

This part also shows the energy dependence of the differential inelastic cross sections of the above states and same scattering angle (Sawada et al (1971)).

The lower part shows the ratio of the differential excitation function of the above state to the background intensity (1 rms error).

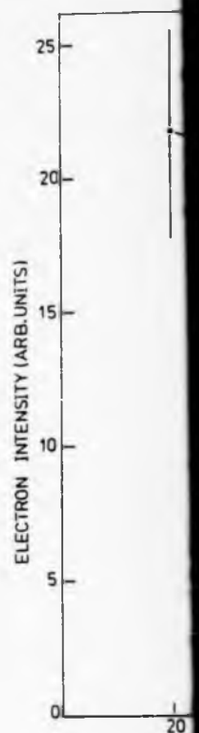

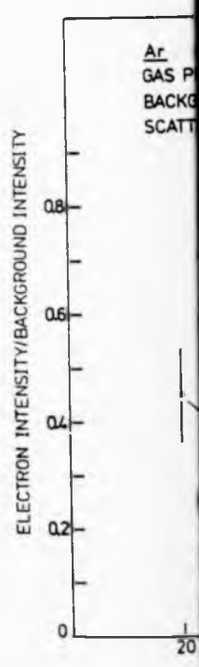

ntial excitation

.82 eV energy

the differential

nd same

tial excitation

ntensity

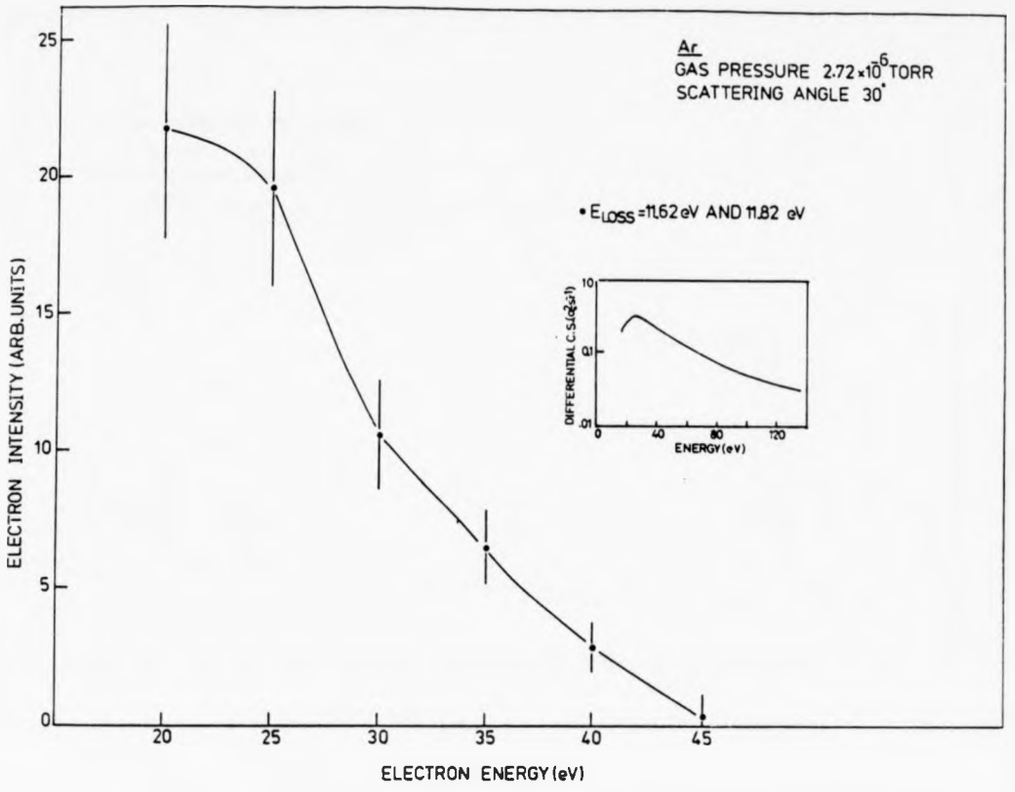

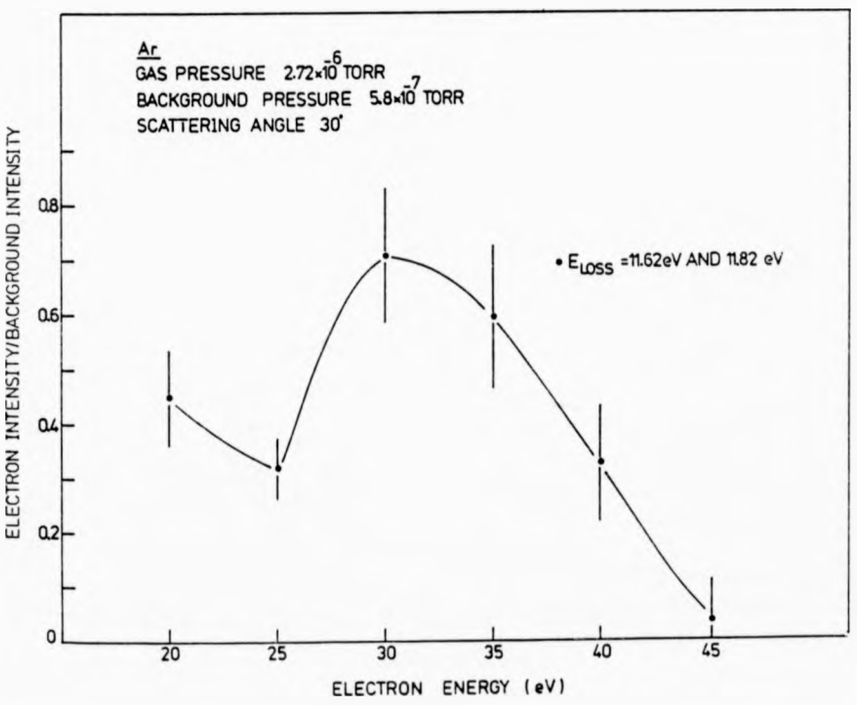

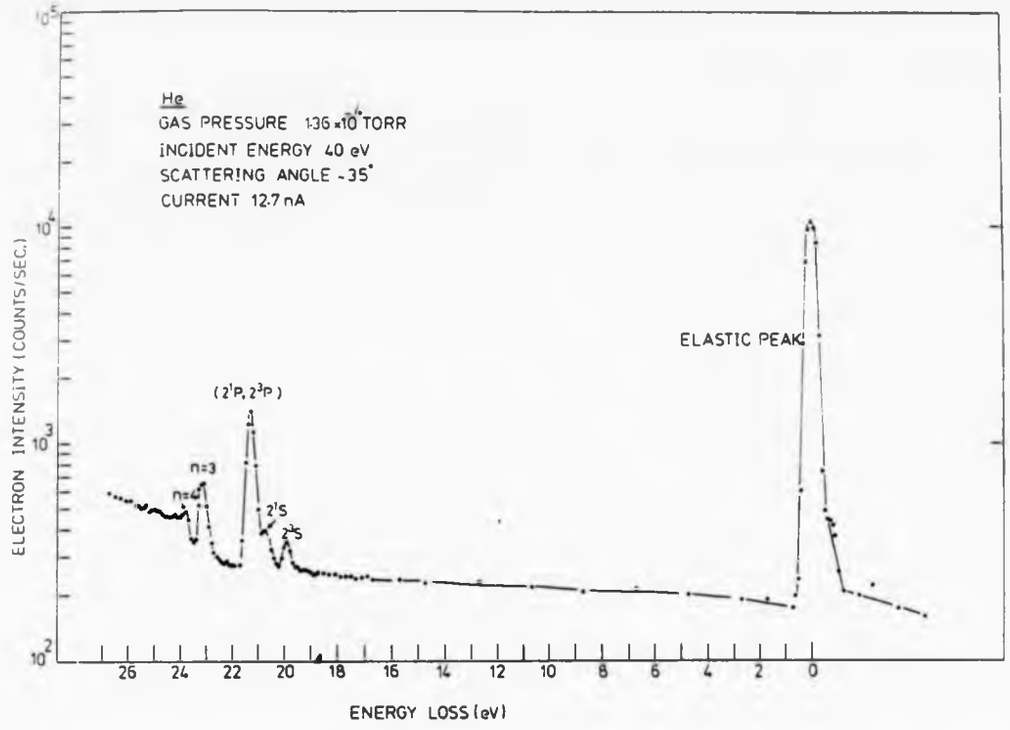

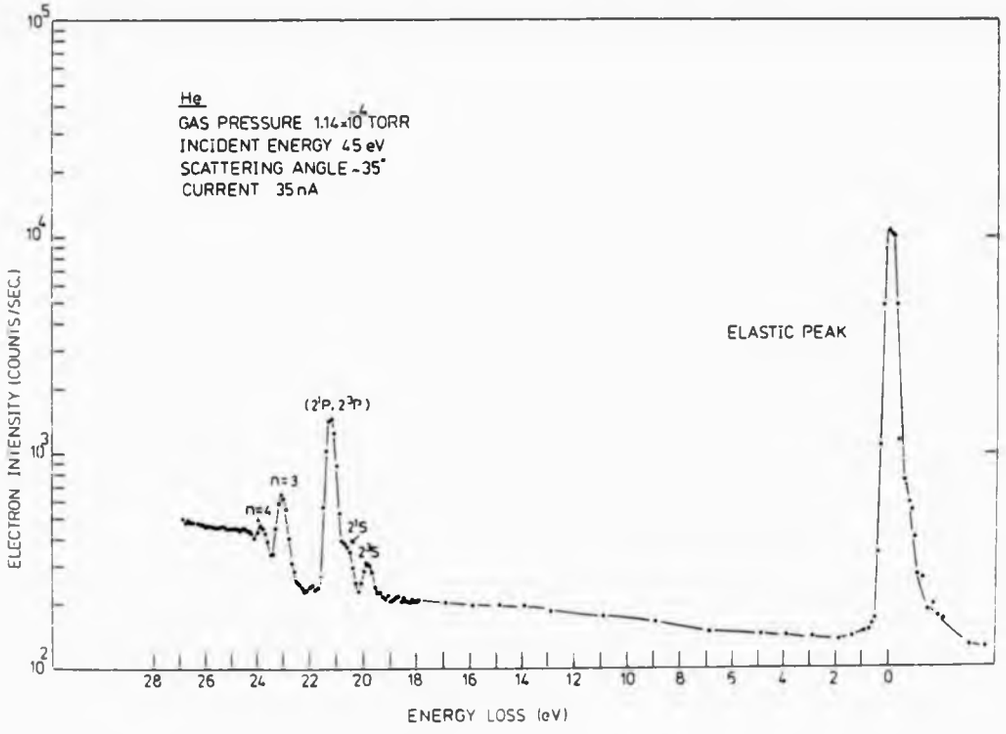

Fig. (5.23): Typical energy loss spectra of He

esolved and is indicated as a slight shoulder of the 2^1P state. The electronic configurations are obtained from the atomic levels of Moore (1949) and are shown on the above Figure.

CHAPTER 6

ELECTRON-PHOTON ANGULAR CORRELATIONS IN THE ELECTRON IMPACT EXCITATION OF Kr

6.1 Introduction

The coincidence technique has been used in experimental physics for more than one decade. It was first developed in nuclear physics by Bell (1966) and then extended into the fields of atomic and molecular physics. There are four kinds of delayed coincidence techniques.

1. Electron-photon coincidence:

This method was applied by Imhof and Read (1971 a) to measure the lifetimes of a number of atomic helium states. Its main advantage is that the problem of cascading from higher states can be completely eliminated. These authors also used this method, in which the inelastic scattered electron and subsequent decay photon pulses are used to start and stop the timing device to measure the lifetimes of different vibrational states of excited CO molecules (1971 b). In (1972) King et al used this method to measure threshold polarization of impact line radiation. In (1974) Eminyan et al reported the electron-photon angular correlations between electrons scattered inelastically from helium and photons decaying from the 2^1P state. They deduced from these measurements the ratio (λ) of differential cross section for exciting the degenerate magnetic sublevels and the relative phase (χ) of the corresponding excitation amplitudes. Further studies of these measurements on helium were carried out by Eminyan et al (1975), Standage and Kleinpoppen (1976), Tan et al (1977), Ugbabe et al (1977), and Sutcliffe et al (1978). The electron-photon angular correlations measurements have also been applied to Ar and Ne by Arriola et al (1975),

and by Malcolm and McConkey (1978) who reported the angular correlation between electrons scattered inelastically from the first excited states of Ar and photons decaying from these states to the ground state and by Ugbabe et al (1977) who reported results for Ne. Rubin et al (1969), Macek and Jaecks (1971), and Wykes (1972) reported a detailed theoretical treatment of collision processes in which the scattered particles and photons are detected in coincidence.

The present work presents the measurements of the electron-photon angular correlations in electron-krypton collisions by delayed coincidences between electrons scattered inelastically from Kr and photons emitted in the decay of the $^3P_1$ and $^1P_1$ states to the ground state. From these measurements λ and χ are deduced.

2. Photon-photon coincidence (cascade coincidence):

The principle of this method is that the target atom or molecule is excited by an electron beam. Photons of wavelengths λ_1 and λ_2 emitted from selected cascade states are used to start and stop the timing device. By observing delayed coincidences between the creation and subsequent decay of the intermediate states, a time spectrum is obtained from which the lifetime of the excited state can be obtained. Measurements of lifetimes of atoms, molecules and ions have been reviewed recently by Imhof and Read (1977).

3. Electron-electron coincidence (e, 2e):

This method can be expressed by the following reaction:

$$e(E_1) + A \rightarrow A^+ + e(E_2) + e(E_3)$$

The ejected electron $e(E_2)$ and scattered electron $e(E_3)$ are detected in coincidence. By using this technique, one can deduce the

collisional parameters (energy of impact electron, energy and angle of scattered electron, and energy and angle of ejected electron) for the ionization of atoms by electron impact. A number of groups have been involved in measuring the two outgoing electrons in coincidence, for example, Erhardt et al (1972), Weigold et al (1973), Backx et al (1975), Jung et al (1975), and Williams (1978).

4. Electron-ion-photon coincidence:

In this technique, the inelastic scattered electrons, ions and photons which result from the electron impact ionization are detected in coincidence. Backx et al (1973) used this method to measure the relative oscillator strength of the formation of the $B^2\Sigma$ state of CO^+.

6.2 Experimental

The block diagram of the electron-photon coincidence circuit is shown in Fig. (2.8). In this experiment, we selected one particular electron energy with the best signal to noise ratio (see section 5.2.1). The results indicate a maximum signal to noise ratio at approximately 35 eV, therefore this energy was chosen for the coincidence experiment. A relatively high electron beam current is needed to produce a high count rate of electrons and photons without increasing the gas pressure (see section 3.2.1). This current is obtained by passing electrons with energies up to 11.5 eV through the monochromator. The energy resolution of the analyzer is, however, still good enough to resolve $^3P_1$ and $^1P_1$ states. Typical currents monitored are 40 - 150 nA at 35 eV incident electron energy. This current is monitored continuously by a single Faraday cup (of 4mm diameter and 40mm length) located about 15mm beyond the interaction region. Care is taken to minimize any effects due to resonance trapping which would lead to a systematic error because the photons resonantly

absorbed and re-emitted by atoms in the atomic beam are no longer correlated in time with the scattered electrons and also the angular distribution of resonance radiation is not related to the electron impact excitation process. A study has been made of the photon intensity as a function of gas pressure at 35 eV incident electron energy as shown in Fig. (6.1). The results show that there is an increase in the photon intensity followed by gradual decrease and then a rise again. The decrease and increase in intensity are probably due to resonance trapping effects. The graph shows the electron intensity (with energy loss 10.03 eV) as a function of gas pressure. The results show a linear dependence of the electron signal on the gas pressure. Typical background pressures in the scattering chamber during measurements were about $4 * 10^{-7}$ Torr. The discriminator level for each of electron and photon channels are adjusted to a suitable level in order to discriminate against the noise without affecting the real signal.

In this experiment, the photon timing pulse from the constant fraction timing discriminator (CFTD) provided a start pulse for a time-to-amplitude converter (TAC), whilse the electron timing pulse provided a stop pulse. The amplitude of the TAC output signal is then proportional to the time difference between the start and stop pulses. A multichannel analyzer (MCA) is used to record the resulting pulse height spectrum from the TAC. This spectrum consists of true coincidences (where the electrons and photons originate from the excitation of an atom) and random coincidences (where the electrons and photons which have no common origin). The true coincidences form a peak on top of a background of coincidences.

Typical coincidence spectra of $^3P_1$ and $^1P_1$ states of Kr obtained from the MCA are shown in section (6.6). Normally, one channel represents 0.8 ns. The decay lifetimes of $^3P_1$ and $^1P_1$ states are 6.15 and 5.51 ns respectively (Dow and Knox (1966)). The counting rates of the electrons

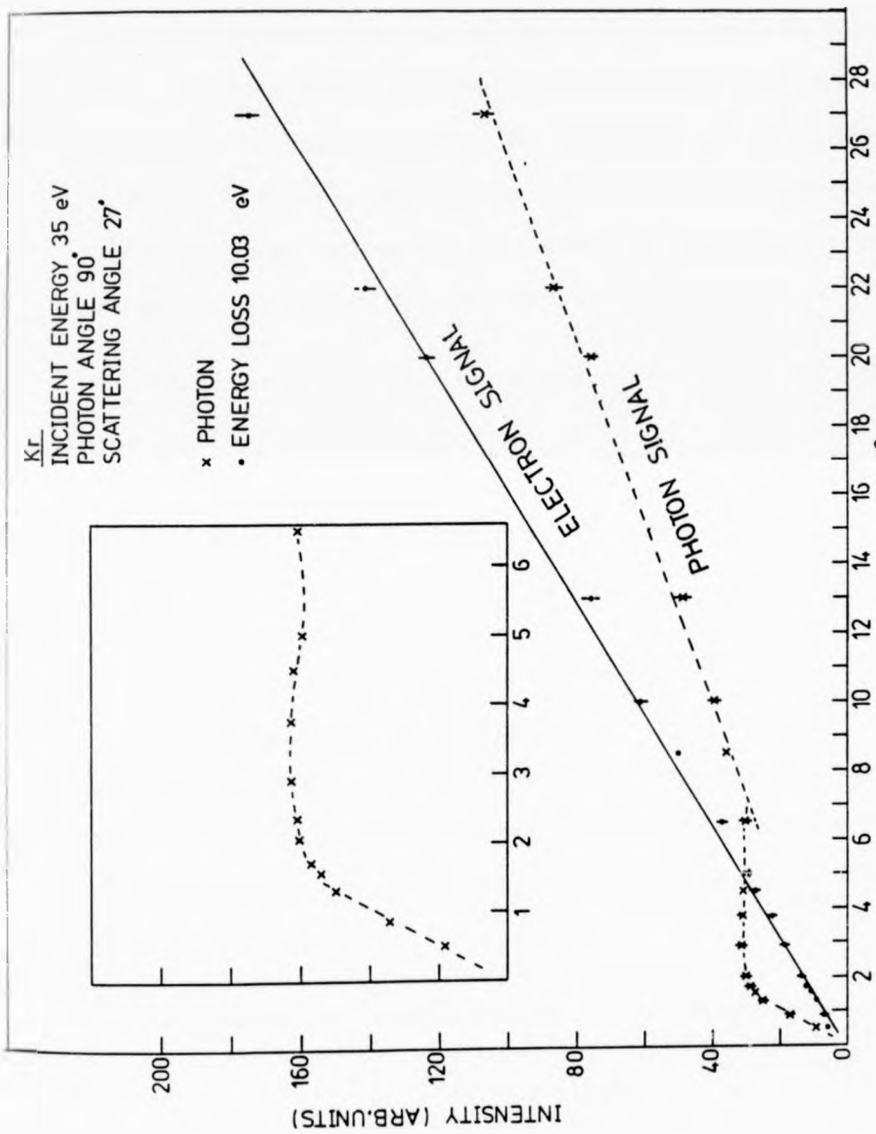

Fig. (6.1): Dependence of the photon and electron signals (10.03 eV energy loss) on the gas pressure. The inset shows the enlarged scale of the photon intensity from lower gas pressure up to 7.0 * 10^{-6} torr (1 rms error).

and the photons are checked before and after each run in order to make sure that no change took place during the run.

6.3 Coincidence analysis

In this experiment, the real coincidences fall into a group of about 26 channels of the MCA corresponding to a range of delays Δt which is determined by the resolution time of the apparatus and by the lifetime of the excited state. The number of real coincidences collected in time T is found by subtracting the base line counts measured in 167 channels outside Δt from the total number of coincidences, real and random, within the coincidence peak confined to Δt.

The procedure used was as follows. Referring to Fig. (6.2)

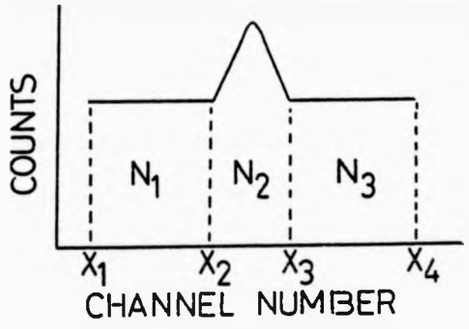

Fig. (6.2)

The area under the curve was divided into three regions called N_1, N_2, and N_3. The area of these regions are obtained by integration within the regions bound by (X_2-X_1), (X_3-X_2), and (X_4-X_3) using the multichannel analyzer.

The random coincidences B under the coincidence peak are given by

$$B = \frac{(N_1+N_3)\ (X_3-X_2)}{(X_2-X_1) + (X_4-X_3)} \qquad (6.1)$$

The number of true coincidences N_c is

$$N_c = N_2 - B \qquad (6.2)$$

The error δN_c in the number of true coincidences is given by

$$\delta N_c^2 = \left(\frac{\delta N_c}{\delta N_2}\right)^2 \Delta N_2^2 + \left(\frac{\delta N_c}{\delta B}\right)^2 \Delta B^2 \qquad (6.3)$$

Therefore,

$$\delta N_c = \sqrt{N_2 + \left\{ \frac{X_3 - X_2}{(X_2 - X_1) + (X_4 - X_3)} \right\}^2 \{N_1 + N_3\}} \qquad (6.4)$$

The number of the coincidences N_c is normalized with respect to the number of inelastic electrons (N_e) collected for each run (to make the measurements independent of intensities).

The parameters $\left(\frac{N_c}{N_e}\right)$ and $\left(\frac{\delta N_c}{N_e}\right)$ have been used to compare the coincidence result for different experimental conditions.

6.4 Test for systematic errors

Typical coincidence spectra are shown in section (6.6). These spectra are obtained as the analyzer is tuned to the $^3P_1$ and $^1P_1$ states (10.03 eV and 10.64 eV energy loss). A number of tests have been performed to check the results:

1. When the electron analyzer is tuned on the wing of the elastic peak (not on the top of the peak, because of high electron counts resulting in the saturation of the electron channeltron), no coincidences are observed.

2. When the atomic beam pressure is high enough to cause radiation trapping, no coincidences are observed.

6.5 Theory of electron-photon angular correlations

The excited J=1 states (Macek and Jaecks (1971)) can be described

by

$$|\psi> = a_1|11> + a_o|10> + a_{-1}|1\text{-}1> \tag{6.5}$$

The amplitudes $a_M(\Theta_e, \phi_e, E)$ describe the excitation to particular sublevels $|J, M_j>$ by electrons of incident energy E scattered through an angle Θ_e and ϕ_e. The dependence on ϕ_e can be factored out. Then the amplitudes depend only on E and Θ_e

$$a(M, E, \Theta_e, \phi_e) = a_M(E, \Theta_e)\ e^{-iM\phi_e} \tag{6.6}$$

Since the scattering process is symmetric about the scattering plane, one can show $a_1 = -a_{-1}$.

The amplitudes are related to the differential cross sections as follows

$$|a_1|^2 = \sigma_1 \tag{6.7}$$

$$|a_o|^2 = \sigma_o \tag{6.8}$$

$$2|a_1|^2 + |a_o|^2 = \sigma \tag{6.9}$$

where σ is the differential cross section for exciting the P_1 state and σ_M is the differential cross section for exciting the magnetic sublevels. The amplitudes σ_M are in general complex number. However, since $|\psi>$ is defined only up to an over all phase factor, a_o may be assumed real and positive.

The relative phase χ between a_1 and a_o is defined by

$$a_1 = |a_1|e^{i\chi} \quad (-\pi \leq \chi \leq \pi) \tag{6.10}$$

The parameter λ is defined by

$$\lambda = \frac{\sigma_o}{\sigma} = \frac{|a_o|^2}{2|a_1|^2 + |a_o|^2} \quad o \leq \lambda \leq 1 \quad . \tag{6.11}$$

The wave function $|\psi>$ is described completely (for a given E, θ_e, ϕ_e) by the parameters σ, λ and χ .

Macek and Jaecks (1971) formulated the theory of angular correlations between photons and scattered electrons. They showed that

$$\frac{d^2P_c}{d\Omega e\, d\Omega_\gamma} = \frac{\sigma}{\Sigma}\frac{dP_c}{d\Omega_\gamma} \tag{6.12}$$

where $$\frac{dP_c}{d\Omega_\gamma} = \left(\frac{3}{8\pi}\right)\{\lambda\sin^2\theta_\gamma + \left(\frac{1-\lambda}{2}\right)(\cos^2\theta_\gamma + 1) - \left(\frac{1-\lambda}{2}\right)\sin^2\theta_\gamma \cos 2(\phi_\gamma-\phi_e) + \{\lambda(1-\lambda)\}^{\frac{1}{2}}\cos\chi \sin 2\theta_\gamma \cos(\phi_\gamma-\phi_e)\} \tag{6.13}$$

and $\frac{d^2P_c}{d\Omega e\, d\Omega_\gamma}$ is the joint probability density for scattering of the electrons in direction (θ_e, ϕ_e) in any P_1 excitation with subsequent emission of the photon in direction $(\theta_\gamma, \phi_\gamma)$. Σ is the total cross section for excitation of the P_1 state,

$\frac{dP_c}{d\Omega_\gamma}$ is the probability density for photon emission after electron scattering in a particular direction.

In our case, the electron beam is incident along the z-direction on the target located at the origin. Scattered electrons are collected by the electron analyzer whose position defines the scattering plane. Therefore, $\phi_e = 0$ for all detected scattered electrons. Photons are counted without regard to polarization by a detector placed in the scattering plane on the opposite side from the electron analyzer, i.e. $\phi_\gamma = \pi$.

In this case eq. (6.13) becomes

$$\frac{dP_c}{d\Omega_\gamma} = \frac{3}{8\pi}N \tag{6.14}$$

where N is the angular correlation function and is defined by

$$N = \lambda \sin^2\theta_\gamma + (1-\lambda)\cos^2\theta_\gamma - 2\{\lambda(1-\lambda)\}^{\frac{1}{2}} \cos\chi \sin\theta_\gamma \cos\theta_\gamma \quad . \qquad (6.15)$$

6.6 Results

Fig. (6.3) shows a typical random (background) coincidence spectrum. This spectrum is taken when the analyzer is tuned to the wing of the elastic peak.

Figs. (6.4) and (6.5) show typical delayed coincidence spectra for the $^3P_1$ state (10.03 eV energy loss) at two different photon angles (120^o and 75^o).

Fig. (6.6) shows a coincidence spectrum for the $^1P_1$ state (10.64 eV energy loss).

The upper part of Fig. (6.7) shows the electron-photon angular correlation for the excitation of the $^3P_1$ state while the lower part shows the results for the excitation of the $^1P_1$ state. The data shown in Fig. (6.7) are the average values extracted from the two electron-photon angular correlation spectra obtained under the same experimental conditions. These data are summarized in Tables (6.1) and (6.2). These data are fitted to the angular correlation function (relation 6.15) and the values of λ and χ (which are summarized in Table (6.3)), are then deduced. In fact, the angular correlation function (relation (6.15)) is formulated for the excitation of the J=1 states but each of the excited $^3P_1$ and $^1P_1$ states is a mixture of a triplet and singlet state (Hippler and Schartner (1974)). These authors treated the wave functions for the two levels $^3P_1$ and $^1P_1$ states in a semi-empirical way using LS wave function.

In the previous electron-photon angular correlations in the electron impact excitation of Ar and Ne by Arriola et al (1975) and Ugbabe et al (1977), the energy resolution of the scattered electron beam was insufficient to

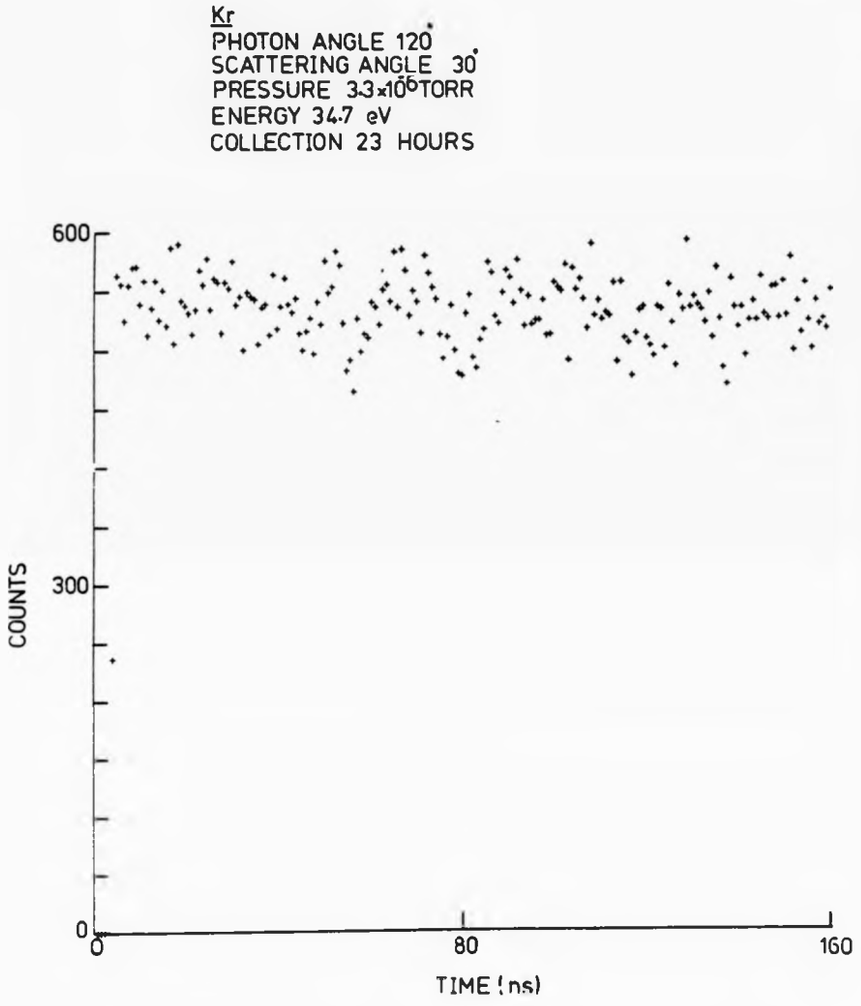

Fig. (6.3): A typical random coincidence spectrum. The photon count rate is ∿3400 Hz, the electron count rate is ∿2300 Hz.

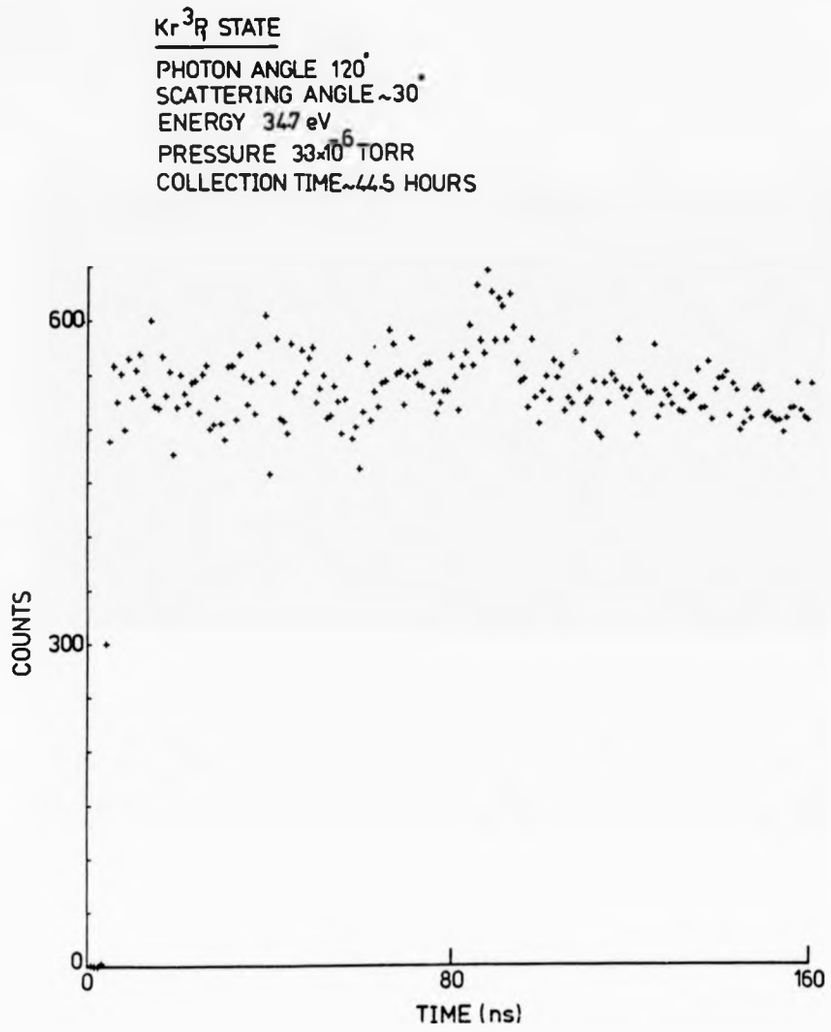

Fig. (6.4): A typical delayed coincidence spectrum for the $^3P_1$ state. The photon count rate is ∿3560 Hz, the inelastic count rate is ∿1200 Hz.

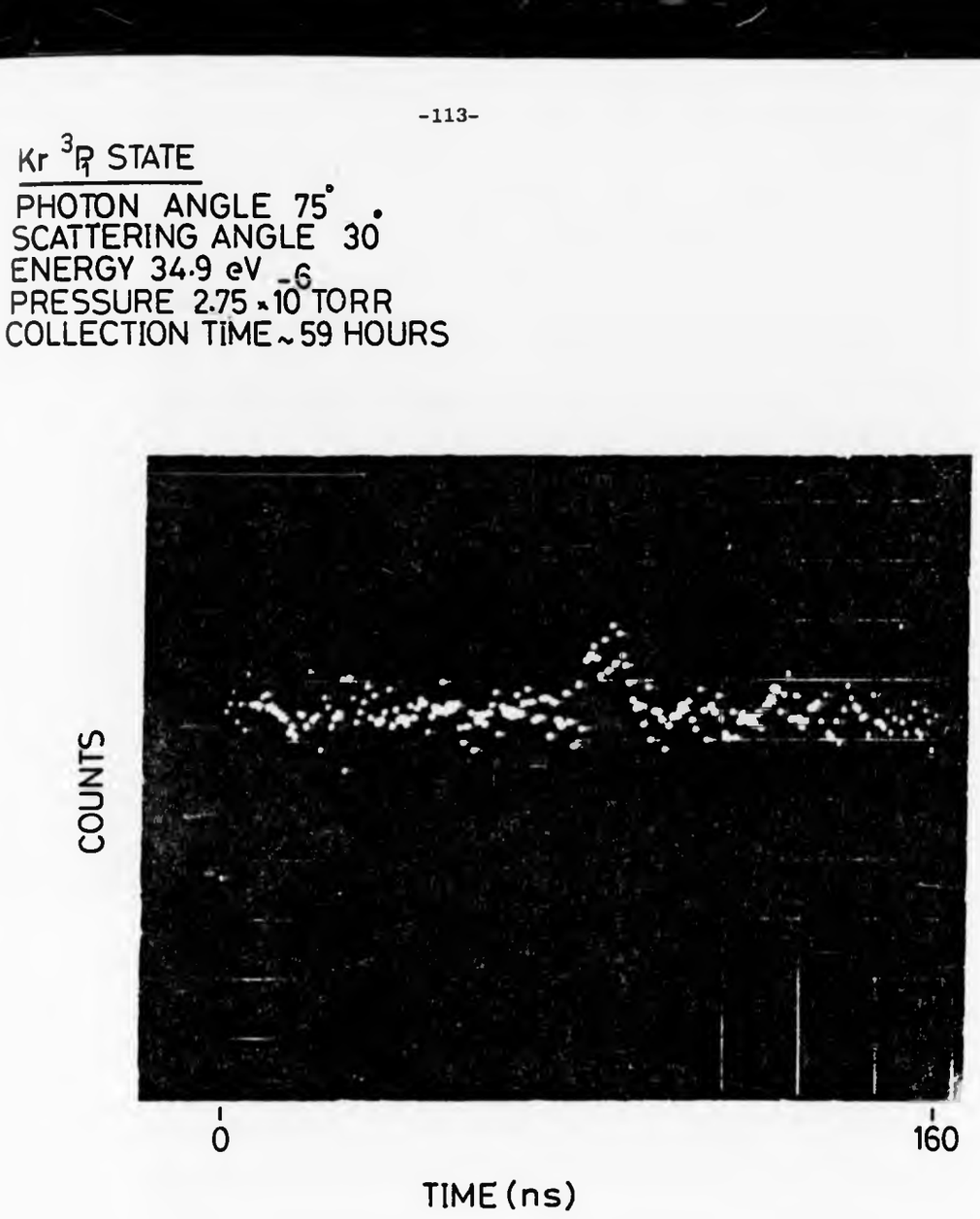

Fig. (6.5): A typical delayed coincidence spectrum for the $^3P_1$ state. The photon count rate is ∿3566 Hz, the inelastic electron count rate is ∿1253 Hz.

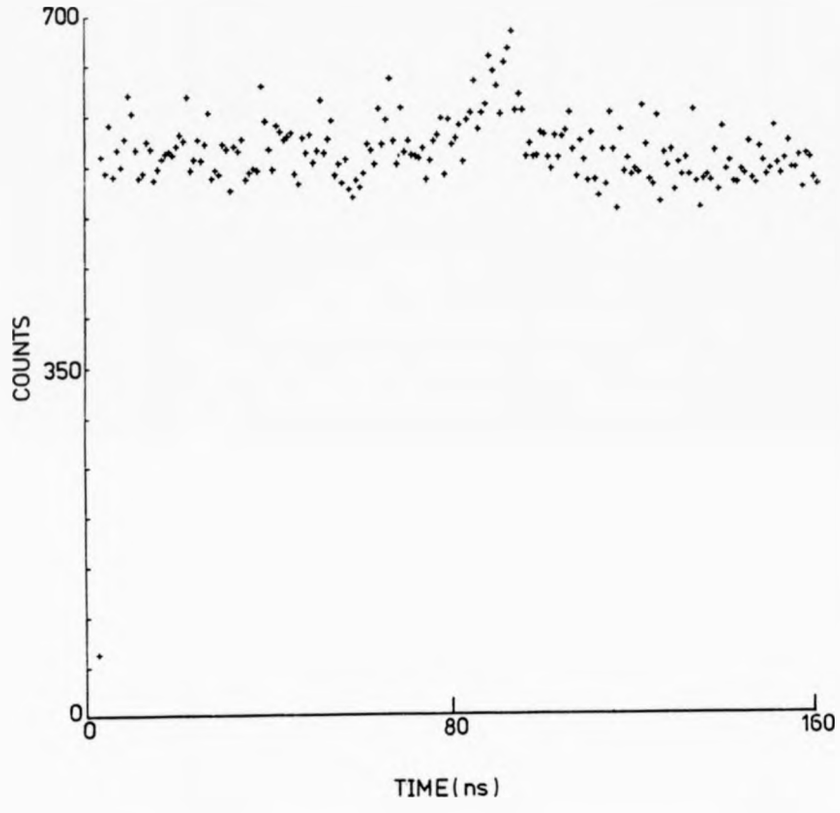

Fig. (6.6): A typical delayed coincidence spectrum for the $^1P_1$ state. The photon count rate is ∿3839 Hz, the inelastic electron count rate is ∿2169 Hz.

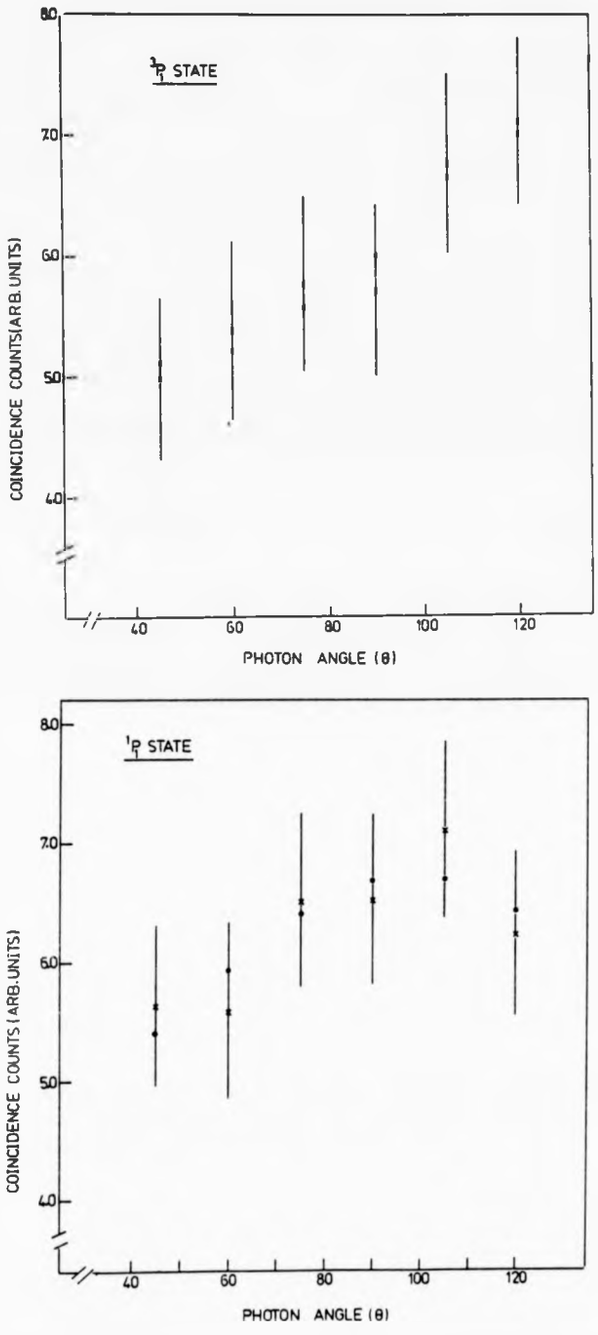

Fig. (6.7): The upper part shows the electron-photon angular correlation for the excitation of the $^3P_1$ state, while the lower part shows the results for the excitation of the $^1P_1$ state (1 rms error).

allow separation between $^3P_1$ and $^1P_1$ states. Since the relative cross sections for the excitation of the triplet and singlet states (σ_3/σ_1) (for the scattering angles and incident energies under study) are small, these authors treated the angular correlation measurements for the excitation $^3P_1$ and $^1P_1$ states in the same way as helium (relation (6.15)) by ignoring the presence of the triplet excitation. Recently, Malcolm and McConkey (1978) reported the electron-photon angular correlations for (resolved $^3P_1$ and $^1P_1$ states) Ar. They treated the angular correlation measurements for the excitation $^3P_1$ and $^1P_1$ states independently.

Angle	Experimental data (N_c/N_e)	Fitted data
45°	4.983 ± 0.682	5.118
60°	5.381 ± 0.756	5.213
75°	5.775 ± 0.733	5.573
90°	5.725 ± 0.727	6.099
105°	6.770 ± 0.749	6.652
120°	7.126 ± 0.704	7.083

Table (6.1): Experimental data for the angular correlation of the excitation of $^3P_1$ state at 34.9 eV incident energy (Fig. (6.7)).

Angle	Experimental data (N_c/N_e)	Fitted data
45^o	5.634 ± 0.745	5.394
60^o	5.587 ± 0.714	5.932
75^o	6.515 ± 0.691	6.404
90^o	6.525 ± 0.695	6.683
105^o	7.111 ± 0.706	6.695
120^o	6.236 ± 0.557	6.436

Table (6.2): Experimental data for the angular correlation of the excitation of $^1P_1$ state at 34.9 eV incident energy (Fig. (6.7)).

Incident energy (eV)	State	λ	χ(rad)
34.9	$^3P_1$	0.4921 ± 0.0304	-1.3955 ± 0.0278
34.9	$^1P_1$	0.5877 ± 0.0497	-1.5186 ± 0.0407

Table (6.3): The values of λ and χ for the excitation of $^3P_1$ and $^1P_1$ states.

CHAPTER 7

CONCLUSIONS

An electron impact spectrometer described in this thesis has been used for a wide range of investigations. The major results obtained from our study are as follows:

1. A survey of UV excitation functions of rare gas atoms (He, Ne, Ar, Kr, and Xe) near the threshold of excitation is produced by electron bombardment. The features which are observed in the excitation functions are compared with previous experiments (total cross section for metastable excitation by Pichanic and Simpson (1968), with the transmission experiment by Sanche and Schulz (1972), and with the UV photon excitation functions by Brunt et al (1977 a,b)). The present results show good agreement with the above experiments except for helium which does not match the one observed by Brunt et al. Probably the present excitation function of helium is dominated by metastable atoms. A further study has been made in the photon channel to measure the angular intensity distribution of photons emitted from the first excited states of Kr and Xe and the polarization was deduced. The results show negative polarization over the electron energy studied. No theoretical prediction of the polarization of the above lines exist.

2. In the electron channel, the energy loss spectra of He, Ar, Kr, and Xe have been measured over the incident energy range from 25 eV to 45 eV and at scattering angles of 27^{o} and 40^{o}. From these measurements, the inelastic cross sections for the prominent peaks of Ar, Kr and Xe are deduced. In addition, the dependence of the differential excitation functions of Ar, Kr, and Xe are obtained.

Results of inelastic cross sections of 3p - 4s, s' states for Ar at incident energies (30 - 40 eV) and at scattering angles of 30^{o} show good agreement with the theoretical values of Sawada et al (1971). No theoretical prediction of the inelastic cross sections for other gases exist.

3. A delayed coincidence technique was applied to the investigations of the angular correlations between electrons scattered inelastically and the subsequent photons emitted in the decay of $^{3}P_{1}$ and $^{1}P_{1}$ states of Kr. The data obtained from these measurements are fitted to the relation (6.15) (which is formulated to J=1 states) and λ and χ are then deduced. In spite of the poor signal to noise ratio in the electron channel, the error in coincidence rate at each photon angle was found to be about 10%.

References

Arriola H., Teubner P.J.O., Ugbabe A., and Weigold E. 1975, J. Phys. B. (Atom. Molec. Phys.) 8, 1275.

Al-Shamma S.H., and Kleinpoppen H. 1977, Abstracts of Papers of Xth International Conference on the Physics of Electronic and Atomic Collisions, Paris, Vol. 1, p.518.

1978, J. Phys. B. (Atom. Molec. Phys.) 11, L367.

Brunt J.N.H., King G.C., and Read F.H. 1977a, J. Phys. B. (Atom. Molec. Phys.) 10, 3781.

1977b, Abstracts of Papers of Xth International Conference on the Physics of Electronic and Atomic Collisions, Paris, Vol. 2, p.942.

Brunt J.N.H., Read F.H., and King G.C. 1977c, J. Phys. E. (Sci. Instr.) 10, 134.

Baranger E., and Gerjuoy E. 1957, Phys. Rev. 106, 1182.

1958, Proc. Phys. Soc., A72, 326.

Burke P.G., and Schey H.M. 1962, Phys. Rev. 126, 147.

Bell R.E. 1966, in "Alpha- Beta- Gamma-Ray Spectroscopy", ed. K. Siegbahn (North Holland, Amsterdam) 2, 911.

Backx C., Klewer M., and Van der Wiel M.J. 1973, Chem. Phys. Lett., 20, 100.

Backx C., Wight G.R., Tol R.R., and Van der Wiel M.J. 1975, J. Phys. B. (Atom. Molec. Phys.) 8, 3007.

Candler C. 1964, in "Atomic Spectra" (Hilger and Watts Ltd., London).

Dow J.D., and Knox R.S. 1966, Phys. Rev. 152, 50.

Delage A., Roy D., and Carett J-D. 1975, Abstracts of Papers of IXth International Conference on the Physics of Electronic and Atomic Collisions, Seattle, Vol. 2, p.1099.

Dassan H., Malcolm I.C., and McConkey J.W. 1977, J. Phys. B. (Atom. Molec. Phys.) 10, L493.

Elett A., Foot P.D., and Mohler F.L. 1926, Phys. Rev. 27, 31.

Eldridge J.A., and Olsen H.F. 1926, Phys. Rev. 28. 1151.

Elston S.B., Lawton S.A., and Pichanic F.M.J. 1973, Abstracts of Papers of VIII International Conference on the Physics of Electronic and Atomic Collisions, Beograd, Vol. 1, p.480.

Enemark E.A., and Gallaghar I. 1972, Phys. Rev. A6, 192.

Ehlers V.J., and Gallagher A.C. 1973, Phys. Rev. A7, 1573.

Ehrhardt H., Hesselbacher K.H., Jung K., Schulz M., and Willmann K. 1972, J. Phys. B. (Atom. Molec. Phys.) 5, 2107.

Eminyan M., MacAdam K.B., Slevin J., and Kleinpoppen H. 1974, J. Phys. B. (Atom. Molec. Phys.) 7, 1519.

Eminyan M., MacAdam K.B., Slevin J., Standage M.C., and Kleinpoppen H. 1975, J. Phys. B. (Atom. Molec. Phys.) 8, 2058.

Federov V.L., Mezentsev A.P. 1965, Opt. Spectroscopy, 19, 5.

Fano U., and Macek J.H. 1973, Rev. Mod. Phys., 45, 553.

Heddle D.W.O., and Keesing R.G.W. 1967, Proc. Roy. Soc., A299, 212.

Heddle D.W.O., Keesing R.G.W., and Watkins, R.D. 1974, Proc. Roy. Soc., A337, 443.

Heddle D.W.O. 1976, Contemp. Phys., Vol. 17, 443.

Hughes A.L., and Rojansky V. 1929, Phys. Rev. 34, 284.

Heideman M.G.M., Smith C., and Smith, J.A. 1969, Physica, 45, 305.

Hafner H., Kleinpoppen H., and Kruger H. 1965, Phys. Letts., 18, 270.

Hippler R., and Schartner K.H. 1974, Z. Phys., 270, 225.

Imhof R.E., and Read F.H. 1971a, J. Phys. B. (Atom. Molec. Phys.) 4, 450.

1971b, Chem. Phys. Lett., 11, 326.

1977, Reports on Progress in Physics, 40.

Jung K., Schubert E., Paul D.A.L., and Ehrhardt H. 1975, J. Phys. B. (Atom. Molec. Phys.) 8, 1330.

Koschmieder H. 1974, Thesis, Physics Department, University of Stirling.

King G.C.E., Adam A., and Read F.H. 1972, J. Phys. B. (Atom. Molec. Phys.) 5, L254.

Kuppermann A., Rice J.K., and Trajmar S. 1968, J. Phys. Chem., 72, 3894.

Kleinpoppen H. 1969, in "Physics of One and Two Electron Atoms", ed. F. Bopp and H. Kleinpoppen, p.612.

1975, Atomic Physics, ed. G. Zu Putlitz, E.W. Weber and A. Winnacker, Vol. 4, p.449.

1977 Advances in Quantum Chemistry, Vol. 10, p.77.

Kuyatt C.E., and Simpson J.A. 1967, Rev. Sci. Instr., 38, 103.

Kuyatt C.E. 1968, Methods of Experimental Physics, ed. L. Marton, Vol. 7a, 11.

Kuyatt C.E., Simpson J.A., and Mielczarek S.R. 1965, Phys. Rev. 138, A385.

Lawrence G.M. 1970, Phys. Rev. 2, 397.

Lewis B.R., Furness J.B., Teubner P.J.O., and Weigold E. 1974, J. Phys. B. (Atom. Molec. Phys.) 7, 1083.

Lewis B.R., Weigold E., and Teubner P.J.O. 1975, J. Phys. B. (Atom. Molec. Phys.) 8, 212.

Lassettre E.N., Skerbele A., Dillon M.M., and Ross K.J. 1968, J. Chem. Phys., 48, 5066.

Lassettre E.N. 1969, Can. J. Chem., 47, 1733.

Moiseiwitsch B.L., and Smith S.J. 1968, Rev. Mod. Phys. 40, 238.

Macek J. and Jaecks D.H. 1971, Phys. Rev. A4, 2288.

Mumma M.J., and Zipf E.C. 1971, J. Chem. Phys., 55, 1661.

Mumma M.J., Misakian M., Jackson W.M., and Faris J.L. 1974, Phys. Rev. A9, 203.

Malcolm I.C., and McConkey J.W., to be published in J. Phys. B. (Atom. Molec. Phys.) 1978.

McFarland R.H. and Soltysik E.A. 1963, Phys. Rev., 129, 2581.

McFarland R.H. 1964, Phys. Rev. 133A, 986.

1967, Phys. Rev., 156, 55.

Moore C.E. 1949, Atomic energy levels as derived from the analysis of optical spectra circular 467, Vol. 1.

1952, Vol. 2.

1958, Vol. 3.

Marmet P., and Kerwin L. 1960, Can. J. Phys., 38, 787.

Oppenheimer J.R. 1927a, Z. Phys., 43, 27.

1927b, Proc. Nat. Acad. Sci., 13, 900.

1928, Phys. Rev., 32, 361.

Ott W.R., Kauppila W.E., and Fite W.L. 1970, Phys. Rev. A1, 1089.

Ottley T.W., and Kleinpoppen H. 1975, J. Phys. B. (Atom. Molec. Phys.) 8, 621.

Purcell E.M. 1938, Phys. Rev. 54, 818.

Penney W.C. 1932, Proc. Nat. Acad. Sci., 18, 231.

Percival I.C., and Seaton M.J. 1958, Phil. Trans. Roy. Soc. London, A251, 113.

Pichanic F.M.J., and Simpson J.A. 1968, Phys. Rev., 168, 64.

Quarder Von B. 1927, Z. Phys., 41, 674.

Rubin K., Bederson B., Goldstein M., and Collins, R.E. 1969, Phys. Rev., 182, 201

Raible V. 1974, Thesis, Physics Department, University of Stirling.

Read F.H. 1970, J. Phys. E. (Sci. Instr.) 3, 127.

Read F.H., Brunt J.N.H., and King G.C. 1976, J. Phys. B. (Atom. Molec. Phys.) 9, 2209.

Smit J.A. 1935, Physica 2, 104.

Swanson N., Cooper J.W., and Kuyatt C.E. 1973a, Phys. Rev. A8, 1825.

Swanson N., Celotta R.J., Kuyatt C.E. 1973b, Abstracts of Papers of VIII International Conference on the Physics of Electronic and Atomic Collisions, Beograd, p.478.

1976, in "Electron Photon Interactions with Atoms", ed. H. Kleinpoppen and M.R.C. McDowell, p.661.

Skinner H.W.B. 1926, Proc. Roy. Soc. A112, 642.

Skinner H.W.B., and Appleyard E.T.S. 1927, Proc. Roy. Soc., A117, 224.

Simpson J.A., and Kuyatt C.E. 1966, J. App. Phys., 37, 3805.

Sawada T., Purcell J.E., and Green A.E.S. 1971, Phys. Rev., A4, 193.

Schulz G.J. 1963, Phys. Rev. Lett., 10, 104.

Schulz G.J. 1973, Rev. Mod. Phys., 45, 378.

Sanche L., and Schulz G.J. 1972, Phys. Rev. A5, 1672.

Spence D. 1977, Phys. Rev., A15, 883.

Standage M.C., Kleinpoppen H. 1976, Phys. Rev. Lett., 36, 577.

Sutcliffe V.C., Haddad G.M., Steph N.C., and Golden D.E. 1978, Phys. Rev., A17, 100.

Tan K.H., Fryar J., Farago P.S., and McConkey J.W. 1977, J. Phys. B. (Atom. Molec. Phys.) 10, 1073.

Ugbabe U., Teubner P.J.O., Weigold E., and Arriola H. 1977, J. Phys. B. (Atom. Molec. Phys.) 10, 71.

Whitteker J.H., and Dalby F.W. 1968, Can. J. Phys., 46, 193.

Williams J.F. and Crowe A. 1975, J. Phys. B. (Atom. Molec. Phys.) 8, 2233.

Williams J.F. and Willis B.A. 1975, J. Phys. B. (Atom. Molec. Phys.) 8, 1670.

Williams J.F. 1976 in "Electron Photon Interactions with Atoms", ed. H. Kleinpoppen and M.R.C. McDowell, p.309.

1978, J. Phys. B. (Atom. Molec. Phys.) 11, 2015.

Weigold E., Hood S.T., and Teubner P.J.O. 1973, Phys. Rev. Lett., 30, 475.

Williams W., Trajmar S., and Kupermann A. 1973, Abstracts of Papers of VIIIth International Conference on the Physics of Electronic and Atomic Collisions, Beograd, Vol. 1, p.328.

Wykes J. 1972, J. Phys. B. (Atom. Molec. Phys.) 5, 1126.

Zaidi A.A., McGregor I., and Kleinpoppen H. 1978, J. Phys. B. (Atom. Molec. Phys.) 11, L151.

4